

Technische Universität München  
TUM School of Engineering and Design

# **Theoretical and Experimental Investigation of High Frequency Thermoacoustic Instabilities in Premixed Multi-Jet Combustors**

**Jan-Andre Rosenkranz**

Vollständiger Abdruck der von der TUM School of Engineering and Design  
der Technischen Universität München zur Erlangung eines

DOKTORS DER INGENIEURWISSENSCHAFTEN (DR.-ING.)

genehmigten Dissertation.

Vorsitz:

Prof. Dr. ir. Daniel Rixen

Prüfende der Dissertation:

Prof. Dr.-Ing. Thomas Sattelmayer

Prof. Dr. Thierry Schuller

Die Dissertation wurde am 20.03.2024 bei der Technischen Universität München eingereicht  
und durch die Fakultät für Maschinenwesen am 20.09.2024 angenommen.



---

## Abstract

The fundamental understanding of high frequency instabilities and the underlying thermoacoustic flame response mechanisms are crucial to predict and mitigate this highly destructive type of instability in Multi-Jet Combustors in rocket and gas turbine engines. The thesis provides experimental insights into hydrogen and natural gas's perfectly premixed flame response by phase-locked  $\text{OH}^*$  chemiluminescence images. The dominant flame response mechanisms are extracted from the experimental results. Alongside the established flame compression and displacement mechanism, coherent vortex shedding is demonstrated as a dominating convective flame response mechanism for high frequency instabilities due to a strong injector coupling of the first transverse mode with the injector tubes. Combustor stability analysis in the low frequency limit, including injector coupling, is well predictable by two-port network models and basic acoustic theory. In the high frequency case numerical methods are the state-of-the-art. However, theory and low order models become increasingly important for the interpretation of experiments and high-fidelity LES simulations. In this context, a novel two-port network modelling approach and a consistent theory for high frequency instabilities in can combustors is deduced, including a convective flame response model. Validation is carried out for the acoustic transfer matrices using a generic test setup. The local flame transfer function is validated with the phase-averaged  $\text{OH}^*$  chemiluminescence images of the multi-jet combustor.

## Kurzfassung

Das grundlegende Verständnis hochfrequenter Instabilitäten und der zugrundeliegenden thermoakustischen Flammenantwortmechanismen ist von entscheidender Bedeutung für die Vorhersage und Dämpfung dieser stark destruktiven Instabilitäten in Strahlflammen von Raketen- und Gasturbinentriebwerken. Die vorliegende Arbeit liefert experimentelle Erkenntnisse über das Verhalten von Wasserstoff und Erdgas in perfekt vorgemischten Flammen durch phasengemittelten  $\text{OH}^*$ -Chemilumineszenzbilder. Die dominanten Mechanismen des Flammenverhaltens werden aus den experimentellen Ergebnissen extrahiert. Neben dem etablierten Mechanismus der Flammenkompression und -verschiebung wird die kohärente Wirbelablösung als dominierender konvektiver Flammenantwortmechanismus für hochfrequente Instabilitäten aufgrund einer starken Injektorkopplung der ersten Transversalmode mit den Injektorrohren nachgewiesen. Im niederfrequenten Bereich ist die Stabilitätsanalyse der Brennkammer, inklusive der Injektorkopplung, mit Hilfe von Zwei-Tor-Netzwerkmodellen und der grundlegenden akustischen Theorie gut vorhersagbar. Im Hochfrequenzbereich werden häufig numerische Methoden eingesetzt. Theorie und Modelle niedriger Ordnung werden jedoch immer wichtiger für die Interpretation von Experimenten und LES-Simulationen. Daher wird in dieser Arbeit die Modellierung der niederfrequenten Thermoakustik durch Zwei-Tor-Netzwerke auf den hochfrequenten Bereich verallgemeinert. Eine konsistente Theorie für hochfrequente Instabilitäten in zylindrischen Brennkammern, inklusive eines konvektiven Flammenantwortmodells, wird vorgeschlagen. Die Validierung der akustischen Transfermatrizen wird mit Hilfe eines generischen Versuchsaufbaus durchgeführt. Die lokale Flammenübertragungsfunktion wird mit den phasengemittelten  $\text{OH}^*$ -Chemilumineszenzbildern der Strahlflammen validiert.

# Contents

<b>1</b>	<b>Introduction</b>	<b>1</b>
1.1	Combustor Concept . . . . .	1
1.2	High Frequency Combustion Instabilities . . . . .	2
1.3	Convective Flame Response . . . . .	5
1.4	Combustor Stability Analysis . . . . .	9
1.5	Thesis Outline . . . . .	11
<b>2</b>	<b>Governing Equations</b>	<b>13</b>
2.1	Governing Conservation Equations . . . . .	13
2.2	Global Combustion Reaction . . . . .	15
2.3	Premixed Turbulent Flames . . . . .	17
<b>3</b>	<b>Linearised Disturbance Equations</b>	<b>21</b>
3.1	Linearised Conservation Equations . . . . .	21
3.2	Acoustic Disturbance Energy and Rayleigh Criterion . . . . .	23
3.3	Inhomogeneous Convective Wave Equation . . . . .	24
3.4	Acoustic Wave Propagation in Tubes . . . . .	26
<b>4</b>	<b>Experimental and Numerical Methods</b>	<b>28</b>
4.1	Phase-Locked OH* images . . . . .	28
4.2	Multi-Microphone-Method . . . . .	30
4.2.1	Azimuthal Acoustic Pressure Field . . . . .	30
4.2.2	Axial Acoustic Pressure Field . . . . .	31
4.2.3	Axial Transfer Matrix Reconstruction . . . . .	32
4.3	Hybrid CFD/CAA Method . . . . .	32
<b>5</b>	<b>Distributed Flame Response Model</b>	<b>35</b>

5.1	Linearised Heat Release Density . . . . .	35
5.2	Acoustic Flame Response . . . . .	36
5.3	Convective Flame Response . . . . .	38
5.3.1	Linear Hydrodynamic Stability Analysis . . . . .	41
5.3.2	Acoustics - Turbulence - Flame - Closure . . . . .	45
<b>6</b>	<b>Low Order Network Modelling Theory</b>	<b>47</b>
6.1	High Frequency Transfer Matrix Method . . . . .	47
6.2	Duct Transfer Matrix . . . . .	49
6.3	Integral HF Acoustic Jump Conditions . . . . .	50
6.4	Area Change Transfer Matrix . . . . .	55
6.5	Flame Transfer Matrix . . . . .	57
6.6	Axially Distributed Convective FTF in a MJC . . . . .	59
<b>7</b>	<b>Validation of the Transfer Matrices</b>	<b>65</b>
7.1	Generic Experimental Setup . . . . .	65
7.2	Global and Area Change Transfer Matrix . . . . .	66
<b>8</b>	<b>Investigation of the Premixed Flame Response</b>	<b>71</b>
8.1	Experimental Setup With Pilot Burner . . . . .	71
8.1.1	Acoustic Forced Response Study . . . . .	75
8.1.2	Numerical Helmholtz Model . . . . .	78
8.1.3	Flame Response - Pressure Anti-Node and Pressure-Node Coupling . . . . .	82
8.2	Experimental Setup Without Pilot Burner for Natural Gas and Hydrogen . . . . .	90
<b>9</b>	<b>Validation of the Flame Response Model</b>	<b>98</b>
9.1	Mean Heat Release and Flow Field . . . . .	98
9.2	Convective Flame Response with Pilot Burner . . . . .	101
9.3	Convective Flame Response without Pilot Burner . . . . .	105
9.4	Axially Distributed Convective FTF . . . . .	109
<b>10</b>	<b>Summary and Conclusion</b>	<b>112</b>
<b>A</b>	<b>Appendix</b>	<b>115</b>

A.1	Natural Gas Composition . . . . .	115
A.2	Pressure Loss and Massflow Split . . . . .	115
A.3	Heat Loss Estimation . . . . .	120

# List of Figures

1.1	Sketch of the investigated MJC of the present thesis with the plenum, eight injector tubes and a combustion chamber of the respective lengths $L_P, L_T, L_C$ and diameters $d_P, d_T, d_C$ and the individual injector tube position $r_T, \theta_T$ . . . . .	3
1.2	Apollo mission rocket combustor (left) and space shuttle injector face plate (right) after the occurrence of HF thermoacoustic instability during engine testing. . . . .	4
5.1	Sketch of an axial cut through a cylindrical MJC with combustion chamber diameter $d_C$ at the centre of a single injector tube with diameter $d_T$ and a jet flame represented by the reaction progress variable iso-contour $C_r = 0.5$ with deflagrative flame stabilisation at the kinematic balance of the turbulent flame speed $s_t$ and the flame normal velocity of unburned gas $u_n$ close to the core region of the turbulent jet. . . . .	39
6.1	Cross-sectional acoustic pressure mode shape of the T1 mode for the injector coupling at the dump plane of the MJC configuration in the present thesis and for a generic configuration of a single injector tube coupled to the R1 mode to illustrate the separation of the acoustic domain at the transverse nodal lines and the combustor wall to obtain the cross-sectional integration boundaries of Eqs. 6.13 and 6.14. . . . .	55

6.2	Sketch of the investigated MJC configuration and the acoustic pressure mode shape of the T1 mode and the expected convective flame response to illustrate the dependency of the locally resolved $\text{ftf}(x, r, \theta)$ to the axially resolved $\text{FTF}_x(x)$ and the global FTF. . . . .	61
7.1	Generic injector coupling experimental setup to validate the acoustic transfer matrices with a forced response of the T1 mode with upstream and downstream forcing and pressure sensors at positions $T_1 - T_3$ in the tube and $C_1 - C_5$ in the cylindrical chamber.	66
7.2	Validation of the analytical and numerical model of the transfer matrix $\text{TM}_{pu}$ (Eq. 7.1) of the generic experiment Fig. 7.1 for the forced T1 mode. . . . .	67
7.3	Validation of the analytical and numerical model of the scattering matrix $\text{SM}_{fg}$ obtained from Eq. 6.26 with Eq. 6.6 of the generic experiment Fig. 7.1 for the forced T1 mode. . . . .	67
7.4	Validation of the analytical and numerical model of the transfer matrix $\text{TM}_{pu,A}$ of the area change (Eq. 6.26) of the generic experiment Fig. 7.1 for the forced T1 mode. . . . .	69
7.5	Validation of the analytical and numerical model of the scattering matrix $\text{SM}_{fg,A}$ obtained from Eq. 6.26 with Eq. 6.6 of the area change of the generic experiment Fig. 7.1 for the forced T1 mode.	69
8.1	Experimental setup for the integrated $\text{OH}^*$ images and simultaneous pressure measurements at the positions $\text{FP}_1 - \text{FP}_4$ , $C_1 - C_2$ and $T_1 - T_2$ . . . . .	72
8.2	Line-of-sight integrated mean HRR density distribution (top-left) and the corresponding integral axial (bottom-left) and radial (top-right) distribution for the MJC without pilot burner for the conditions summarised in Tab. 8.2. . . . .	74
8.3	Experimental forced response of the MJC for pressure anti-node coupling. . . . .	76
8.4	Experimental forced response of the MJC for pressure node coupling. . . . .	76

8.5	Experimental results for the nodal line (left) and the spin ratio (right) for pressure anti-node coupling and pressure node coupling at $f = 3100$ Hz with zero angles at the triangular forcing inlet at the top. . . . .	78
8.6	Numerical setup for pressure anti-node coupling (top) and pressure node coupling (bottom) with the forced axial acoustic velocity at $x_{\text{force}} = 0.25 L_C$ and impedance boundary conditions according to Tab. 8.3. . . . .	78
8.7	Numerical results of the acoustic pressure mode shapes at the peak frequencies of the forced response simulation with pressure anti-node coupling ( $L_T = 3/4\lambda_{T1}$ ) at $f = 3110$ Hz (top) and with pressure node coupling ( $L_T = 1/2\lambda_{T1}$ ) at $f = 3020$ Hz (middle) and at $f = 3150$ Hz (bottom) with the boundary conditions according to Tab. 8.3. . . . .	80
8.8	Numerical results of the normalised axial acoustic velocity at the exit of the injector tube three times during the period $T = 1/f$ for the two cases with pressure anti-node coupling ( $L_T = 3/4\lambda_{T1}$ ) at $f = 3110$ Hz (left) and with pressure node coupling ( $L_T = 1/2\lambda_{T1}$ ) at $f = 3150$ Hz (right). . . . .	81
8.9	Phase-locked Heat Release Rate (HRR) $\dot{q}(\varphi)$ (top), fluctuations $\dot{q}'(\varphi)$ (middle) and normalised HRR fluctuations $\dot{q}'(\varphi)/\bar{\dot{q}}$ (bottom) with pressure anti-node coupling (left) and with pressure node coupling (right) for natural gas (Tab. 8.2) at 3100 Hz. . . . .	84
8.10	Axially resolved HRR fluctuations $\dot{Q}'_x$ (bottom, $\square$ ), normalised fluctuations $\dot{Q}'_x/\bar{\dot{Q}}_x$ (top, $\square$ ), their respective offset (—) and envelopes (--) for pressure anti-node coupling ( <b>a</b> ) and pressure node coupling ( <b>b</b> ) with maximum, zero and minimum acoustic pressure amplitude at $\varphi = 0, 1/2\pi, \pi$ , respectively. . . . .	86
8.11	Integrated HRR fluctuations (top) and Rayleigh integral (bottom) with pressure anti-node coupling (left) and with pressure node coupling (right) over the phase-averaged period of the oscillation. . . . .	88

8.12	Integrated HRR fluctuations (top) and Rayleigh integral (bottom) separated into convective and offset contribution with pressure anti-node coupling (left) and with pressure node coupling (right) over the phase-averaged period of the oscillation. . . . .	89
8.13	Experimental setup for the integrated OH* images and simultaneous pressure measurements at the positions C <sub>1</sub> – C <sub>2</sub> , P <sub>1</sub> – P <sub>3</sub> and T <sub>1</sub> – T <sub>2</sub> without pilot burner. . . . .	91
8.14	Line-of-sight integrated mean HRR density distribution (top-left) and the corresponding integral axial (bottom-left) and radial (top-right) distribution for the MJC without pilot burner for natural gas operation according to Tab. 8.5. . . . .	93
8.15	Line-of-sight integrated mean HRR density distribution (top-left) and the corresponding integral axial (bottom-left) and radial (top-right) distribution for the MJC without pilot burner for hydrogen gas operation according to Tab. 8.5. . . . .	93
8.16	Phase-locked HRR $\dot{q}(\varphi)$ (top), fluctuations $\dot{q}'(\varphi)$ (middle) and normalised fluctuations $\dot{q}'(\varphi)/\bar{\dot{q}}$ (bottom) for H <sub>2</sub> (left) at $f = 3175$ Hz and CH <sub>4</sub> (right) at $f = 3100$ (Tab. 8.5). . . . .	95
9.1	Axial mean HRR distribution $\bar{Q}_x$ (top) and the axial velocity profile $\bar{u}$ (bottom) fitted to the experimental results of natural gas with pilot burner (left) and without pilot burner (right) for $T_u = 673$ K, $\lambda_{\text{CH}_4} = 1.5$ and $\bar{u}_T = 115 \text{ ms}^{-1}$ . . . . .	100
9.2	Mean speed of sound [ $\text{ms}^{-1}$ ] (top-left), mean HRR density [ $\text{Wm}^{-3}$ ] (bottom-left) and the resulting acoustic pressure mode shape [Pa] (top-right) and the convective HRR density fluctuations [ $\text{Wm}^{-3}$ ] (bottom-right) of the numerical Helmholtz model at 3100 Hz considering a preheat temperature of $T_u = 673$ K and an adiabatic flame temperature of $T_b = 2070$ K. . . . .	102
9.3	Forced flame response for $\varphi = 0$ at a preheat temperature of $T_u = 673$ K and an air excess ratio of $\lambda_{\text{CH}_4} = 1.5$ at 3100 Hz of the MJC with pilot burner (left) and the comparison of the experimental flame response ( $\square$ ) to the flame response model (–) according to Eq. 5.22 for negligible turbulent dissipation (right) at the upper flames, indicated by the dashed line. . . . .	103

9.4	Validation of the axially resolved flame response model (–) with the phase-locked radially integrated HRR fluctuations of the experimental results (□) with pilot burner for natural gas. . . . .	105
9.5	Reconstructed acoustic pressure (left) and axial acoustic velocity field (right) in the injector tube using the two dynamic pressure sensors $T_1$ and $T_2$ . . . . .	106
9.6	Validation of the axially resolved flame response model (–) with the phase-locked radially integrated HRR fluctuations of the experimental results (□) without pilot burner for natural gas. . . .	107
9.7	Globally integrated HRR fluctuations (left) and simplified Rayleigh integral (right) for all phase bins for the MJC without pilot burner. . . . .	108
9.8	Validation of the axially resolved $FTF_x$ with the radially integrated experimental flame response for natural gas. . . . .	110
A.1	Sketch of the mass flow split between injector tubes and pilot burner (left) and the estimated pressure drop of the test rig (right).	116
A.2	Sketch of the pilot burner with the separation into the different pressure loss segments. . . . .	119
A.3	Sketch of the heat loss model (left) and the estimated burned gas and wall temperature of the combustor (right). . . . .	120

# List of Tables

7.1	Geometry of the generic experiment in [mm]	65
8.1	Geometry of the MJC with pilot burner in [mm]	72
8.2	Operating Conditions for the MJC with Pilot Burner	73
8.3	Numerical Domain and Boundary conditions	79
8.4	Geometry of the MJC without pilot burner in [mm]	91
8.5	Operating Conditions for the MJC without Pilot Burner	92
A.1	Natural gas composition according to the average of the year 2021 in munich.	115
A.2	Constants for the calculation of the emissivity of water - carbon-dioxide mixtures $\epsilon_{H_2O,CO_2}$ for $0.5 < \frac{p_{H_2O}}{p_{CO_2}} < 2$ .	122

# Nomenclature

## Latin Letters

$\hat{A}_r$	Radial Acoustic Pressure Field Amplitude [Pa <sup>1/3</sup> ]
$A$	Area [m <sup>2</sup> ]
$A_{mn}$	Effective Modal Acoustic Area [m <sup>2</sup> ]
$c$	Speed of Sound [m s <sup>-1</sup> ]
$c_i$	Molar Concentration of Species i [mol/m <sup>3</sup> ]
$c_p$	Isochoric Heat Capacity [J kg <sup>-1</sup> K <sup>-1</sup> ]
$c_F$	Molar Concentration of the Fuel Species [mol/m <sup>3</sup> ]
$C_r$	Reaction Progress Variable [-]
$d$	Diameter [m]
$d_P$	Diameter of the Plenum [m]
$d_T$	Diameter of the Injector Tubes [m]
$d_C$	Diameter of the Combustion Chamber [m]
$D$	Diffusion Coefficient [m <sup>2</sup> /s]
$E_{up}$	Upper Envelope of a non-dimensional Fluctuation [-]
$E_{low}$	Lower Envelope of a non-dimensional Fluctuation [-]
$E_a$	Integral Unsteady Change in Acoustic Energy [W]
$F_a$	Integral Flux of the Acoustic Energy [W]
$f$	Frequency [Hz]
$f_{T1}$	Cut-On Frequency of the T1 Mode [Hz]
$\hat{f}_x$	Amplitude of the Axially Downstream Propagating Acoustic Wave [Pa <sup>1/3</sup> ]
$\hat{f}_\theta$	Amplitude of the Azimuthally Positive Spinning Acoustic Wave [Pa <sup>1/3</sup> ]
$\hat{f}$	Lumped Amplitude of the Downstream Propagating Acoustic Wave [Pa]
$f(x)$	Downstream Propagating Acoustic Wave [Pa]
$\hat{g}_x$	Amplitude of the Axially Upstream Propagating Acoustic Wave [Pa <sup>1/3</sup> ]

$\hat{g}_\theta$	Amplitude of the Azimuthally Negative Spinning Acoustic Wave [Pa <sup>1/3</sup> ]
$\hat{g}$	Lumped Amplitude of the Downstream Propagating Acoustic Wave [Pa]
$g(x)$	Upstream Propagating Acoustic Wave [Pa]
$h$	Molar Specific Enthalpy [J mol <sup>-1</sup> ]
$H_u$	Mass-Specific Lower Caloric Heating Value [J kg <sup>-1</sup> ]
$I_{OH^*}$	Intensity of the Optical Chemiluminescence Measurements [-]
$J_n$	Bessel Function [-]
$k$	Acoustic Wavenumber [rad m <sup>-1</sup> ]
$k_\pm$	Axial Acoustic Wavenumber in Positive/Negative Direction [rad m <sup>-1</sup> ]
$k_{mn}$	Acoustic Wavenumber in Radial Direction [rad m <sup>-1</sup> ]
$k_{conv}$	Convective Wavenumber [rad m <sup>-1</sup> ]
$k_{diff}$	Convective-Diffusive Wavenumber [rad m <sup>-1</sup> ]
$k_{shear}$	Convective-Diffusive Wavenumber with Velocity Gradients [rad m <sup>-1</sup> ]
$L_P$	Length of the Plenum [m]
$L_T$	Length of the Injector Tubes [m]
$L_C$	Length of the Combustion Chamber [m]
$L_{eff}$	Effective Acoustic Length [m]
$l_t$	Turbulent Length Scale [m]
$\tilde{l}$	Minimal Molar Air Requirement [-]
$M$	Mach Number [-]
$M_F$	Molar Mass of the Fuel [kg mol <sup>-1</sup> ]
$m$	Order of the Mode in Azimuthal Direction [-]
$\dot{m}$	Mass flow rate [kg s <sup>-1</sup> ]
$n$	Order of the Mode in Radial Direction [-]
$n_{Fl}$	Flame Front Normal Vector [-]
$n_{a \rightarrow v}$	Hydrodynamic Gain [-]
$P_{th}$	Thermal Power [W]
$P_m$	Azimuthal Ansatz Function of the Acoustic Field [-]
$p'$	Real-Valued Acoustic Pressure [Pa]
$\tilde{p}$	Time-Dependent Complex-Valued Acoustic Pressure [Pa]
$\hat{p}$	Complex-Valued Acoustic Pressure [Pa]
$\hat{p}_{mn}$	Complex-Valued Modal Acoustic Pressure [Pa]
$\dot{Q}$	Global Heat Release Rate [W]
$\dot{\hat{Q}}_{mn}$	Global Modal Heat Release Rate Fluctuations [W]

---

$\hat{Q}_{mn,x}$	Axially Resolved Modal Heat Release Rate Fluctuations [ $\text{W m}^{-1}$ ]
$\dot{q}$	Heat Release Rate Density [ $\text{W/m}^3$ ]
$\hat{q}$	Complex-Valued Heat Release Rate Density Fluctuation [ $\text{W/m}^3$ ]
$\tilde{q}$	Time-Dependent Heat Release Rate Density Fluctuation [ $\text{W/m}^3$ ]
$r$	Radial Coordinate [m]
$r_T$	Radial Displacement from the Centre Line of the Injector Tubes [m]
ri	Rayleigh Index [ $\text{PaW/m}^3$ ]
RI	Rayleigh Integral [PaJ]
$R_\theta$	Acoustic Pressure Reflection Coefficient in Azimuthal Direction [-]
$\dot{S}_a$	Integral Source in Acoustic Energy [W]
$s_d$	Displacement Speed of the Flame Front [ $\text{m s}^{-1}$ ]
$s_t$	Turbulent Flame Speed [ $\text{m s}^{-1}$ ]
$u$	Mass-Specific Internal Energy [ $\text{J kg}^{-1}$ ]
$\mathbf{u}$	Velocity Vector [ $\text{m s}^{-1}$ ]
$u_i$	Velocity Component [ $\text{m s}^{-1}$ ]
$u'$	Real-Valued Acoustic Velocity [ $\text{m s}^{-1}$ ]
$u'_t$	Stochastic Turbulent Velocity Fluctuations [ $\text{m s}^{-1}$ ]
$\hat{u}_{mn}$	Complex-Valued Modal Axial Acoustic Velocity [ $\text{m s}^{-1}$ ]
$u'_{r,\theta}$	Real-Valued Acoustic Velocity in Radial and Azimuthal Direction [ $\text{m s}^{-1}$ ]
$\hat{u}$	Complex-Valued Acoustic Velocity [ $\text{m s}^{-1}$ ]
$\tilde{u}$	Time-Dependent Complex-Valued Acoustic Velocity [ $\text{m s}^{-1}$ ]
$\hat{u}_{\text{ref}}$	Complex-Valued Acoustic Velocity at the Reference Position [ $\text{m s}^{-1}$ ]
$\bar{u}_{\text{ref}}$	Axial Mean Flow Velocity at the Reference Position [ $\text{m s}^{-1}$ ]
$\hat{u}_{v,n}$	Vortical Velocity Fluctuations Normal to the Flame Front [ $\text{m s}^{-1}$ ]
$\tilde{v}$	Molar Exhaust Amount [-]
$x$	Axial Coordinate [m]
$\mathbf{x}$	Spatial Coordinate Vector [m]
$\bar{x}_{\dot{q}}$	Weighted Axial Mean Position of the Heat Release Distribution [m]
$Y$	Mass Fraction [-]
$z$	Normed Acoustic Impedance [-]

## Transfer Functions and Matrices

ftf	Locally Resolved Flame Transfer Function
FTF	Global Flame Transfer Function
FTF <sub>x</sub>	Axially Resolved Flame Transfer Function
FTM	Flame Transfer Matrix in p-u Notation
SM <sub>fg</sub>	Scattering Matrix in f-g Notation
TM <sub>pu</sub>	Transfer Matrix in p-u Notation
TM <sub>fg</sub>	Transfer Matrix in f-g Notation

## Greek Letters

$\alpha_{mn}$	Argument of the Bessel Function [-]
$\alpha_g$	Growth Rate of the Instability [Hz]
$\alpha$	Heat Transfer Coefficient [W/m <sup>2</sup> /K]
$\alpha_{\dot{q}}$	Skewness Factor of the Heat Release Distribution [-]
$\delta$	Kronecker Delta [-]
$\epsilon$	Emissivity [-]
$\zeta$	Pressure Loss Coefficient [-]
$\theta$	Azimuthal Angle [rad]
$\theta_T$	Azimuthal Angle of the Injector Tubes [rad]
$\theta_m$	Transverse Nodal Line Angle [rad]
$\kappa$	Heat Capacity Ratio [-]
$\kappa_{\pm}$	Non-Dimensional Axial Wavenumber in Positive/Negative Direction [-]
$\lambda$	Acoustic Wavelength [m]
$\lambda_{\text{fuel}}$	Air Excess Ratio of the Fuel [-]
$\lambda_{\text{cond}}$	Thermal Conductivity Coefficient [Wm <sup>-1</sup> K <sup>-1</sup> ]
$\mu$	Dynamic Viscosity [Pa s <sup>-1</sup> ]
$\nu$	Kinematic Viscosity [m <sup>2</sup> /s]
$\nu_t$	Turbulent Viscosity [m <sup>2</sup> /s]
$\nu_i$	Stoichiometric Coefficient of species i [-]
$\xi$	Axial Mean Heat Release Distribution [m <sup>-1</sup> ]
$\Pi$	Non-Dimensional Acoustic Pressure Field [-]

$\rho$	Fluid Density [kg/m <sup>3</sup> ]
$\sigma_{\text{Fl}}$	Flame Surface Density [m <sup>-1</sup> ]
$\sigma_{\tau}$	Variance of the Time Delay [s]
$\sigma_{\dot{q}}$	Variance of the Axial Position of the Heat Release Distribution [m]
$\tau_{ij}$	Shear Stress Tensor [Pa]
$\tau_{\dot{q}}$	Time Delay of the Heat Release Response [s]
$\varphi$	Phase of the Temporal Oscillation [rad]
$\omega$	Angular Frequency [rad s <sup>-1</sup> ]
$\dot{\omega}_r$	Molecular Reaction Rate [mol/m <sup>3</sup> /s]
$\dot{\Omega}_r$	Normalised Molecular Reaction Rate [s <sup>-1</sup> ]
$\dot{\Omega}_t$	Normalised Turbulent Reaction Rate [s <sup>-1</sup> ]

## Indices

<i>A</i>	Cross-Sectional Area Change
<i>a</i>	Acoustic
<i>b</i>	Burned Gas
<i>c.o.</i>	Cut-On Condition
<i>C</i>	Combustion Chamber
<i>D</i>	Duct
<i>do</i>	Downstream
<i>e</i>	Entropy
<i>eq</i>	Equivalent
<i>ex</i>	Exhaust
<i>F</i>	Fuel
<i>Fl</i>	Flame
<i>g</i>	Gas
<i>h</i>	Hydraulic
<i>img</i>	Image
<i>jet</i>	Jet Flames
<i>mn</i>	Normalised With the Acoustic Field in Cross-Sectional Direction
<i>off</i>	Offset
<i>P</i>	Plenum

<i>pilot</i>	Pilot Flame
<i>r</i>	Reaction
<i>ref</i>	Reference Position at the Injector Section Exit
<i>t</i>	Stochastic Turbulence
<i>tot</i>	Total
<i>T</i>	Injector Tube
<i>u</i>	Unburned
<i>up</i>	Upstream
<i>v</i>	Coherent Vortical Turbulent Structures
<i>vc</i>	Vena Contracta
<i>W</i>	Wall

## **Abbreviations**

**CFD/CAA** Computational Fluid Dynamics/Computational Aeroacoustics

**DLR** German Aerospace Center

**DF** Downstream Forcing

**HF** High Frequency

**HRR** Heat Release Rate

**LF** Low Frequency

**MJC** Multi-Jet-Combustor

**MMM** Multi-Microphone-Method

**ODE** Ordinary Differential Equation

**PDE** Partial Differential Equation

**SR** Spin Ratio

**UF** Upstream Forcing



# 1 Introduction

The energy transition in power generation and aviation is crucial due to the high amount of greenhouse gas emissions. Full electrification or the use of fuel cells is limited to medium-sized aeroplanes. Moreover, the volatility of wind and solar energy requires flexible solutions to avoid temporary loss in power generation. Modern premix gas turbines provide a robust and flexible solution to reach the goal of net-zero carbon dioxide production. Low emissions and fuel flexibility between pure natural gas and hydrogen operation are required. Besides carbon dioxide emissions, the formation of  $\text{NO}_x$  must be maintained at current levels or even reduced, although turbine inlet temperatures are increasing for higher thermodynamic efficiency. The lean premixed combustor concept addresses these challenging technical requirements. Specifically, Multi-Jet-Combustor (MJC)'s are a promising combustor concept for hydrogen application due to their reduced risk of flame flashback and low  $\text{NO}_x$  emissions.

## 1.1 Combustor Concept

MJC's are a lean premixed, low emission, gas turbine combustor concept originating from the FLOX<sup>®</sup>-concept with flameless oxidation of premixed fuel and air. Multiple, small, premixed jets are assembled in a can combustor yielding much lower residence times (i.e. low  $\text{NO}_x$ ) than the established single swirl-stabilised flames. Under conditions similar to gas turbine engines, however, flameless oxidation cannot be achieved. Instead, deflagrative turbulent flame stabilisation in the shear layer yields multiple jet flames with fast burnout and low combustor residence time [1,2]. In the present thesis, a low-emission MJC with gas turbine similar operation conditions is designed and investigated experimentally under perfectly premixed conditions. The advances of lean pre-

mixed combustor concepts with increased turbine inlet temperatures include significant technical difficulties. Susceptibility to instabilities, such as flame flashback or thermoacoustic instabilities, increases for lean premixed flames. Flashback and Low Frequency (LF) thermoacoustic instabilities have been researched in gas turbine engines for decades [3, 4]. High Frequency (HF) thermoacoustic instabilities, however, reveal a substantial lack of knowledge concerning gas turbine combustors.

The considered MJC configuration is sketched in Fig. 1.1 including the plenum (index: P), eight injector tubes (index: T) and the combustion chamber (index: C). The relevant geometrical parameters depicted in Fig. 1.1 contain the plenum, injector tube and combustion chamber lengths  $L_P, L_T, L_C$  and diameters  $d_P, d_T, d_C$ . Moreover, the position of each individual injector tube is indicated by the radial displacement from the centre line  $r_T$  and the azimuthal angle  $\theta_T$ . Technical MJC configurations in gas turbine and rocket engines consist of multiple rows of injector tubes [2, 5]. In order to obtain optical access to the flame response of the investigated MJC, a number of eight injector tubes is chosen that are evenly distributed in azimuthal direction within a single row. Especially the acoustic low order modelling approach in the present thesis depends primarily on the indicated geometrical parameters and is, therefore, applicable to multi-injector can combustors in gas turbines and rocket engines.

## 1.2 High Frequency Combustion Instabilities

Thermoacoustic instabilities are an interdisciplinary, thermo-fluid-dynamical scientific field, where complexity further increases considering HF modes. The occurrence of thermoacoustic instabilities depends on several factors, such as the type of combustion (premixed, diffusion, laminar, turbulent flames), the aerodynamics of the combustor (jet flow, swirl flow, pressure drop, turbulent dissipation) and the boundary conditions (combustor geometry, temperature gradients). Gas turbine combustors using premixed swirl flames of recent decades have shown less susceptibility to HF instabilities. Therefore, the existing literature is predominantly limited to LF thermoacous-

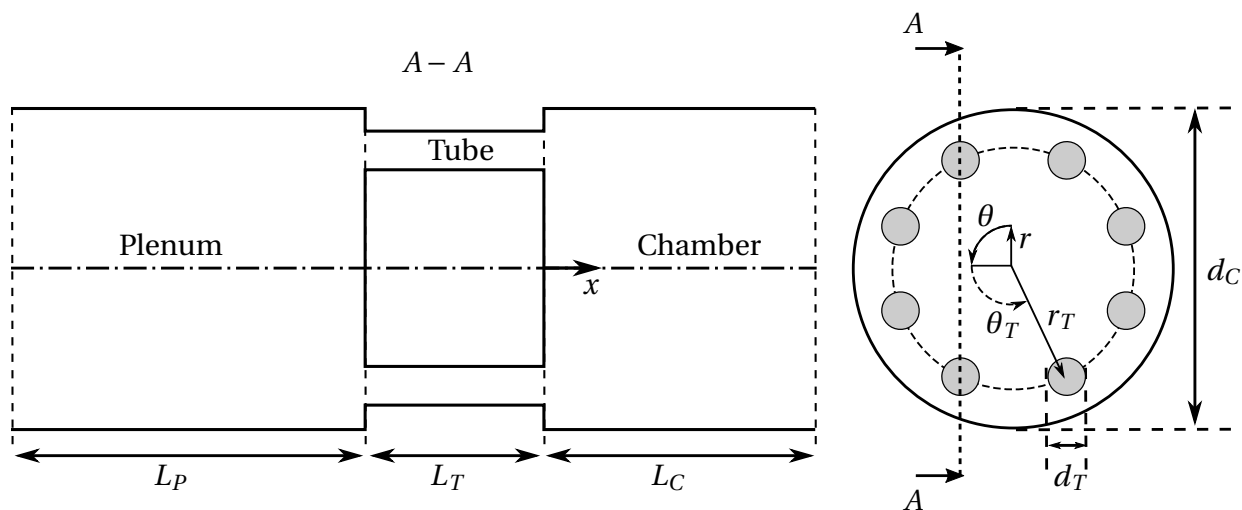


**Figure 1.1:** Sketch of the investigated MJC of the present thesis with the plenum, eight injector tubes and a combustion chamber of the respective lengths  $L_P, L_T, L_C$  and diameters  $d_P, d_T, d_C$  and the individual injector tube position  $r_T, \theta_T$ .

tic instabilities [3, 6, 9]. Modern premixed low-emission MJC's featuring higher power density and turbine inlet temperature show increased susceptibility to HF thermoacoustic instabilities [10], which might further increase using hydrogen. The knowledge of the underlying thermoacoustic driving mechanisms is crucial to developing predictive combustor design tools accounting for HF thermoacoustic instabilities. In this context, the RoboFlex project is funded by BMWK and Siemens Energy within the AG Turbo collaboration to investigate the fundamental HF flame-acoustic feedback mechanisms and provide predictive tools for the gas turbine industry.

HF thermoacoustic instabilities are a well-known threat in non-premixed rocket combustors with a similar MJC concept using multiple injectors arranged in several rows at the front plate. In particular, the Apollo mission rocket engine exhibited self-sustained HF combustion instabilities [7]. The high pressure gradients of the HF thermoacoustic mode lead to catastrophic consequences for the engine within seconds, as depicted on the left side of Fig. 1.2. Similar high-cycle fatigue failure of the space shuttle rocket engine's injector plate [8] yielded severe damage, as shown on the right side of Fig. 1.2.

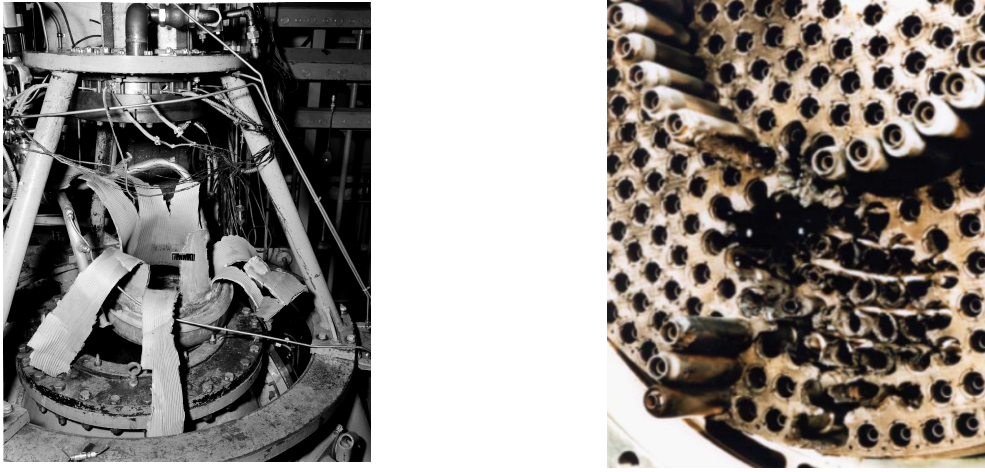


**Figure 1.2:** Apollo mission rocket combustor (left) and space shuttle injector face plate (right) after the occurrence of HF thermoacoustic instability during engine testing.

The acoustic boundary conditions are a crucial aspect considering the growth rate of thermoacoustic instabilities [3, 6, 10, 11]. Rocket engine combustor walls provide highly reflective boundary conditions in radial direction. The extremely high temperature gradient from unburned to burned gas conditions in rocket combustors favours evanescent, i.e. exponentially decaying, acoustic pressure mode shapes in the axial direction [16–18]. The variation in cut-on frequency for increased temperature yields the evanescent HF mode shape with highly reflective acoustic boundary conditions in axial direction, resulting in increased susceptibility for HF combustion instabilities in rocket engines. Similar highly reflective axial boundary conditions for evanescent wave propagation are present in gas turbine combustors if the temperature gradient and, thus, the variation in cut-on frequency is sufficient. Additionally, possible secondary air inlets are omitted in lean premixed gas turbine concepts, which further contribute to reflective boundary conditions in the radial direction. Thus, susceptibility to HF thermoacoustic instabilities increases [10].

Besides the acoustic boundary conditions, the proper prediction of the acoustic pressure mode shape  $p'$  and the local flame response, i.e. the HRR density fluctuations  $\dot{q}'$ , are of first-order importance. The volume source in acoustic energy driving the instability is determined by the local Rayleigh index  $p'\dot{q}'$

[12], i.e. the product of acoustic pressure and HRR density fluctuations. Extensive experimental and numerical investigations of HF instabilities in rocket engines emphasise the significance of coherent acoustically triggered vortex shedding in the flame shear layer [5, 13–16] to the flame response and thus the local Rayleigh index  $p'\dot{q}'$ . LES results of Urbano et al. [17, 18] further indicate a substantial decrease in the flame length during the thermoacoustic limit cycle due to increased transverse velocity fluctuations. Consequently, the flame becomes convectively more compact, leading to a higher global gain of the convective driving mechanisms in the HF regime due to a lower compensation of positive and negative HRR fluctuations in main flow direction. Concerning lean premixed gas turbine combustors, HF instability driving mechanisms are a relatively new field. Existing experimental and numerical investigations for swirl-stabilised flames [19–21] revealed a periodic displacement and compression of the flame in phase with the transverse acoustic field. Acoustic flame displacement and acoustic flame compression are identified as possible HF driving mechanisms solely dependent on the instantaneous acoustic field [22,23]. However, the open literature on HF instabilities in rocket engines and recent experimental results on lab-scale gas turbine combustors emphasise the importance of additional convective driving mechanisms that may dominate the flame response. The existing literature on possible convective driving mechanisms for HF thermoacoustic instabilities is reviewed in the next section with focus on perfectly premixed fuel and air in gas turbine engines.

### 1.3 Convective Flame Response

The convective flame response is the predominant thermoacoustic driving mechanism in the LF regime [3, 6]. Acoustic velocity fluctuations at the dump plane are the origin of the perfectly premixed flame response, leading to reaction rate fluctuations at the flame front. Premixed combustion modelling splits the reaction rate in the flame surface density and a laminar or turbulent flame speed [24]. Therefore, the superimposed contribution of turbulent flame speed and acoustic flame area perturbations is often proposed concern-

ing combustor stability analysis in literature [3,25]. Turbulent flame speed and flame area perturbations originate from the acoustic velocity fluctuations at the dump plane. Acoustic velocity fluctuations induce a direct acoustic displacement of the flame surface. Acoustically triggered large-scale vortex shedding at the dump plane yields an indirect perturbation of the flame since a transfer of the acoustic velocity into local coherent vortical velocity fluctuations is required. The acoustic and vortical coherent velocity fluctuations are both convected with the mean flow along the flame surface, resulting in local reaction rate fluctuations. Two main approaches to model the convective reaction rate fluctuations are present in literature: kinematic flame area models and the semi-empirical  $n - \tau - \sigma$  approach.

The existing literature on kinematic flame area response models provides fundamental insights into the non-compact flame response of jet flames. First models were developed for laminar flames by Fleifil [26, 27] and extended to turbulent flames by Dowling et al. [28]. The kinematic model provided by Ducruix et al. [29] in the LF limit is extended by Schuller et al. [30] to capture the gain and phase of the flame transfer function for higher frequencies. Although a single laminar jet flame with longitudinal acoustic forcing is considered by Schuller et al., the extracted insights on the HF limit of the flame response are particularly interesting concerning the modelling objectives of the thesis for turbulent jet flames in MJC's. The results of Schuller et al. stress two main effects to be considered for higher frequencies: 1. the convective non-compactness of the flame and 2. the variation in the mean flow field along the flame length. The convective compactness may be characterised by the convective wavelength  $\lambda_{\text{conv}} = \bar{u}/f$  given by the frequency  $f$  and the predominant axial mean flow velocity  $\bar{u}$  in relation to the flame length  $L_{\text{Fl}}$ . For higher frequencies, the convective wavelength is smaller than the flame length  $\lambda_{\text{conv}} \ll L_{\text{Fl}}$  and the phase of the convective HRR density fluctuations varies along the extent of the flame, which is crucial for the global flame response gain and phase.

The semi-empirical  $n - \tau - \sigma$  approach accounts for the interaction of coherent velocity fluctuations and the heat release by an empirically determined interaction index  $n$ . Dowling [28] derives the analytical expression for the in-

teraction index based on a kinematic flame area response model. However, the gain is commonly obtained by an empirical fit to experiments. The flame is assumed acoustically compact  $\lambda_a \gg L_{\text{Fl}}$  such that solely the integral heat release fluctuations are measured. The time delay is generally predictable with knowledge of the mean flow field and the mean flame position. Although acoustically compact, the flame might be convectively non-compact  $\lambda_{\text{conv}} \approx L_{\text{Fl}}$ . The convective non-compactness is accounted by the distribution of the time delay with the variance  $\sigma_{\dot{q}}$  around the mean time delay  $\bar{\tau}_{\dot{q}}$  [9, 31, 32]. The present thesis proposes a generalised, semi-empirical approach regarding fully non-compact flame dynamics.

Although the convective flame response is a primary driving mechanism for HF combustion instabilities in rocket engine combustors [17, 18], they are often assumed negligible for HF dynamics in premixed gas turbine engines. This assumption might be justified by the high degree of dissipation of convective fluctuations in the injector section with an increasingly shorter convective wavelength and the associated decreasing gain of the flame transfer function [32]. Instead of convective response mechanisms, local coupling models for HF flame dynamics, namely flame displacement and compression, are established mechanisms deduced from premixed experiments on swirl flames [20–23]. Recent experimental results, however, emphasise the importance of coherent vortex shedding for HF instabilities in gas turbine combustors. Buschhagen et al. [33] provide experimental insights on the contribution of flame area perturbation due to acoustic velocity fluctuations or due to coherent turbulent velocity fluctuations for a longitudinal instability. The Strouhal number, i.e. the frequency dependency of a longitudinal self-sustained combustion instability in a single jet flame test rig, reveals acoustic velocity perturbations as the dominant flame response at low frequencies. However, large-scale vortex structures dominate the flame response at higher frequencies, leading to coherent turbulent velocity fluctuations at the flame front. Buschhagen et al. investigated a single jet flame at elevated pressure [34] that exhibits a self-sustained first transverse thermoacoustic instability including heat release fluctuations caused by coherent vortex shedding. Philo et al. [35] provide experimental results of a self-sustained first transverse combustion instability in a rectangular MJC under elevated pressure associ-

ated with strong injector coupling, resulting in convective heat release rate fluctuations due to coherent vortex shedding. McClure et al. [36] investigated a self-sustained first transverse mode in an atmospheric rectangular reheat combustor jet flame. Coherent shear layer modulation is identified as the root cause of the self-sustained first transverse mode. Experimental results with compact hydrogen flames in an atmospheric multi-slit combustor test rig by Lee et al. [37] show a self-sustained first transverse mode. The MJC investigated by the German Aerospace Center (DLR) group, as presented by Lamme et al. [1], exhibits a self-sustained transverse instability when operated with certain amounts of hydrogen-natural gas mixture at elevated pressure as also numerically investigated by Grimm et al. [38]. Additional numerical LES studies of Sharifi et al. provide insights into a single jet flame with a self-sustained first radial mode [39, 40] and the presence of a possible convective driving mechanism. Shipley et al. [41] investigated the rectangular MJC used by Philo et al. and demonstrated the dominant contribution of coherent vortex shedding due to transverse and axial acoustic velocity fluctuations to the flame response.

In summary, fundamental experimental insights on HF instabilities in gas turbine combustors are provided within the review by O'Connor et al. [10] and also within more recent literature [33–36, 39, 41, 42]. The mentioned investigations emphasise the significance of convective driving mechanisms for HF combustion instabilities in premixed gas turbine combustors and the crucial role of injector coupling in MJC. Moreover, the results outline the predominant occurrence of the T1 mode. The T1 mode is the first transverse HF mode with the lowest cut-on frequency, which outlines a low pass behaviour typical for convective driving mechanisms. However, the provided results are limited to generic rectangular, annular or can-annular combustors. In these cases, it is unclear whether the observed effects are representative of HF modes in can combustors. Also, non-linear limit cycle behaviour highly determines the flame response of self-sustained experiments and LES simulations. Therefore, additional experimental insights on the forced flame response are required to deduce linear thermoacoustic driving models for combustor stability analysis, as provided in the present thesis.

## 1.4 Combustor Stability Analysis

As reviewed above, cost-intensive, brute-force numerical LES simulations or experiments yield detailed insights into HF thermoacoustic instabilities. Low order modelling frameworks are required to adequately interpret LES simulations and experiments. Moreover, thermoacoustic instabilities are one of many technical challenges in combustor design and therefore, efficient analytical pre-design tools are necessary.

Two efficient and established methods to predict thermoacoustic instabilities early in design exist: the hybrid Computational Fluid Dynamics/Computational Aeroacoustics (CFD/CAA) and the low order network method, both considered in the thesis. The state-of-the-art stability analysis method covering transverse modes is the hybrid CFD/CAA method. The linearised Navier-Stokes equations, the Euler equation or the Helmholtz equation are solved numerically [43–46] covering three-dimensional acoustic wave propagation. In the LF regime, low order networks using measured or analytical two-port transfer matrices are an established modelling approach in the acoustic literature [47] and have become common practice in the last decades for longitudinal thermoacoustic modes in can combustors [6, 48]. The low order network method is extended to cans in annular combustors using three-dimensional acoustic wave numbers [49–52]. Progress concerning the analytical prediction of thermoacoustic instabilities in annular and can-annular combustors is reviewed by Bauernheim et al. [53]. The current status of science concerning the HF thermoacoustic instabilities in can combustors is reviewed by O'Connor et al. [10]. It is noted that progress in analytical modelling concerning HF mode coupling in multi-injector can combustors and the flame response is required. Dowling et al. [54] and You et al. [55] provide a notable contribution concerning analytical methods on HF thermoacoustic in gas turbine combustors. However, the modelling of HF transfer matrices is limited to multi-port transfer matrices [56, 57] yielding rather complex thermoacoustic models [55]. These multi-port transfer matrices include various unknowns that have to be determined and interpreted. Thus, the application of low order network models to HF thermoacoustic combustor stability anal-

ysis requires improvement. Therefore, an extended two-port transfer matrix theory covering HF modes in can combustors is suggested in the present thesis.

Both the low order network and the hybrid CFD/CAA method require a flame response model covering the HRR density fluctuations, i.e. the local fluctuations in heat release rate per unit volume, which are not yet fully understood. The investigation of fundamental thermoacoustic driving mechanisms and the deduction of local driving models coupling the acoustic field variables, acoustic pressure and velocity to the heat release rate fluctuations are major challenges. HF modes require a locally distributed flame response model to adequately predict the driving potential of the instability. Distributed time delay models are an established approach in the LF limit to model the convective non-compact yet acoustically compact flame response as reviewed by Polifke et al. [9]. Locally distributed models in the LF case are limited to the coupling of multiple compact flames [58] or numerical CFD/CAA models assuming a constant gain and phase over the extent of the flame [44–46, 59].

The prediction of the combustor acoustics covering the wave propagation through ducts, area changes and the boundary conditions is a crucial open aspect considering low order models for HF modes. In complex real-engine applications theory and analytical methods, paradoxically, become increasingly important for the interpretation of experiments and LES simulations and for the extraction of possible mitigation strategies for thermoacoustic instabilities [11]. The reviews of O'Connor et al. [10] and Bauerheim et al. [53] provide insights on analytical methods for HF instabilities and stress the importance of the dominant convective flame response mechanism, similar to rocket engines [17, 18]. Nevertheless, a fundamental lack of knowledge on reduced and analytical modelling and a consistent theoretical framework on HF combustion instabilities, especially concerning multi-injector can combustors, is present in the literature.

## 1.5 Thesis Outline

The present thesis contributes to the fundamental understanding of HF thermoacoustic instabilities in can combustors. The thesis can be divided into three main contributions on perfectly premixed HF jet flame dynamics,

1. the derivation and validation of a distributed convective flame response model,
2. the derivation and validation of a generalised low order network model and
3. the experimental investigation of the flame response to the forced T1 mode.

The transverse to longitudinal injector-coupling and the resulting convective flame response of natural gas and hydrogen jet flames is investigated in a forced response, atmospheric MJC experiment. Special emphasis is on the development of analytical low order methods for HF thermoacoustic combustion instabilities.

The thesis begins with the necessary fundamentals for understanding HF thermoacoustic instabilities concerning premixed jet flames in MJC's in Chapters 2 and 3. Chapter 4 includes the common experimental and numerical methods used in this work and provides the post-processing of the phase-locked images, the acoustic field reconstruction using the dynamic pressure measurements and the CFD/CAA methodology. Chapter 5 contains the derivation of the flame response model including the locally resolved convective reaction rate fluctuations at the flame front, extending the existing  $n-\tau-\sigma$  approach to HF thermoacoustics. The flame response model is applied to the CFD/CAA method and the HF network model derived in Chapter 6. The generalised network theory in Chapter 6 includes HF transfer matrices for a straight duct, an area change and a flame. The non-reactive transfer matrices are validated in Chapter 7. The experimental investigation of the perfectly premixed forced flame response in Chapter 8 reveals the significant HF driving mecha-

nisms in the atmospheric MJC. The detailed validation of the axially resolved flame response model is provided in Chapter 9.

## 2 Governing Equations

The relevant theoretical fundamentals for the experimental investigation and the modelling are provided in this section. The Navier-Stokes equations, i.e., the conservation of mass and momentum as well as the energy and species conservations, are introduced in their non-linear, general form. Correctly estimating the unburned and burned gas properties is crucial for evaluating the experiments and the proposed coupling models. Therefore, the global, one-step combustion reaction equation and the estimated adiabatic flame temperature and gas properties are discussed briefly. The chapter concludes with the c-equation approach of premixed combustion modelling, providing the basis for the convective flame response model in the present thesis.

### 2.1 Governing Conservation Equations

The governing equations are given by the conservation of mass and momentum expressed via the density  $\rho$ , the velocity  $u_i$ , the pressure  $p$ , the stress tensor  $\tau_{ij}$  and external forces  $f_i$

$$\frac{d\rho}{dt} + \rho \frac{\partial u_i}{\partial x_i} = 0, \quad (2.1)$$

$$\rho \frac{du_i}{dt} + \frac{\partial p}{\partial x_i} = \frac{\partial \tau_{ij}}{\partial x_j} + \rho f_i. \quad (2.2)$$

The material derivative denoted with  $\frac{d}{dt}$  in a Lagrangian frame of reference implies a local unsteady and convective transport term  $\frac{d}{dt} = \frac{\partial}{\partial t} + u_j \frac{\partial}{\partial x_j}$  in the Eulerian frame of reference. For a Newtonian fluid the stress tensor is expressed via the dynamic viscosity  $\mu = \frac{\nu}{\rho}$  which yields  $\tau_{ij} = \mu \left( \frac{\partial u_i}{\partial x_j} + \frac{\partial u_j}{\partial x_i} - \frac{2}{3} \delta_{ij} \frac{\partial u_k}{\partial x_k} \right)$ . The stress tensor term in the Navier-Stokes equations yields the common simplifi-

cation  $\tau_{ij} = \mu \frac{\partial u_i}{\partial x_j}$  for an incompressible Newtonian fluid. The conservation of species in the form of the mass fraction  $Y_i$  yields

$$\frac{dY_i}{dt} + Y_i \frac{\partial u_j}{\partial x_j} = \frac{\partial}{\partial x_j} \left( D_i \frac{\partial Y_i}{\partial x_j} \right) + \underbrace{\frac{M_i}{\rho} \sum_r \nu_i \dot{\omega}_r}_{\dot{\omega}_i}, \quad (2.3)$$

which includes the convective transport, molecular diffusion and a volumetric source term  $\dot{\omega}_i$  due to chemical reaction. In general, finite rate chemistry predicts the local reaction rate by the change in molar concentration  $\frac{dc_i}{dt}$  of a species  $i$  by the sum of all chemical reactions  $\frac{dc_i}{dt} = \sum_r \nu_i \dot{\omega}_r$  weighted with the stoichiometric coefficient  $\nu_i$ . The energy conservation accounts for the change of the internal energy  $u$  depending on the translational, rotational and vibrational energy stored on the molecular level and the kinematic energy stored on the continuum, fluid dynamical level:

$$\rho \frac{du + \frac{1}{2} u_i^2}{dt} + \frac{\partial u_j p}{\partial x_j} = - \underbrace{\sum_r \dot{\omega}_r \sum_i \Delta h_i \nu_i}_{\dot{q}_r} + \frac{\partial}{\partial x_j} \left( \lambda_{\text{cond.}} \frac{\partial T}{\partial x_j} \right) + \frac{\partial (\tau_{ij} u_j)}{\partial x_i}. \quad (2.4)$$

The left-hand side of the energy conservation contains the unsteady change in internal and kinetic energy and the energy flux. The right-hand side contains the volumetric heat release rate due to chemical reaction, heat conduction and viscous losses. Note that sources of heat radiation and external forces are neglected. The HRR density due to chemical reaction  $\dot{q}_r$  is coupled to the species balance

$$\dot{q}_r = - \sum_r \dot{\omega}_r \left( \underbrace{\sum_i \Delta h_i \nu_i}_{\Delta_r h} \right), \quad (2.5)$$

via the weighted sum of the formation enthalpies  $\Delta h_i$  by the stoichiometric coefficients  $\nu_i$  of all species in all chemical reactions, which yields the reaction enthalpy  $\Delta_r h$ .

Various forms of the energy equation exist, expressed by the enthalpy, the entropy, temperature or pressure. The pressure form is particularly helpful in

numerical [4, 60] and analytical thermoacoustic modelling [3, 6]. The derivation of the energy conservation in pressure form [4] requires the subtraction of the kinetical energy balance, i.e. the momentum conservation multiplied by  $u_i$  from the total energy Eq. 2.4 and the substitution of the internal energy by  $du = c_v dT$  for an ideal gas  $p = \rho R_s T$ . Use of the relation of the ideal gas constant to the isochoric and isobaric mass-specific heat capacities  $R_s = c_p - c_v = c_v(\kappa - 1)$  by the heat capacity ratio  $\kappa = c_p/c_v$  yields the internal energy as function of the pressure  $\rho du = \frac{dp}{\kappa-1}$  and the energy conservation in pressure form

$$\frac{1}{\kappa - 1} \frac{dp}{dt} + \frac{\kappa p}{\kappa - 1} \frac{\partial u_j}{\partial x_j} = \dot{q}_r + \frac{\partial}{\partial x_i} \left( \lambda_{\text{cond.}} \frac{\partial T}{\partial x_j} \right) + \tau_{ij} \frac{\partial (u_j)}{\partial x_i} \quad (2.6)$$

is obtained. Equation 2.6 contains the dependency of the local pressure on the heat release rate.

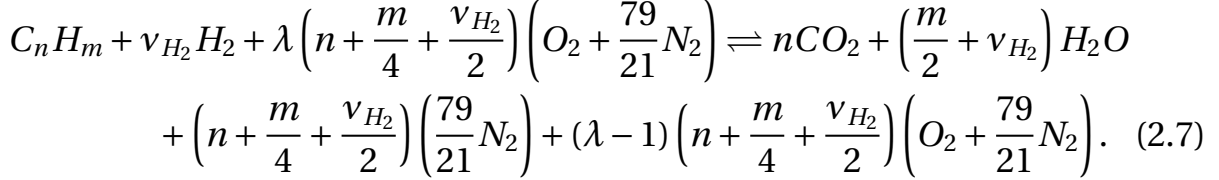
The Navier-Stokes equations Eqs. 2.1 and 2.2 provide the fundamentals for the entire linearised acoustic and hydrodynamic stability analysis framework in the present thesis. The species conservation Eq. 2.3 is used in the following to obtain the C-equation for premixed combustion at the end of this Chapter. The pressure form of the energy conservation according to Eq. 2.6 provides the coupling of the local pressure to the local volumetric heat release rate and is thus used to deduce the inhomogeneous thermoacoustic wave equation in Chapter 3.

## 2.2 Global Combustion Reaction

The single-step global combustion reaction is a highly simplified yet beneficial physical model of the complex reaction mechanisms associated with combustion. The assumption of full conversion is justified for the engine-similar conditions in the present thesis with burned gas temperatures of  $T_b \approx 2000$  K.

The global combustion reaction considering a gas mixture of methane,

ethane, propane and hydrogen yields



The minimal molar air requirement  $\tilde{l}_{\min}$   $\left[ \frac{\text{kmol}_{\text{air}}}{\text{kmol}_F} \right]$  and the equivalent minimal molar exhaust amount  $\tilde{\nu}_{\text{ex},\min}$   $\left[ \frac{\text{kmol}_{\text{ex},\min}}{\text{kmol}_F} \right]$

$$\tilde{l}_{\min} = \left( n + \frac{m}{4} + \frac{\nu_{H_2}}{2} \right) \left( 1 + \frac{79}{21} \right), \quad (2.8)$$

$$\tilde{\nu}_{\text{ex},\min} = n + \frac{m}{2} + \nu_{H_2} + \left( n + \frac{m}{4} + \frac{\nu_{CO}}{2} + \frac{\nu_{H_2}}{2} \right) \frac{79}{21}, \quad (2.9)$$

are introduced to reduce the integral balance equations to the dependency on the air excess ratio  $\lambda$  and one lumped fuel and exhaust component. The mass-specific minimal air requirement and minimal amount of exhaust  $l_{\min} = \tilde{l}_{\min} \frac{M_{\text{air}}}{M_u}$ ,  $\nu_{\min} = \tilde{\nu}_{\text{ex},\min} \frac{M_{\text{ex}}}{M_u}$  is helpful to determine the mass and energy conservation in the following. The overall mass flow rate  $\dot{m}$  is obtained from the conservation of mass considering Eq. 2.7 and thus a complete conversion of the unburned mass flow  $\dot{m}_u$  to the burned mass flow  $\dot{m}_b$  which yields

$$\dot{m} = \underbrace{\dot{m}_F (1 + \lambda l_{\min})}_{\dot{m}_u} = \underbrace{\dot{m}_F (\nu_{\text{ex},\min} + (1 - \lambda) l_{\min})}_{\dot{m}_b}. \quad (2.10)$$

The enthalpy conservation at constant pressure yields the local adiabatic flame temperature

$$T_b = T_u - \frac{\Delta_r h^0 + \Delta_r c_p (T_u - T_0)}{\Delta_r c_{p,b}} \quad (2.11)$$

including the temperature correction of the reaction enthalpy  $\Delta_r h = \Delta_r h^0 + \Delta_r c_p (T_u - T_0)$  using the stoichiometrically weighted species heat capacities  $\Delta_r c_p = \sum_{i=1}^n \nu_i \cdot c_{p,i}$  and the stoichiometrically weighted burned gas heat capacities  $\Delta_r c_{p,b} = (\lambda - 1) \tilde{l}_{\min} c_{p,\text{air}} + \tilde{\nu}_{\text{ex},\min} c_{p,\text{ex}}$ . Since the heat capacities depend on the temperature, an iterative solution is used to estimate the adiabatic

flame temperature. The equivalent expression using mass-specific heat capacities and the temperature-corrected lower heating value  $H_u = -\frac{\Delta_r h}{M_F}$  reads

$$T_b = T_u + \frac{Y_F H_u}{c_{p,b}}, \quad (2.12)$$

dependent on the unburned gas fuel mass fraction  $Y_F = \frac{\dot{m}_F}{\dot{m}}$  and the heat capacity of the burned gas.

The global combustion reaction according to Eq. 2.7 is used to evaluate the unburned and burned gas temperature, density, heat capacity ratio and the speed of sound at adiabatic conditions in the present thesis. The natural gas composition provided in the App. A.1 is used. The estimates are required for both the numerical simulations and the post processing of the experimental data. The associated adiabatic flame temperature is of particular interest for the proper evaluation of the speed of sound in the burned gas, which is crucial for the prediction of the acoustic field in the combustor. Moreover, the unburned gas density used to estimate the injector tube velocity is essential for the analysis of the experimental results and the modelling. The assumption of adiabatic conditions is justified with a steady-state, zero-dimensional heat loss estimation in App. A.3. The heat loss estimation includes convective heat transfer and heat radiation. For the investigated MJC operating conditions above a thermal power of  $\approx 150$  kW the heat loss results in a decrease in burned gas temperature of less than  $\approx 5\%$  considering natural gas combustion at  $\lambda_{\text{CH}_4} = 1.8$  and a preheat temperature of  $T_u = 673$  K.

Similar to the global combustion reaction equation, the simplified premixed combustion modelling approach describes the conversion of unburned fuel to burned gas with a single progress variable to access the locally resolved heat release of the flame, as discussed in the next section.

## 2.3 Premixed Turbulent Flames

Concerning HF thermoacoustics, a locally resolved flame response model is required, which is based on the C-equation for premixed combustion. The

fundamentals of the C-equation are discussed in this subsection according to premixed turbulent combustion literature [4, 24, 61].

The complexity of finite rate chemistry accounting for multiple reactions is reduced to a single non-dimensional reaction progress variable

$$C_r = \frac{Y_F - Y_{F,u}}{Y_{F,b} - Y_{F,u}}, \quad (2.13)$$

defined by the mass fraction of the fuel species  $Y_F$ . The flame is modelled as a propagating iso-surface of constant reaction progress. An irreversible one-step mechanism  $F + O \rightarrow P$  of the chemical reaction from unburned fuel (F) and oxidizer (O) to burned products (P) is assumed. Inserting Eq. 2.13 into the species conservation Eq. 2.3 yields the non-dimensional species conservation

$$\frac{dC_r}{dt} = \frac{\partial}{\partial x_j} \left( D_F \frac{\partial C_r}{\partial x_j} \right) + \dot{\Omega}_r. \quad (2.14)$$

The normalisation of the source term due to chemical reaction of the fuel species (Eq. 2.3) with the unburned fuel mass fraction  $\frac{\dot{\omega}_F}{Y_{F,u}} = \frac{M_F}{Y_{F,u}\rho} \sum_r \nu_F \dot{\omega}_r$  in combination with the molar fuel concentration  $c_{F,u} = \frac{\rho}{M_F} Y_F$  and the stoichiometric coefficient of the fuel  $\nu_F = -1$  for the one-step mechanism yields the normalised molecular reaction rate  $\dot{\Omega}_r = -\frac{\dot{\omega}_F}{c_{F,u}}$  introduced in Eq. 2.14. The right-hand side of Eq. 2.14 is rewritten, introducing the displacement speed  $s_d$  to finally obtain

$$\frac{\partial C_r}{\partial t} + u_j \frac{\partial C_r}{\partial x_j} = \underbrace{\frac{\frac{\partial}{\partial x_j} \left( D_F \frac{\partial C_r}{\partial x_j} \right) + \dot{\Omega}_r}{\left| \frac{\partial C_r}{\partial x_j} \right|}}_{s_d} \left| \frac{\partial C_r}{\partial x_j} \right|. \quad (2.15)$$

The transport equation of the progress variable is referred to as the C-equation (Eq. 2.15). The progress variable field represents the non-dimensional cumulative probability density distribution of the reaction zone. Thus, the flame surface density

$$\sigma_{Fl} = \left| \frac{\partial C_r}{\partial x_j} \right| = \sqrt{\left( \frac{\partial C_r}{\partial x_j} \right)^2}, \quad (2.16)$$

corresponds to the non-dimensional spatial probability density distribution of the flame surface [24]. Moreover, the flame surface normal vector  $n_{\text{Fl}}$  is introduced

$$n_{\text{Fl},j} = -\frac{\frac{\partial C_r}{\partial x_j}}{\sqrt{\left(\frac{\partial C_r}{\partial x_j}\right)^2}}, \quad (2.17)$$

which describes the spatial orientation of the iso-scalar surface  $C_r$ . The C-equation can be expressed via Eqs. 2.16 and 2.17, which yields

$$\frac{\partial C_r}{\partial t} = (s_d + \underbrace{u_j n_{\text{Fl},j}}_{u_n}) \sigma_{\text{Fl}}. \quad (2.18)$$

Thus, the C-equation describes the propagation of the iso-scalar surface  $C_r$  with the propagation speed of the flame surface given by the kinematic relation of the flame displacement speed  $s_d$  and the flame front normal convection velocity  $u_n = u_j n_{\text{Fl},j}$ . Concerning turbulent combustion, the statistical time-average of the progress variable in the C-equation 2.15 has to be considered. In the turbulent case, the diffusion coefficient  $D_F$  might be dominated by turbulent transport which is accounted by the turbulent flame speed  $s_t$ , neglecting curvature and molecular diffusion [24,61]. The turbulent flame speed  $s_t$  and the flame surface density  $\sigma_{\text{Fl}}$  yield the normalised turbulent reaction rate

$$\dot{\Omega}_t = s_t \sigma_{\text{Fl}}, \quad (2.19)$$

as the volume source term in the C-Equation (Eq. 2.15). The right-hand side of the energy conservation (Eq. 2.4 and 2.6) is commonly expressed with the normalised turbulent reaction rate considering a turbulent Lewis-number of unity [4,24,61] according to Eq. 2.19 which yields the local HRR density closure

$$\dot{q} = \rho \dot{\Omega}_t Y_F H_u, \quad (2.20)$$

based on the turbulent flame speed and the flame surface density as frequently used in thermoacoustic low order models [25, 32, 62]. The local HRR density  $\dot{q}$  depends on the density  $\rho$ , the normalised turbulent reaction rate  $\dot{\Omega}_t$ , the fuel mass fraction  $Y_F$  and the caloric heating value  $H_u = -\frac{\Delta_r h}{M_F}$ .

The fundamentals of the turbulent premixed combustion modelling based on the C-equation (Eq. 2.15) yields a simplified relation of the local normalised

turbulent reaction rate to the local HRR density (Eq. 2.20) that provides the starting point of the locally resolved flame response model in Chapter 5.

## 3 Linearised Disturbance Equations

The solution of the general, non-linear form of the conservation equations requires cost-intensive numerical methods. However, the linear or weakly non-linear approximation of the governing equations can be solved by efficient analytical and numerical approaches, and therefore, the linearised conservation equations and relevant assumptions are provided in this section. The disturbance energy, the Rayleigh criterion, and the inhomogeneous wave equation are introduced. The chapter concludes with the analytical solution of HF acoustic modes in cylindrical can combustors.

### 3.1 Linearised Conservation Equations

Efficient thermoacoustic modelling employs the linearisation of the pressure, velocity and HRR density, since the direct solution of the non-linear conservation equations requires cost-intensive numerical methods. The linearisation of the variable  $\phi$  to first order  $\phi = \bar{\phi} + \phi'$  yields the time invariant mean  $\bar{\phi}$  and the fluctuation  $\phi'$ , which yields for the pressure, velocity and HRR density respectively:

$$p = \bar{p} + p', \quad (3.1)$$

$$\mathbf{u} = \bar{\mathbf{u}} + \mathbf{u}', \quad (3.2)$$

$$\dot{q} = \bar{\dot{q}} + \dot{q}'. \quad (3.3)$$

Suitable assumptions are inevitable for the numerical solution and especially for possible analytical solutions. First, the restriction to small, linear perturbations concerning the solution of the instantaneous acoustic pressure fields is common practice in linear stability analysis. Second, neglecting entropy fluctuations reduces the required set of differential equations to the momentum

and energy balance. The mass balance becomes redundant with the energy balance due to the isentropic relation of density and pressure  $p' = \rho' \bar{c}^2$ . Although combustion is associated with an increase in entropy, the assumption of isentropic propagation of the acoustic fluctuations is still valid. Third, the stochastic turbulent fluctuations cancel out for statistically stationary acoustic experimental data and are thus only concerned with the mean flow properties. Fourth, heat conduction, radiation and external volume forces are neglected. Thus, heat release due to the unburned, ideal gas mixture is considered as the dominant source in the energy conservation.

Linearisation of the conservation of the mass, momentum and energy considering a steady mean flow field yields

$$\bar{d}\rho' + u'_j \frac{\partial \bar{\rho}}{\partial x_j} + \rho' \frac{\partial \bar{u}_i}{\partial x_i} + \bar{\rho} \frac{\partial u'_i}{\partial x_i} = 0, \quad (3.4)$$

$$\bar{\rho} \left( \frac{\bar{d}u'_i}{dt} + u'_j \frac{\partial \bar{u}_i}{\partial x_j} \right) + \rho' \bar{u}_j \frac{\partial \bar{u}_i}{\partial x_j} + \frac{\partial p'}{\partial x_i} = \frac{\partial \tau'_{ij}}{\partial x_j}, \quad (3.5)$$

$$\frac{\bar{d}p'}{dt} + u'_j \frac{\partial \bar{p}}{\partial x_j} + \bar{\kappa} \left( \bar{p} \frac{\partial u'_j}{\partial x_j} + p' \frac{\partial \bar{u}_j}{\partial x_j} \right) = (\bar{\kappa} - 1) \dot{q}', \quad (3.6)$$

denoting the mean material derivative of the fluctuations  $\bar{d} = \frac{\partial}{\partial t} + \bar{u}_j \frac{\partial}{\partial x_j}$ . Considering a homogeneous mean flow, i.e. no gradients in density or velocity and neglecting viscous dissipation yields

$$\frac{\bar{d}\rho'}{dt} + \bar{\rho} \frac{\partial u'_i}{\partial x_i} = 0, \quad (3.7)$$

$$\bar{\rho} \frac{\bar{d}u'_i}{dt} + \frac{\partial p'}{\partial x_i} = 0, \quad (3.8)$$

$$\frac{\bar{d}p'}{dt} + \bar{\kappa} \bar{p} \frac{\partial u'_j}{\partial x_j} = (\bar{\kappa} - 1) \dot{q}'. \quad (3.9)$$

The linearised conservation equations account for acoustic and vortical disturbances and provide the governing equations for the linear acoustic network model in Chapter 6 and the linear hydrodynamic transport model in Section

5.3.1. Moreover, the linear combination of the momentum and energy conservation Eqs. 3.7 and 3.9 yields the inhomogeneous wave equation and the acoustic disturbance energy equation discussed in the following section.

## 3.2 Acoustic Disturbance Energy and Rayleigh Criterion

Coherent flame dynamics originating from the acoustic fluctuations in combustors are associated with a volumetric source in disturbance energy, which might generally originate from acoustic, turbulent or entropic disturbances [67–69]. The relation of the volumetric source to the flux in disturbance energy entering and leaving the combustor determines the thermoacoustic stability of the system.

In the present thesis, the disturbance energy conservation accounting solely for the isentropic acoustic disturbances is considered, neglecting any losses. The acoustic disturbance energy conservation is derived from the combination of the linearised momentum 3.8 and the linearised energy conservation 3.9 equations, which yields

$$\frac{\partial}{\partial t} \left( \frac{p'^2}{2\bar{\rho}\bar{c}^2} + \frac{\bar{\rho}}{2} u_j'^2 \right) + \frac{\partial p' u_j'}{\partial x_j} = \frac{\bar{\kappa} - 1}{\bar{\kappa}\bar{p}} p' \dot{q}', \quad (3.10)$$

for negligible mean flow effects in the low Mach number limit. Integration over the control volume  $V$  and employing the Gauss' integral theorem to obtain the acoustic power flux across the closed system surface  $A$  yields

$$\int_V \frac{\partial}{\partial t} \left( \frac{p'^2}{2\bar{\rho}\bar{c}^2} + \frac{\bar{\rho}}{2} u_j'^2 \right) dV + \oint p' u_j' n_j dA = \frac{\bar{\kappa} - 1}{\bar{\kappa}\bar{p}} \int_V p' \dot{q}' dV. \quad (3.11)$$

The first term on the left-hand side of Eq. 3.11 contains the integral unsteady change in acoustic energy

$$E_a = \int_V \frac{\partial}{\partial t} \left( \frac{p'^2}{2\bar{\rho}\bar{c}^2} + \frac{\bar{\rho}}{2} u_j'^2 \right) dV, \quad (3.12)$$

the second term describes the flux of the acoustic energy across the system boundaries

$$F_a = \oint_A p' u_j' n_j dA. \quad (3.13)$$

The term on the right-hand side of Eq. 3.10 is the integral source of acoustic energy

$$\dot{S}_a = \frac{\bar{\kappa} - 1}{\bar{\kappa} \bar{p}} \int_V p' \dot{q}' dV. \quad (3.14)$$

The local formulation provided by Eq. 3.10 reveals detailed insight regarding the local coupling of the isentropic acoustic pressure and unsteady heat release associated with the Rayleigh index  $ri = p' \dot{q}'$  [12]. The integral formulation according to Eq. 3.11 yields the global Rayleigh Integral  $\int \int p' \dot{q}' dV dt$  that reveals the resulting driving potential of a thermoacoustic instability. The thermoacoustic system becomes unstable if the integral source outperforms the acoustic power transmitted from the system boundaries [3].

The Rayleigh integral is used in the present thesis to estimate the driving potential of the experimental results in Chapter 8. Schuermans et al. [32] shows for the LF case that the Rayleigh Integral is expected to be always positive for statistically stationary data if the acoustic pressure is adequately measured, which has to be considered for the experimental results. Moreover, as a linear combination of the linearised momentum and energy balance, the disturbance energy conservation Eq. 3.10 provides the basis for the low order modelling approach accounting for the power transmitted at a sudden area change or a flame in Chapter 6.

The inhomogeneous wave equation discussed in the next section is an alternative linear combination of momentum and energy conservation.

### 3.3 Inhomogeneous Convective Wave Equation

The common derivation of the inhomogeneous convective wave equation according to the thermo- and aeroacoustic literature [70–72] contains the following steps. First of all, the momentum and energy conservation is linearised as shown in Section 3.1. Second of all, the conservation equations are combined by subtracting the gradient  $\frac{\partial}{\partial x_i}$  of the momentum conservation from the material derivative of the energy conservation  $\frac{d}{dt}$  combined with the speed of sound for an ideal gas  $\rho c^2 = \kappa p$ . The momentum and energy conservation ac-

ording to Eqs. 3.5 and 3.6 include gradients of the mean flow velocity that can be accounted for by the choice of proper boundary conditions as shown by Heilmann et al. [72]. However, the focus of the present thesis is on the inhomogeneous source term rather than the contribution of the mean flow and therefore a homogeneous mean flow field may be assumed. In the case that a homogeneous mean flow field is assumed, Eqs. 3.8 and 3.9 are used to obtain the inhomogeneous convective wave equation

$$\frac{\bar{d}^2 p'}{dt^2} - \bar{\rho} \bar{c}^2 \frac{\partial}{\partial x_i} \left( \frac{1}{\bar{\rho}} \frac{\partial p'}{\partial x_i} \right) = (\bar{\kappa} - 1) \frac{\bar{d} \dot{q}'}{dt}. \quad (3.15)$$

Here, the second derivative of the mean material derivative reads  $\frac{\bar{d}^2 p'}{dt^2} = \frac{\partial^2}{\partial t^2} + 2\bar{u}_j \frac{\partial}{\partial x_j} \frac{\partial}{\partial t} + \bar{u}_j^2 \frac{\partial^2}{\partial x_j^2}$ . The inhomogeneous convective wave equation is transformed to the frequency domain, which yields the inhomogeneous convective Helmholtz equation

$$\omega^2 \hat{p} - 2i\omega \bar{u}_j \frac{\partial \hat{p}}{\partial x_j} - \bar{u}_j^2 \frac{\partial^2 \hat{p}}{\partial x_j^2} + \bar{\rho} \bar{c}^2 \frac{\partial}{\partial x_i} \left( \frac{1}{\bar{\rho}} \frac{\partial \hat{p}}{\partial x_i} \right) = -(\bar{\kappa} - 1) \left( i\omega \hat{q} + \bar{u}_j \frac{\partial \hat{q}}{\partial x_j} \right), \quad (3.16)$$

see also Heilmann et al. [73]. Acoustic velocity boundary conditions might be applied by the acoustic flux term  $\frac{\partial}{\partial x_i} \left( \frac{1}{\bar{\rho}} \frac{\partial \hat{p}}{\partial x_i} \right)$  using the linearised momentum conservation at the boundaries (Eq. 3.5) accounting for mean flow effects, see [73]. In the low Mach number limit the velocity boundary conditions are applied via

$$\hat{u}_i = -\frac{1}{i\omega \bar{\rho}} \frac{\partial \hat{p}}{\partial x_i} \quad (3.17)$$

and the non-dimensional impedance boundaries accounting for the area normal acoustic velocity:

$$z = \frac{\hat{p}}{\bar{\rho} \bar{c} \hat{u}_i}. \quad (3.18)$$

The inhomogeneous wave equation contains the volumetric source term due to unsteady HRR associated with thermoacoustic instabilities and can only be solved by numerical methods for arbitrary geometries as discussed in Section 4.3. For technically relevant combustion chambers in gas turbines and rocket engines, analytical solutions of the wave equation can be deduced, as described in the next section.

### 3.4 Acoustic Wave Propagation in Tubes

The solution of the wave equation in cylindrical coordinates of the acoustic pressure  $p'$  is obtained by the general three-dimensional separation ansatz employing the Bessel function  $J_n$ , azimuthal counter- and clock-wise spinning waves and up- and downstream travelling f- and g-waves [74] as frequently used for combustor stability analysis (e.g. [3, 10, 75]). Employing the linearised momentum conservation for low Mach number flow (Eq. 3.17) results in the axial acoustic velocity field. The obtained mode shapes  $p' = \Re [\hat{p}e^{i\omega t}]$  and  $u' = \Re [\hat{u}e^{i\omega t}]$  generally depend on multiple complex amplitudes

$$\hat{p} = \hat{A}_r J_n(r) (\hat{f}_\theta e^{-im\theta} + \hat{g}_\theta e^{+im\theta}) (\hat{f}_x e^{-ik_+x} + \hat{g}_x e^{-ik_-x}), \quad (3.19)$$

$$\bar{\rho}\bar{c}\hat{u} = \hat{A}_r J_n(r) (\hat{f}_\theta e^{-im\theta} + \hat{g}_\theta e^{+im\theta}) (\hat{f}_x \kappa_+ e^{-ik_+x} + \hat{g}_x \kappa_- e^{-ik_-x}). \quad (3.20)$$

The azimuthal dependency of the acoustic cylinder mode

$$P_m(\theta) = e^{-im\theta} + R_\theta e^{+im\theta} \quad (3.21)$$

is used in the following derivations. Thus, the three-dimensional acoustic mode shapes of acoustic pressure and axial velocity in a can combustor reduce to

$$\hat{p} = J_n(r) P_m(\theta) (f(x) + g(x)), \quad (3.22)$$

$$\hat{u} = J_n(r) P_m(\theta) \left( \frac{\kappa_+}{\bar{\rho}\bar{c}} f(x) + \frac{\kappa_-}{\bar{\rho}\bar{c}} g(x) \right). \quad (3.23)$$

The axial dependencies on the f- and g-waves,  $f(x) = \hat{f}e^{-ik_+x}$  and  $g(x) = \hat{g}e^{-ik_-x}$ , respectively, consider the lumped amplitudes  $\hat{f} = \hat{A}_r \hat{f}_\theta \hat{f}_x$  and  $\hat{g} = \hat{A}_r \hat{g}_\theta \hat{g}_x$ . The Bessel function  $J_n(r)$  implies rigid wall boundary conditions at the combustor wall in the radial direction, otherwise, the Hankel function has to be considered [71, 74]. The azimuthal function  $P_m(\theta)$  depends on the constant azimuthal mode number  $m = 1, 2, \dots$  and the azimuthal reflection coefficient  $R_\theta = \frac{g_\theta}{f_\theta}$  equivalent to a spin ratio in azimuthal direction. Thus, boundary conditions in the azimuthal direction are applied by the azimuthal reflection coefficient, which includes standing ( $R_\theta = 1$ ), spinning ( $R_\theta = 0$ ) and mixed

( $0 < R_\theta < 1$ ) mode wave propagation in azimuthal direction. The axial wave numbers generally include mean flow effects

$$k_\pm = \frac{1}{1 - M^2} \left( -Mk \pm \sqrt{k^2 - k_{mn}^2 (1 - M^2)} \right), \quad (3.24)$$

which simplifies for a low Mach number  $M = \frac{\bar{u}}{c} \ll 0.2$  to  $k_\pm = \pm \sqrt{k^2 - k_{mn}^2}$ . Normalisation with the acoustic wave number  $k = \frac{2\pi f}{c}$  yields the non-dimensional axial wave numbers  $\kappa_\pm = \frac{k_\pm}{k}$ . The wave number  $k_{mn} = \frac{\alpha_{mn}}{r}$  depends on the radial position. The argument of the Bessel function  $J_n(\alpha_{mn})$  is obtained by the reflective boundary condition at the tube wall and depends on the radial and azimuthal mode number (e.g. T1 mode:  $\alpha_{mn} = 1.841$ ). The equations provided in this section include longitudinal and transverse mode wave propagation, since the LF case is obtained for  $\alpha_{mn} = 0$ .

The self-similarity of the cross-sectional dependency of acoustic pressure and axial velocity is used to define the four poles of the two-port transfer matrices by normalisation with the ansatz functions in cross-sectional direction. This yields the modal acoustic pressure  $\hat{p}_{mn}$  and the modal axial acoustic velocity  $\hat{u}_{mn}$  which read

$$\hat{p}_{mn}(x) = \frac{\hat{p}}{J_n(r)P_m(R_\theta, \theta)} = f(x) + g(x), \quad (3.25)$$

$$\hat{u}_{mn}(x) = \frac{\hat{u}}{J_n(r)P_m(R_\theta, \theta)} = \frac{\kappa_+}{\rho c} f(x) + \frac{\kappa_-}{\rho c} g(x). \quad (3.26)$$

The similarity of the modal acoustic pressure (Eq. 3.25) and the modal axial acoustic velocity (Eq. 3.26) is used in the following Chapter 6 to extend the two-port transfer matrix method to HF acoustics in cylindrical geometries. The distinction between the locally resolved acoustic pressure and axial acoustic velocity according to Eqs. 3.22 and 3.23, respectively, and the modal acoustic pressure and modal axial acoustic velocity (Eq. 3.25 and 3.26) is crucial for the derivation of the low order model in Chapter 6.

## 4 Experimental and Numerical Methods

The experimental and numerical methods applied in the present thesis work are provided in this section. First, the general procedure to obtain phase-averaged HRR images is described. Second, the Multi-Microphone-Method (MMM) in the azimuthal and axial direction and the reconstruction of axial transfer matrices is discussed. Third, the numerical CFD/CAA method based on the weak formulation of the Helmholtz equation is provided.

### 4.1 Phase-Locked OH\* images

The core of the phase-locking routine is similar to the one described by McClure et al. [36]. Phase-averaging eliminates stochastic turbulent fluctuations from the OH\* chemiluminescence signal [76]. The high-speed camera record signal triggers the measured acoustic pressure to obtain simultaneous acoustic and optical data for the phase-averaging routine. The shutter signal of the image intensifier is used to assign the instantaneous images to the respective time in the acoustic pressure time series. In order to obtain information on the driving potential of the HRR fluctuations, the global Rayleigh integral or the local Rayleigh index needs to be determined. Schuermans et al. [77] indicate that a proper choice of the reference sensor for phase-locking is crucial to obtain the correct phase relation of the HRR and the acoustic pressure fluctuations associated with the Rayleigh integral. Therefore, an acoustic pressure sensor  $C_1$  just downstream of the flames in the combustion chamber is used for the optical investigations and referred to as  $p'_{C_1}(t)$  in the following. Additional post-processing of the measured acoustic pressure time series  $p'_{C_1}(t)$  is necessary to access the phase  $\angle p'_{C_1}(t)$  at every instant  $t$ . The Hilbert Trans-

form [78] is applied to the time series

$$\hat{p}_{C1} = \mathcal{H} [p'_{C1}(t)] \quad (4.1)$$

to obtain the complex-valued acoustic pressure amplitude  $\hat{p}_{C1}$  and the phase  $\varphi(t)$  at every instant in time. Several hundred of instantaneous images are phase-locked to the chosen acoustic pressure reference time series and averaged in discretised phase bins. One oscillation period is separated into  $n_{\text{bin}} = 8$  discrete, equally spaced phase bins to phase-average the respective chemiluminescence images. The local line-of-sight integrated, phase-locked HRR density

$$\dot{q} = K \bar{I}_{\text{OH}^*} \quad (4.2)$$

is estimated by the scaling-factor

$$K = \frac{P_{\text{th}}}{\int \bar{I}_{\text{OH}^*} dV}, \quad (4.3)$$

which relates the phase-locked OH\* intensity  $\bar{I}_{\text{OH}^*}$  to the global thermal power  $P_{\text{th}}$ . The difference between the phase-averaged HRR density and the temporal mean value yields the fluctuations

$$\dot{q}' = \dot{q} - \bar{\dot{q}} \quad (4.4)$$

and the normalisation with the mean value yields the normalised HRR fluctuations

$$\frac{\dot{q}'}{\bar{\dot{q}}} = \frac{\dot{q}}{\bar{\dot{q}}} - 1. \quad (4.5)$$

An OH\* intensity brightness cutoff of 2% is used to avoid an artificial increase of the normalised HRR density fluctuations  $\dot{q}'/\bar{\dot{q}}$  due to low OH\* intensity background signals.

Several parameters must be defined for the optical measurements. The resolution of  $1024 \times 1024$  pixel of the instantaneous images and the sample rate of 10000 Hz determine the maximum number of images stored on the internal storage of the high-speed camera, which yields an amount of  $n \approx 5000$  images. The shutter time must be sufficiently large to obtain a clear OH\* intensity. However, a sufficiently small shutter time is required to assign the instantaneous images to the respective phase in the time series correctly. This work identifies an image intensifier shutter time of  $80 - 40 \mu\text{s}$  as suitable.

## 4.2 Multi-Microphone-Method

The multi-microphone method is an established method to reconstruct acoustic fields in straight ducts [47]. In the HF case, the axial and azimuthal direction needs to be considered to capture the azimuthal mode shape, including standing, spinning or flipping transverse modes as demonstrated by Kim et al. [75, 79]. The multi-microphone method is used to ensure a standing mode shape of the forced response T1 mode in the optical and acoustical experiments and to reconstruct the acoustic velocity fluctuations at the injector tube exit.

### 4.2.1 Azimuthal Acoustic Pressure Field

The mode shape reconstruction in the azimuthal direction reveals insights into the spinning or standing behaviour of transverse acoustic modes. In order to resolve the temporal evolution of the spinning or standing transverse mode, the MMM might be applied to the azimuthal and temporal resolved pressure signals according to Kim et al. [75, 79]. The azimuthal dependency of the acoustic pressure field

$$\hat{p}_\theta(\theta)e^{i\omega t} = \underbrace{[\hat{f}_\theta e^{im\theta}]}_{f_\theta} + \underbrace{[\hat{g}_\theta e^{-im\theta}]}_{g_\theta} e^{i\omega t} \quad (4.6)$$

is decomposed into the wave travelling in positive  $f_\theta$  and negative  $g_\theta$  azimuthal direction for the entire time signal. In order to calculate the spin ratio, Eq. 4.6 is recast in matrix form

$$\underbrace{\begin{bmatrix} \hat{p}_\theta(\theta_1)e^{i\omega t} \\ \vdots \\ \hat{p}_\theta(\theta_n)e^{i\omega t} \end{bmatrix}}_{\mathbf{P}_\theta} = \underbrace{\begin{bmatrix} e^{im\theta_1} & e^{-im\theta_1} \\ \vdots & \vdots \\ e^{im\theta_n} & e^{-im\theta_n} \end{bmatrix}}_{\mathbf{M}_\theta} \times \underbrace{\begin{bmatrix} \hat{f}_\theta e^{i\omega t} \\ \hat{g}_\theta e^{i\omega t} \end{bmatrix}}_{\mathbf{X}_\theta}. \quad (4.7)$$

Here  $\theta_1$  to  $\theta_n$  describes the azimuthal position of the  $n$  sensors. The least-square fit reveals

$$\mathbf{X}_\theta = (\mathbf{M}_\theta^T \mathbf{M}_\theta)^{-1} \mathbf{M}_\theta^T \mathbf{P}_\theta, \quad (4.8)$$

where the vector  $\mathbf{M}_\theta^T$  means the transposed vector of  $\mathbf{M}_\theta$ . The time evolution of the nodal line is evaluated

$$\theta_m(t) = \frac{j \cdot \pi - (\angle(\hat{f}_\theta e^{i\omega t}) - \angle(\hat{g}_\theta e^{i\omega t}))}{2m}, j = 1, 3, 5... \quad (4.9)$$

which gives insight into the pressure field inside the combustion chamber. The amplitudes  $\hat{f}_\theta$  and  $\hat{g}_\theta$  determine the Spin Ratio (SR)

$$SR = \frac{|\hat{f}_\theta| - |\hat{g}_\theta|}{|\hat{f}_\theta| + |\hat{g}_\theta|}. \quad (4.10)$$

A perfectly standing mode corresponds to a Spin Ratio of  $SR = 0$ . On the contrary, a spin ratio of  $SR = \pm 1$  yields a perfectly spinning mode in a positive or negative azimuthal direction. Mixed standing and spinning modes are identified by values of  $0 < |SR| < 1$ , which account for mixed modes [75]. The spin ratio and the nodal line position are used to characterise the standing mode type of the investigated forced response experiments.

### 4.2.2 Axial Acoustic Pressure Field

The application of the MMM to at least two acoustic pressure sensors with varying axial position and constant radial and azimuthal position yields the axial acoustic pressure field

$$\hat{p}_{mn}(x) = \hat{f}_x e^{-ik_+x} + \hat{g}_x e^{-ik_-x}. \quad (4.11)$$

The matrix representation of the acoustic pressure field for the different sensor positions

$$\underbrace{\begin{bmatrix} \hat{p}_{mn}(x_1) \\ \vdots \\ \hat{p}_{mn}(x_n) \end{bmatrix}}_{\mathbf{P}_x} = \underbrace{\begin{bmatrix} e^{-ik_+x_1} & e^{-ik_-x_1} \\ \vdots & \vdots \\ e^{-ik_+x_n} & e^{-ik_-x_n} \end{bmatrix}}_{\mathbf{M}_x} \times \underbrace{\begin{bmatrix} \hat{f}_x \\ \hat{g}_x \end{bmatrix}}_{\mathbf{X}} \quad (4.12)$$

is solved for the unknown vector  $\mathbf{X}$  of the f- and g-wave amplitudes

$$\mathbf{X} = (\mathbf{M}_x^T \mathbf{M}_x)^{-1} \mathbf{M}_x^T \mathbf{P}_x. \quad (4.13)$$

The acoustic pressure and the axial acoustic velocity are calculated according to Eqs. 3.25 and 3.26, respectively.

### 4.2.3 Axial Transfer Matrix Reconstruction

The reconstruction of the HF transfer matrices is required to validate the analytical transfer matrices of the low order network model. Reconstructed transfer matrices from CFD or experiments might also be used to model the flame dynamics. Experimentally measured HF transfer matrices can be reconstructed using the two-port network modelling approach once the acoustic field is determined from the MMM.

The effective acoustic pressure Eq. 3.25 and axial acoustic velocity Eq. 3.26 normalised with the radial and azimuthal dependency are used to obtain a quasi-two-port transfer matrix reconstruction for HF acoustics. The SR or azimuthal reflection coefficient  $R_\theta$  needs to be determined for the normalisation in Eqs. 3.26 and 3.25 from the MMM in azimuthal direction. The two-source location method [47] with Upstream Forcing (UF) and Downstream Forcing (DF)

$$\underbrace{\begin{pmatrix} \hat{p}_{mn,UF} & \hat{p}_{mn,DF} \\ \hat{u}_{mn,UF} & \hat{u}_{mn,DF} \end{pmatrix}_{do}}_{=Y_{do}} = \text{TM}_{pu} \cdot \underbrace{\begin{pmatrix} \hat{p}_{mn,UF} & \hat{p}_{mn,DF} \\ \hat{u}_{mn,UF} & \hat{u}_{mn,DF} \end{pmatrix}_{up}}_{=X_{up}} \quad (4.14)$$

yields the transfer matrix in  $p, u$ -notation

$$\text{TM}_{pu} = X_{up}^{-1} Y_{do} \quad (4.15)$$

from the effective acoustic pressure and axial velocity up- and downstream of the transfer element obtained with the MMM.

## 4.3 Hybrid CFD/CAA Method

The inhomogeneous wave equation might be solved by the separation of the mean flow field and the acoustic domain according to the CFD/CAA approach. COMSOL Multiphysics is used to calculate the solution of the Helmholtz Equation employing the Galerkin-FEM methodology, which solves

the weak formulation of a Partial Differential Equation (PDE). The weak formulation of a PDE requires less computational cost. However, the weak formulation of the boundary conditions and the weak formulation of the differential equation have to be derived.

First, the weak-form-PDE is obtained by multiplication of the PDE with a test function denoted with  $\tilde{()}$  for discretisation. Second, the differential equation is partially integrated to obtain the weak formulation. Third, the boundary flux terms are expressed using Gauss' theorem. Considering the inhomogeneous Helmholtz equation 3.16 in the low Mach number limit, the weak formulation reads

$$\int \omega^2 \hat{p} \tilde{p} - \bar{c}^2 (\nabla \hat{p}) \cdot \nabla \tilde{p} dV + \int \bar{c}^2 (\nabla \hat{p}) \tilde{p} \tilde{n} dA = i\omega \int_V (\bar{\kappa} - 1) \hat{q} \tilde{p} dV. \quad (4.16)$$

For a more detailed derivation accounting also for convective effects, see Heilmann et al. [73]. Impedance boundary conditions are implemented according to Eq. 3.18 in the flux term

$$\int \bar{c}^2 (\nabla \hat{p}) \tilde{p} \tilde{n} dA = \int i\omega \bar{c} \frac{\hat{p}}{z} \tilde{p} \tilde{n} dA \quad (4.17)$$

to express the acoustic velocity via the acoustic pressure, using the Euler equation in the low Mach number limit.

The inhomogeneous source term of the Helmholtz equation requires additional closure models to couple the local unsteady HRR to the acoustic velocity and pressure. The instantaneous coupling to the acoustic pressure and acoustic velocity is considered in the flame compression and displacement model in the HF regime [20–23]. The convectively transported reaction rate perturbations due to large scale coherent turbulent structures might be accounted for by an additional transport equation for the progress variable, which diminishes the advantage of solving one single acoustic equation. An efficient approach is to account for the convective flame response mechanism by the Flame Transfer Function (FTF) coupling the acoustic velocity fluctuations at a reference position to the integral HRR fluctuations  $FTF = \frac{\hat{Q}_{conv}/\bar{Q}}{\hat{u}_{ref}/\bar{u}_{ref}}$ , according to the  $n$ - $\tau$ - $\sigma$  modelling approach in the LF regime [31,32]. The acoustic velocity fluctuations at the reference position  $\hat{u}_{ref}$  are constant in cross-

sectional direction due to the longitudinal wave propagation. The spatial distribution of the time delays is obtained from the CFD mean field. The application of the global FTF to the CFD/CAA method assumes a constant gain and phase of the unsteady HRR fluctuations over the extent of the flame, which is a reasonable assumption in the LF limit [43–46].

The assumption of both spatially invariant gain and phase of the flame response is violated for HF thermoacoustics. Thus, instead of the global FTF, the locally resolved Flame Transfer Function (ftf) has to be considered

$$\hat{q}_{\text{conv}}(\mathbf{x}) = \frac{\bar{q}}{\bar{u}_{\text{ref}}} \hat{u}_{\text{ref}} \text{ftf}(\mathbf{x}), \quad (4.18)$$

to obtain the local flame response. The local flame response according to Eq. 4.18 might generally include a three-dimensional resolved gain and phase of the ftf. Moreover, the acoustic velocity varies in cross-sectional direction in the HF case and locally due to the longitudinal to transverse/radial coupling at the injector tube exit, which is covered by the acoustic solver. A hydrodynamic transport model is required to couple the convective flame response to the acoustic velocity fluctuations at the reference position, i.e. the injector tube exit, to obtain the generalised, locally resolved flame response. Thus, in similarity to the  $n$ - $\tau$  approach the locally resolved flame response might be obtained by the local time delay  $\tau(\mathbf{x})$  and the local gain  $n(\mathbf{x})$  to obtain the closure model  $\text{ftf} = n(\mathbf{x})e^{i\tau(\mathbf{x})}$ . In first proximity, a straight flow path from the reference position to the flame is assumed for the considered MJC configuration, which implies that  $\tau$  is solely dependent on the axial coordinate, as used for the numerical solution of the flame response in Section 9.2. Thus, the convective transport in main flow direction is assumed. Both the distribution of the local gain and phase and turbulent dissipation become important for the HF case due to the decreasing gain of the convective flame response. Therefore, a distributed convective flame response model is deduced in the following section, accounting for a local gain and phase and turbulent dissipation along the flow path from the injector section exit to the end of the flame.

## 5 Distributed Flame Response Model

The scope of this section is to discuss the dominant acoustic and convective sources in unsteady heat release and the main assumptions of the convective flame response model, i.e. perfectly premixed conditions and the transport of coherent vortices in main flow direction.

The inhomogeneous convective acoustic wave equation 3.15 includes the acoustic source term due to unsteady heat release, which is linearised considering solely acoustic perturbations:

$$\frac{\bar{d}\dot{q}'}{dt} = \frac{\partial \dot{q}'}{\partial t} + \bar{u}_j \frac{\partial \dot{q}'}{\partial x_j}. \quad (5.1)$$

Consistent with the low Mach number assumption, the convective transport of the HRR fluctuations  $\bar{u}_j \frac{\partial \dot{q}'}{\partial x_j}$  in Eq. 5.1 is omitted in the following. In this section, closure models are derived for the remaining local sources  $\frac{\partial \dot{q}'}{\partial t}$  of the mean HRR. First, the local flame displacement and flame compression mechanisms are discussed. Second, a distributed convective flame response model is deduced based on hydrodynamic stability analysis.

### 5.1 Linearised Heat Release Density

The local volumetric source term in HRR density is obtained from the linearised heat release closure

$$\dot{q}' = \rho' \bar{\dot{\Omega}}_t \bar{Y}_F \bar{H}_u + \bar{\rho} \dot{\Omega}'_t \bar{Y}_F \bar{H}_u + \dots \quad (5.2)$$

according to Eq. 5.2 dependent on the local density, the normalised consumption rate, the fuel mass fraction and the lower caloric heating value. For perfectly premixed conditions local density and consumption rate fluctuations

are the predominant sources. The density fluctuations obtained from the ideal gas law  $\frac{\rho'}{\bar{\rho}} = \frac{p'}{\bar{p}} - \frac{T'}{\bar{T}}$  generally include a non-homentropic contribution  $T'$  accounting for entropy waves convected downstream and generating acoustic waves at the combustor exit nozzle [31, 80]. However, entropy waves in the burned gas are non-existent for perfectly premixed combustion. Furthermore, the local sources  $\frac{\partial \dot{q}'}{\partial t}$  in Eq. 5.1 might generally include local consumption rate fluctuations originating from baroclinic torque due to the 90 degree orientation in space of the acoustic pressure and the mean density gradient. However, the effect is merely negligible for low amplitudes [81]. Nevertheless, the baroclinic effect can have a noticeable impact for higher amplitudes and lead to an amplitude-dependent dissipation, as shown by Hofmeister et al. [60].

The acoustic flame response due to the local acoustic pressure and velocity fluctuations and the convective flame response mechanisms are discussed in the following two sections.

## 5.2 Acoustic Flame Response

The acoustic flame response might be attributed to both the acoustic flame compression and the acoustic flame displacement, since both depend on the local, instantaneous acoustic field variables [22, 23, 72].

The linearised inhomogeneous convective wave equation provided by Eq. 3.15 is derived from the linear combination of the linearised momentum and energy conservation, as predominantly found in aero- and thermoacoustic literature [6, 73, 82]. Similarly, the gradient of the non-linear momentum conservation (Eq. 2.2) and the material derivative of the non-linear energy conservation (Eq. 2.6) might be combined according to Poinsot et al. [4] to obtain a non-linear inhomogeneous wave equation

$$\frac{d^2 p}{dt^2} - \rho c^2 \frac{\partial}{\partial x_i} \left( \frac{1}{\rho} \frac{\partial p}{\partial x_i} \right) = (\kappa - 1) \frac{d\dot{q}}{dt}. \quad (5.3)$$

The subsequent linearisation with respect to acoustic disturbances of Eq. 5.3

for a homogeneous mean flow field, neglecting second order terms yields

$$\frac{\bar{d}^2 p'}{dt^2} - \bar{\rho} \bar{c}^2 \frac{\partial}{\partial x_i} \left( \frac{1}{\bar{\rho}} \frac{\partial p'}{\partial x_i} \right) = (\bar{\kappa} - 1) \left( \frac{\bar{d} \dot{q}'}{dt} + u'_j \frac{\partial \bar{q}}{\partial x_j} \right). \quad (5.4)$$

Mind that the linearisation of the material derivative in Eq. 5.4 inherently includes the acoustic displacement term  $\dot{q}'_{\text{disp}} = u'_j \frac{\partial \bar{q}}{\partial x_j}$ . The source terms in the inhomogeneous wave equation according to Eq. 5.4 inherently includes the flame displacement mechanism, which is not the case if the source term according to Eq. 5.1 is considered. The flame displacement source term in the frequency domain reads

$$\hat{q}'_{\text{disp}} = -\frac{\hat{u}_j}{i\omega} \frac{\partial \bar{q}}{\partial x_j}, \quad (5.5)$$

which accounts for the displacement of the flame due to the local acoustic velocity field [22, 23]. The acoustic flame displacement accounts solely for the acoustic velocity fluctuations interacting with the flame. Thus, with restriction to acoustic velocity fluctuations in the low Mach limit, the linearised momentum conservation Eq. 3.17 couples the flame displacement model to the acoustic pressure  $\hat{u}_j = -\frac{1}{i\omega \bar{\rho}} \frac{\partial \hat{p}}{\partial x_j}$ .

The density fluctuations according to Eq. 5.2 contribute to the local HRR fluctuations, i.e. the first term on the left-hand side of Eq. 5.1. The isentropic relation of acoustic pressure and density fluctuations  $\hat{p} = \frac{\hat{\rho}}{\bar{\rho}}$  yields for the normalised density fluctuations  $\frac{\hat{\rho}}{\bar{\rho}} = \frac{\hat{p}}{\bar{\rho} \bar{c}^2}$ . The mean speed of sound expressed by the mean density and pressure using the ideal gas law  $\bar{\rho} \bar{c}^2 = \bar{\kappa} \bar{p}$  yields the normalised, isentropic density fluctuations

$$\frac{\hat{\rho}}{\bar{\rho}} = \frac{\hat{p}}{\bar{\kappa} \bar{p}}. \quad (5.6)$$

Finally, combining Eq. 5.6 and Eq. 5.2 the flame compression mechanism is obtained

$$\hat{q}'_{\text{comp}} = \frac{\hat{p}}{\bar{\kappa} \bar{p}} \bar{q}, \quad (5.7)$$

which directly couples to the local acoustic pressure mode shape to the HRR density fluctuations.

The acoustic flame displacement and compression mechanisms are established flame response models depending on the local acoustic and mean heat release rate field [22, 23]. The convective driving mechanism, however, requires an additional transport model to couple the local acoustic pressure and velocity to the convective source, as discussed in the following section.

### 5.3 Convective Flame Response

Figure 5.1 illustrates the considered generic setup of a perfectly premixed jet flame. Full conversion rate from unburned  $C_{r,u} = 0$  to burned gas conditions  $C_{r,b} = 1$  from upstream of the injector tube to downstream of the combustion chamber is considered. The dump plane, i.e. the injector tube exit, is referred to as the reference position in the following, see Fig. 5.1. Neglecting the effects of molecular diffusion and curvature on the flame speed, the local normalised turbulent reaction rate  $\bar{\Omega}_t$  (Eq. 2.19) yields the source term of the steady-state C-equation 2.15 expressed by the turbulent flame speed and the mean flame surface density

$$\bar{\Omega}_t = \bar{u}_j \frac{\partial \bar{C}_r}{\partial x_j} = \bar{s}_t \bar{\sigma}_{\text{Fl}}. \quad (5.8)$$

In the perfectly premixed case, the quasi-steady flame front stabilises due to the kinematic balance of the turbulent flame speed  $s_t$  and the flame normal velocity of unburned gas  $u_n = u_j n_{\text{Fl},j}$ . The flame front normal velocity is expressed with the flame front normal vector according to Eq. 2.17 as illustrated in Fig. 5.1. In case of thermoacoustic instability, the local kinematic balance of unburned gas velocity and turbulent flame speed is disturbed by acoustic velocity fluctuations at the reference position. The resulting flame dynamics are expressed via the linearised C-equation

$$\hat{\Omega}_t = i\omega \hat{C}_r + \bar{u}_j \frac{\partial \hat{C}_r}{\partial x_j} + \hat{u}_j \frac{\partial \bar{C}_r}{\partial x_j} = \hat{s}_t \bar{\sigma}_{\text{Fl}} + \bar{s}_t \hat{\sigma}_{\text{Fl}}. \quad (5.9)$$

The linearised C-equation according to Eq. 5.9 includes the unsteady change of the progress variable, its convective transport and an additional sink or source due to mean progress variable gradients and local coherent velocity

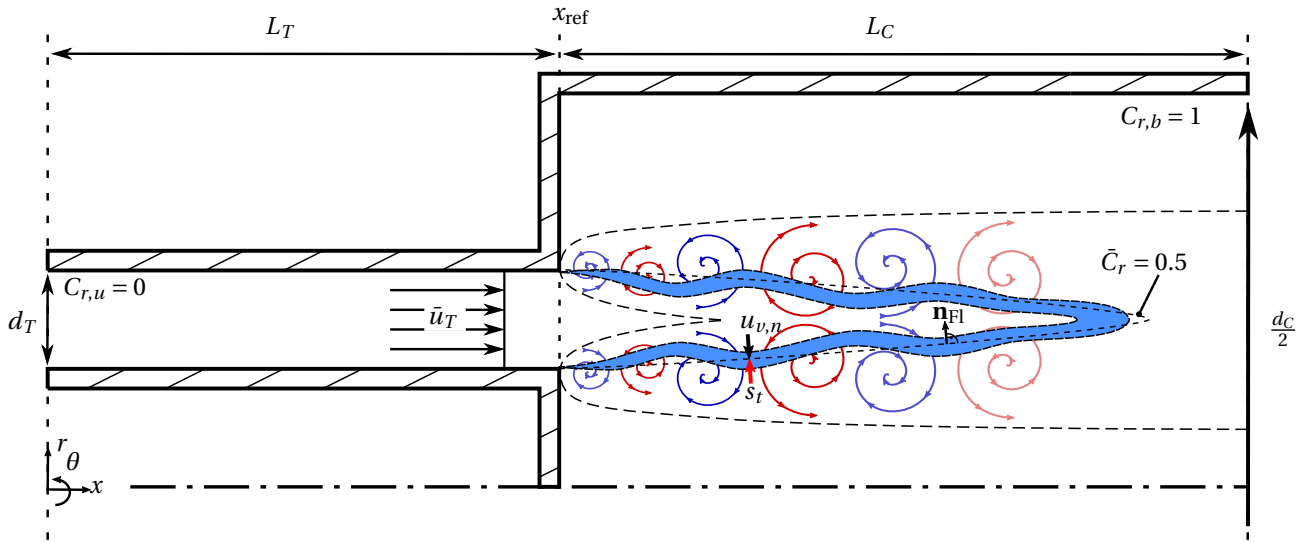


**Figure 5.1:** Sketch of an axial cut through a cylindrical MJC with combustion chamber diameter  $d_C$  at the centre of a single injector tube with diameter  $d_T$  and a jet flame represented by the reaction progress variable iso-contour  $C_r = 0.5$  with deflagrative flame stabilisation at the kinematic balance of the turbulent flame speed  $s_t$  and the flame normal velocity of unburned gas  $u_n$  close to the core region of the turbulent jet.

fluctuations. The equivalent split of the reaction rate fluctuations into flame speed and flame area perturbations is provided on the right-hand side, as often proposed in literature. The solution of the linearised C-equation generally requires numerical methods [28, 30, 83] including a local mean field and accounting for a closure model for flame area  $\hat{\sigma}_{\text{Fl}}$  and flame speed  $\hat{s}_t$  perturbation as considered by Hofmeister [60] or Romero Vega [84]. The scope of this section, however, is to deduce a simplified analytical, low order model of the convective flame response to reveal the main physics of the flame response.

Thus, additional assumptions are required to simplify Eq. 5.9, as discussed in the following. Generally, the convective flame response might originate from acoustic velocity fluctuations  $\hat{u}_{a,j}$  and coherent vortical velocity fluctuations  $\hat{u}_{v,j}$  as introduced in Chapter 3. The purely acoustic velocity fluctuations at the flame base generate unsteady flame front modulations that are convected downstream, which may contribute to the convective flame re-

sponse, besides coherent vortical fluctuations. The entire flame front is distorted due to the acoustic velocity fluctuation  $\hat{u}_{a,j}$  at low Strouhal-numbers  $St = \frac{f d_T}{\bar{u}_T} \ll 1$  as accounted by kinematic flame response models in the low frequency limit [28, 85]. However, coherent vortical velocity fluctuations  $\hat{u}_{v,j}$  dominate the entire convective flame response especially for fully turbulent flows and high Strouhal numbers as also shown for a self-sustained instability of a single jet flame by Buschhagen et al. [33]. Thus, solely the coherent vortical disturbances due to the acoustically triggered Kelvin Helmholtz instability in the hydrodynamic shear layer of the jet flames, as depicted in Fig. 5.1, is considered in the present thesis. Therefore, the coherent velocity fluctuations  $\hat{u}_j$  in Eq. 5.9 are replaced by the coherent vortical velocity fluctuations  $\hat{u}_{v,j}$  in the following. The gradients in progress variable in Eq. 5.9 are expressed via the flame surface density (Eq. 2.16) and the flame front normal vector (Eq. 2.17) for both fluctuating  $\hat{n}_{\text{Fl},j} = -\frac{\partial \hat{C}_r}{\partial x_j} / \sqrt{\left(\frac{\partial \hat{C}_r}{\partial x_j}\right)^2}$  and mean  $\bar{n}_{\text{Fl},j} = -\frac{\partial \bar{C}_r}{\partial x_j} / \sqrt{\left(\frac{\partial \bar{C}_r}{\partial x_j}\right)^2}$  contribution. Thus, the normalised turbulent reaction rate fluctuations

$$\hat{\Omega}_t = i\omega \hat{C}_r - \bar{u}_j \hat{n}_{\text{Fl},j} \bar{\sigma}_{\text{Fl}} - \hat{u}_{v,j} \bar{n}_{\text{Fl},j} \bar{\sigma}_{\text{Fl}} \quad (5.10)$$

are obtained. Consistent with the  $n$ - $\tau$  modelling approach [6, 25, 32], the first and second term on the right-hand side may be neglected. Based on the analytical approach of Hirsch et al. [62] a similar quasi-steady flame response model is suggested by Hofmeister [60], accounting solely for the last term on the right-hand side of Eq. 5.10. The first term on the right-hand side of Eq. 5.10 corresponds to the local unsteady change in the reaction progress. Neglecting of the first term yields a quasi-steady flame response model. The coherent velocity fluctuations include, however, a time delay due to the hydrodynamic transport from the reference position to the flame, as discussed in Section 5.3.1. The second term on the right-hand side of Eq. 5.10 covers the change in the local flame front normal vector due to the coherent velocity perturbations. The fluctuations in the flame front normal vector may be neglected considering small, linear perturbations. The flame front normal velocity fluctuations  $\hat{u}_{v,n} = -\hat{u}_{v,j} \bar{n}_{\text{Fl},j}$  yield

$$\hat{\Omega}_t = \hat{u}_{v,n} \bar{\sigma}_{\text{Fl}}. \quad (5.11)$$

Thus, the local flame front normal velocity fluctuations due to the coherent vortices determine the quasi-steady flame response by means of the reaction

rate fluctuations according to Eq. 5.11. The reaction rate fluctuations at the flame front (Eq. 5.11) are consistent with the commonly used  $n$ - $\tau$  models that might be applied to the numerical CFD/CAA method [43–46].

The coherent vortical fluctuations propagate with the mean flow and require an additional transport model. The hydrodynamic transport model is required to couple the local HRR fluctuations, i.e. the local coherent vorticity (Eq. 5.11), to the acoustic velocity fluctuations at the reference position, as discussed in the next section.

### 5.3.1 Linear Hydrodynamic Stability Analysis

Concerning the flame response to LF acoustic modes, the  $n$ - $\tau$  approach yields reasonable results, particularly for the phase between HRR fluctuations and the acoustic pressure and thus the flame driving. In the HF case, however, both the gain and phase vary significantly due to the convective non-compactness of the flame and the classical  $n$ - $\tau$  approach fails. A distributed response model is required to resolve the local coherent vortices and the associated vortical velocity fluctuations normal to the flame surface  $\hat{u}_{v,n}$  covering the hydrodynamic shear layer instability. The quasi-steady model, according to Eq. 5.10, is considered by Hofmeister [60]. The numerical solution of the linearised Navier-Stokes equations provides the transport of the coherent vortical velocity fluctuations, which comes at a high computational cost. Therefore, the objective of the next section is to obtain an efficient analytical approach for the transport model similar to Hirsch et al. [62].

The linearised momentum conservation Eq. 3.5 covers the material transport of coherent velocity fluctuations. Therefore, the linear stability analysis of the momentum conservation employing a normal mode ansatz for the preferred hydrodynamic mode provides a low order approach for the generation and the convective transport of the coherent velocity fluctuations. The axial gradient in fluctuating pressure is negligible in comparison to the convective transport of the coherent velocity fluctuations in unburned gas mixture  $\frac{1}{\rho} \frac{\partial \hat{p}}{\partial x} \ll \bar{u} \frac{\partial \hat{u}_{v,n}}{\partial x_j}$  in accordance to turbulent jet theory [86]. The convective transport of the flame response is usually dominated by one main flow direction.

For the case of MJC's, the convective transport is dominated by the axial direction  $\frac{u_x}{|\mathbf{u}|} \gg \frac{u_y}{|\mathbf{u}|}, \frac{u_z}{|\mathbf{u}|}$ , see Fig. 5.1. Therefore, a quasi-one-dimensional transport model in axial, main flow direction is deduced in the following. In order to increase the complexity step-wise, three analytical convective transport models are discussed in the following.

**First**, the linearised momentum conservation Eq. 3.17 reduces to the convective transport equation for  $\hat{u}_{v,n}$  concerning negligible viscous dissipation, negligible mean velocity and fluctuating pressure gradients:

$$i\omega \hat{u}_{v,n} + \bar{u} \frac{\partial \hat{u}_{v,n}}{\partial x} = 0. \quad (5.12)$$

The solution to Eq. 5.12 reads

$$\frac{\hat{u}_{v,n}(x)}{\hat{u}_{v,n}(x_{\text{ref}})} = e^{-ik_{\text{conv}}(x-x_{\text{ref}})} \quad (5.13)$$

with the constant axial convective wave number  $k_{\text{conv}} = \frac{\omega}{\bar{u}}$ . Equation 5.13 is an equivalent spatial expression of the  $n$ - $\tau$  model. Distributed response models assume a spatially constant amplitude of the velocity fluctuations over the extent of the flame, which might be justified in the LF regime. However, concerning the HF convective flame response, a spatially resolved amplitude of the fluctuations becomes important due to the non-compactness of the flame.

**Second**, the effect of dissipation might become increasingly important in the HF regime for increasing distance from the reference position and high turbulence levels. The linearised momentum conservation 3.8 is employed accounting for the diffusive term  $\bar{\nu} \frac{\partial^2 \hat{u}_{v,n}}{\partial x_j^2}$  with the diffusion coefficient  $\nu = \nu_t + \nu_m$  given by the turbulent and molecular diffusivity  $\nu_t, \nu_m$ , respectively. An analytical solution can be derived if the diffusive contribution is assumed to originate from the gradients in axial direction  $\frac{\partial^2 \hat{u}_{v,n}}{\partial x^2} \gg \frac{\partial^2 \hat{u}_{v,n}}{\partial y^2}, \frac{\partial^2 \hat{u}_{v,n}}{\partial z^2}$ , which yields

$$i\omega \hat{u}_{v,n} + \bar{u} \frac{\partial \hat{u}_{v,n}}{\partial x} = \bar{\nu} \frac{\partial^2 \hat{u}_{v,n}}{\partial x^2}. \quad (5.14)$$

Solving the second order Ordinary Differential Equation (ODE) Eq. 5.14 leads to a quadratic characteristic polynomial and thus the sum of two eigenfunctions with two constants  $c_{\pm}$ . The constants are determined from the boundary

condition at the reference position  $\hat{u}_{v,n} = \hat{u}_{v,n}(x_{\text{ref}})$  and at quasi-infinite distance  $L_\infty$  downstream of the flame  $\left. \frac{\partial \hat{u}_{v,n}}{\partial x} \right|_{L_\infty} = 0$ . The proportionality constants rapidly tend to their limits  $\lim_{x_\infty \rightarrow \infty} c_+ = 0$  and  $\lim_{x_\infty \rightarrow \infty} c_- = 1$ . Therefore, the solution of Eq. 5.14 simplifies to

$$\frac{\hat{u}_{v,n}(x)}{\hat{u}_{v,n}(x_{\text{ref}})} = e^{-ik_{\text{diff}}(x-x_{\text{ref}})} \quad (5.15)$$

$$k_{\text{diff}} = \frac{i\bar{u}}{2\bar{v}} \left( 1 - \sqrt{1 + i\omega \frac{4\bar{v}}{\bar{u}^2}} \right), \quad (5.16)$$

where the axial convective-diffusive wave number  $k_{\text{diff}}$  is introduced. The turbulent viscosity yields dissipation of the coherent structures due to stochastic turbulence and, thus, a decrease in coherent velocity fluctuations in the axial direction. Turbulent jet theory might be employed to obtain a first principle estimate of the axial increase in turbulent viscosity of the shear layer.

**Third**, gradients in the mean flow velocity according to Eq. 3.5 might amplify the coherent velocity fluctuations due to turbulence production. The momentum conservation accounting for velocity gradients yields

$$\hat{u}_{v,n} \left( i\omega + \frac{\partial \bar{u}}{\partial x} + \frac{\partial \bar{u}}{\partial r} \right) + \bar{u} \frac{\partial \hat{u}_{v,n}}{\partial x} = \bar{v} \frac{\partial^2 \hat{u}_{v,n}}{\partial x^2}. \quad (5.17)$$

The solution of the ODE given by Eq. 5.17 is obtained similar to the solution of Eq. 5.14 and reads

$$\frac{\hat{u}_{v,n}(x)}{\hat{u}_{v,n}(x_{\text{ref}})} = e^{-ik_{\text{shear}}(x-x_{\text{ref}})} \quad (5.18)$$

$$k_{\text{shear}} = \frac{i\bar{u}}{2\bar{v}} \left( 1 - \sqrt{1 + \left( i\omega + \frac{\partial \bar{u}}{\partial x} + \frac{\partial \bar{u}}{\partial r} \right) \frac{4\bar{v}}{\bar{u}^2}} \right), \quad (5.19)$$

Note that negative gradients yield an amplification of the velocity fluctuations according to Eq. 5.19, which might be significant at small axial distance from the reference position close to the injector tube exit, see Fig. 5.1. In particular, strong radial velocity gradients due to the high axial bulk velocity and the low axial velocity of the surrounding exhaust gas are expected. The radial gradients yield an amplification of the initial flow disturbance at the reference

position since the radial gradients are negative due to the decrease of the flow velocity in the radial direction. Thus, the initial coherent vortex formation due to the acoustic velocity fluctuations at the reference position amplified by the velocity gradients in the radial direction is covered by Eq. 5.19. However, detailed information on the mean flow gradients are required to quantitatively estimate the velocity fluctuations, which might be obtained from a CFD simulation or an empirical fit to experimental data.

The convective transport models of the coherent vortical velocity fluctuations according to Eqs. 5.13, 5.15 and 5.18 require an acoustic - turbulence - closure model, which may be expressed via the hydrodynamic gain  $n_{a \rightarrow v}$  of the initial flow disturbance

$$n_{a \rightarrow v} = \frac{\hat{u}_{v,n}(x_{\text{ref}})}{\hat{u}_{\text{ref}}}. \quad (5.20)$$

The acoustic velocity fluctuations at the reference position  $\hat{u}_a(x_{\text{ref}})$  are referred to as  $\hat{u}_{\text{ref}}$ , for the sake of brevity. The hydrodynamic gain according to Eq. 5.20 accounts for the coupling of the coherent vortical fluctuations  $\hat{u}_{v,n}(x_{\text{ref}})$  to the acoustic velocity fluctuations  $\hat{u}_{\text{ref}}$  at the reference position, which is an empirical constant. The extensive experiments on 'orderly structure in jet-turbulence' provided by Crow and Champagne [64] reveal insights on the hydrodynamic gain  $n_{a \rightarrow v}$  of acoustically forced coherent structures in a non-reactive jet. The coherent velocity fluctuations due to the forced acoustic velocity disturbance at the reference position are coupled by a Strouhal-number and the spatio-temporal dependent gain  $n_{a \rightarrow v}$  measured four tube diameters downstream of the reference plane. The approximation of  $n_{a \rightarrow v} = 1$  holds only in the low Strouhal number, i.e. LF limit. For higher Strouhal numbers, the local gain in turbulence is generally forcing amplitude and frequency dependent and might take values of up to  $n_{a \rightarrow v} = 20$  at the fundamental hydrodynamic mode of the jet at  $\text{St} = f \frac{d_T}{\bar{u}_T} = 0.3$  [64]. Thus, the initial acoustic velocity fluctuation is amplified by a generally non-linear hydrodynamic shear layer instability. Strouhal numbers of up to  $\text{St} = 0.5$  showed a similar yet lower amplification, which is of particular interest since the Strouhal numbers of the reactive experiments conducted in this thesis are in the same order. The gain reaches an asymptotic limit of  $n_{a \rightarrow v} \approx 0$  for very high frequencies in the non-reactive experiments of Crow et al. [64]. Note that results on the forced flame response

of a swirl-stabilised flame show a similar behaviour [87]. For very high frequencies  $f \approx 10000$  Hz no convective flame response is present and the flame is entirely dominated by the local, instantaneous response mechanisms. Although the dynamics of reacting flows might differ from the non-reactive experiments of Crow et al. [64], the results provide insights into the spatial and Strouhal number dependency of the hydrodynamic instability causing the flame dynamics and a reasonable parameter space of the hydrodynamic gain.

### 5.3.2 Acoustics - Turbulence - Flame - Closure

The coherent turbulence - flame - closure of the local coherent vortical velocity fluctuations to the local HRR density fluctuations is provided by the linearised HRR density Eq. 5.2 and the coupling to the local velocity fluctuations via the linearised C-Equation 5.11 and yields

$$\hat{q}_{\text{conv}} = \frac{\hat{\Omega}_t}{\bar{\Omega}_t} \bar{q} = \bar{\rho} \hat{u}_{v,n} \bar{\sigma}_{\text{Fl}} \bar{Y}_F \bar{H}_u. \quad (5.21)$$

The flame response due to coherent vortical velocity fluctuations (Eq. 5.21) generally requires a spatially resolved solution of the coherent velocity fluctuations, which might be obtained from the numerical solution of the linearised Navier-Stokes equations, see Hofmeister [60]. Alternatively, the combination with the hydrodynamic transport model according to Eqs. 5.13 and 5.18 assuming an empirical hydrodynamic gain (Eq. 5.20) yields an analytical model for the coherent turbulent velocity fluctuations. Turbulent diffusion according to Eq. 5.15 yields a decreasing gain over the length of the flame. The hydrodynamic transport model according to Eq. 5.18, however, emphasises the generation of the coherent vortical disturbances within a finite distance from the reference position, which is helpful for the interpretation of the upcoming experimental flame response. Concerning the modelling objectives, the assumption of a hydrodynamic gain (Eq. 5.15) is used in similarity to the  $n$ - $\tau$ - $\sigma$  approach with application to analytical models [6, 28, 31, 32, 51] and the CFD/CAA method [43–46]. The resulting convective HRR density fluctuations due to coherent velocity fluctuations yield the axially distributed flame re-

sponse:

$$\frac{\hat{q}_{\text{conv}}}{\bar{q}} = n \frac{\hat{u}_{\text{ref}}}{\bar{u}_{\text{ref}}} e^{-ik_{\text{diff}}(x-x_{\text{ref}})}. \quad (5.22)$$

The local interaction index  $n$  of the flame response might take different values compared to the non-reactive experiments of Crow et al. due to the differences between the reacting mean flow and a non-reacting mean flow. Dowling et al. [6] suggest a parameter space of  $n = 0 - 10$  in the linear regime for LF thermoacoustics, which seems reasonable judged by the non-reactive experimental insights of Crow and Champagne and Hussain et al. [64–66]. Instead of the fixed initial hydrodynamic gain (Eq. 5.15), the third model (Eq. 5.18) might be used if more detailed information on the mean flow field is provided.

The convective flame response model discussed in this section might be applied to the numerical CFD/CAA method. The mean CFD flow fields provide information on the local turbulent viscosity and the mean flow field. However, analytical methods are required to interpret numerical simulations and experiments. Therefore, the convective flame response is integrated in a low order network model, as discussed in the next section.

## 6 Low Order Network Modelling Theory

Low order network models reveal physical insights on thermoacoustic system stability in the early design phase of rocket and gas turbine combustion chambers, mufflers and dampers. This section introduces a novel quasi-two-port network modelling approach for HF acoustic mode propagation, including an analytical HF flame response model. The goal is to derive generalised acoustic two-port network matrices for a straight duct, an area change and a flame applicable to longitudinal and transverse mode propagation. First, the non-reactive acoustic network model elements, i.e. ducts and area changes, are provided. Second, the flame transfer matrix and function are derived.

### 6.1 High Frequency Transfer Matrix Method

The discussed transfer matrix method is based on the assumption of a given cross-sectional mode shape, i.e. the T1 mode shape in can combustors in the present thesis. This allows to determine the transfer matrices of any acoustic wave in a can combustor by a two-port transfer matrix. The assumption of a certain cross-sectional mode shape (T1, T2, R1, ...) might seem like a restrictive assumption at first glance. Note, however, that the assumption of a cross-sectional mode shape is implicit in all LF lumped parameter models [88] since a constant acoustic pressure and velocity mode shape is assumed. Also, the well-established MMM inherently assumes a given mode shape in longitudinal, azimuthal and radial direction considering transverse modes [47, 75, 79], which is fitted to the measured dynamic pressure data. Thus, the assumption of a given acoustical mode shape is an established and validated approach. The generalisation to HF modes in can combustors is highly appealing since the known theory for LF thermoacoustics might be slightly modified to cover all cross-sectional acoustic mode shapes. The cross-sectional mode shape be-

comes non-trivial, proceeding to the first transverse (T1) mode or the first radial (R1) mode. However, the similarity in the cross-sectional mode shape in acoustic pressure and axial acoustic velocity allows defining the modal acoustic pressure and axial acoustic velocity Eqs. 3.25 and 3.26 normalised with the transverse mode shape. Thus, a transfer matrix  $\text{TM}_{pu}$  in  $p' - u'$  notation

$$\begin{bmatrix} \hat{p}_{mn,do} \\ \hat{u}_{mn,do} \end{bmatrix} = \text{TM}_{pu} \begin{bmatrix} \hat{p}_{mn,up} \\ \hat{u}_{mn,up} \end{bmatrix}, \quad (6.1)$$

is introduced. The transfer matrix  $\text{TM}_{pu}$  describes the axial transfer behaviour from up- to downstream of the acoustic element, i.e. an area change, a duct or a flame. Another common formulation of the two-port transfer matrix is based on the f- and g-waves. The modal acoustic pressure and modal acoustic velocity according to Eqs. 3.25 and 3.26, respectively, are employed to eliminate the g- and subsequently the f-wave. The g-wave is obtained by multiplication of Eq. 3.26 with  $\frac{\rho c}{\kappa_+}$  and subtraction of Eq. 3.25. Similar, the f-wave is obtained by multiplication of Eq. 3.26 with  $\frac{\rho c}{\kappa_-}$  and subtraction of Eq. 3.25, which yields

$$f(x) = \hat{f} e^{-ik_+x} = \frac{\kappa_+}{\kappa_- - \kappa_+} \left( \frac{\rho c \hat{u}_{mn}(x)}{\kappa_+} - \hat{u}_{mn}(x) \right), \quad (6.2)$$

$$g(x) = \hat{g} e^{-ik_-x} = \frac{\kappa_-}{\kappa_+ - \kappa_-} \left( \frac{\rho c \hat{u}_{mn}(x)}{\kappa_-} - \hat{p}_{mn}(x) \right). \quad (6.3)$$

The relations according to Eqs. 6.2 and 6.3 yield the equivalent  $fg$ -transfer matrix:

$$\begin{bmatrix} f_{do} \\ g_{do} \end{bmatrix} = \text{TM}_{fg} \begin{bmatrix} f_{up} \\ g_{up} \end{bmatrix}. \quad (6.4)$$

The transfer matrix in acoustic pressure and velocity Eq. 6.1 and in f- and g-wave Eq. 6.4 are two equivalent notations frequently used for the development of low order network models of thermoacoustic systems.

The scattering matrix  $\text{SM}_{fg}$

$$\begin{bmatrix} f_{do} \\ g_{up} \end{bmatrix} = \text{SM}_{fg} \begin{bmatrix} f_{up} \\ g_{do} \end{bmatrix}, \quad (6.5)$$

reveals physical insights into the scattering processes and is derived from the f- and g-waves given by Eq. 6.4. The scattering matrix  $\text{SM}_{fg}$  is deduced from

Eq. 6.5, which yields

$$\text{SM}_{fg} = \begin{pmatrix} \text{TM}_{fg,11} - \frac{\text{TM}_{fg,12} \cdot \text{TM}_{fg,21}}{\text{TM}_{fg,22}} & \frac{\text{TM}_{fg,12}}{\text{TM}_{fg,22}} \\ -\frac{\text{TM}_{fg,21}}{\text{TM}_{fg,22}} & \frac{1}{\text{TM}_{fg,22}} \end{pmatrix}. \quad (6.6)$$

The next section provides the transfer matrix of a rigid duct for HF and LF acoustics. Afterwards, the integral jump conditions covering an area expansion and a flame and the resulting transfer matrices are presented.

## 6.2 Duct Transfer Matrix

The acoustic HF transfer matrix from upstream  $x_{\text{up}} = 0$  to downstream  $x_{\text{do}} = L$  of a rigid duct of constant cross-section is derived from the solution of the Bessel differential equation, see Section 3.4. The solution of the modal acoustic pressure (Eq. 3.25) and the axial acoustic velocity (Eq. 3.26) at the downstream side  $x_{\text{do}} = L$  yields

$$\hat{p}_{\text{mn}}(x_{\text{do}} = L) = \hat{f} e^{-ik_+L} + \hat{g} e^{-ik_-L}, \quad (6.7)$$

$$\hat{u}_{\text{mn}}(x_{\text{do}} = L) = \frac{\kappa_+}{\rho c} \hat{f} e^{-ik_+L} + \frac{\kappa_-}{\rho c} \hat{g} e^{-ik_-L}. \quad (6.8)$$

According to Eqs. 6.2 and 6.3, the complex amplitudes  $\hat{f}$  and  $\hat{g}$  of the up- and downstream travelling waves  $f(x) = \hat{f} e^{-ik_+x}$  and  $g(x) = \hat{g} e^{-ik_-x}$ , respectively, are obtained from the upstream side of the duct

$$\hat{f} = \frac{\kappa_+}{\kappa_- - \kappa_+} \left( \frac{\rho c \hat{u}_{\text{mn}}(x_{\text{up}} = 0)}{\kappa_+} - \hat{p}_{\text{mn}}(x_{\text{up}} = 0) \right), \quad (6.9)$$

$$\hat{g} = \frac{\kappa_-}{\kappa_+ - \kappa_-} \left( \frac{\rho c \hat{u}_{\text{mn}}(x_{\text{up}} = 0)}{\kappa_-} - \hat{p}_{\text{mn}}(x_{\text{up}} = 0) \right). \quad (6.10)$$

The f- and g-wave amplitudes according to Eqs. 6.9 and 6.10 are inserted into Eqs. 6.7 and 6.8 and rearranged in transfer matrix notation, which yields the transfer matrix of a rigid duct of constant cross-section:

$$\text{TM}_{pu,D} = \begin{bmatrix} -\frac{\kappa_-}{\kappa_+ - \kappa_-} e^{ik_+L} + \frac{\kappa_+}{\kappa_- - \kappa_+} e^{ik_-L} & -\frac{\rho c}{\kappa_+ - \kappa_-} e^{ik_+L} - \frac{\rho c}{\kappa_- - \kappa_+} e^{ik_-L} \\ \frac{1}{\rho c} \left( \frac{\kappa_- \kappa_+}{\kappa_+ - \kappa_-} e^{ik_+L} + \frac{\kappa_+ \kappa_-}{\kappa_- - \kappa_+} e^{ik_-L} \right) & \frac{\kappa_+}{\kappa_+ - \kappa_-} e^{ik_+L} + \frac{\kappa_-}{\kappa_- - \kappa_+} e^{ik_-L} \end{bmatrix}. \quad (6.11)$$

The equivalent f- and g-wave transfer matrix according to Eq. 6.4 yields

$$\text{TM}_{fg,D} = \begin{bmatrix} e^{-ik_+L} & 0 \\ 0 & e^{-ik_-L} \end{bmatrix}. \quad (6.12)$$

Very similar transfer matrices are given in the literature for can annular combustors [50,89]. Simplification of the transfer matrix  $\text{TM}_{pu,D}$  is obtained with a low Mach number assumption  $\frac{\kappa_{\pm}}{\kappa_{\mp} - \kappa_{\pm}} = -\frac{1}{2}$ . However, the  $\text{TM}_{pu,12}$  and  $\text{TM}_{pu,21}$  elements still contain frequency-dependent normalised wave numbers in the low Mach limit. Note that the longitudinal and transverse/radial wave propagation is included in Eq. 6.11 depending on the argument of the Bessel function with  $\alpha_{mn} = 0$  for LF and  $\alpha_{mn} \neq 0$  for HF wave propagation. In the LF, low Mach number case, the wave numbers further reduce to  $k_{\pm} = \pm k$  and the classical duct transfer matrix is obtained.

Contrary to the acoustic wave propagation in a straight duct, the derivation of the acoustic area change transfer matrix and thermoacoustic flame transfer matrix requires integral conservation equations, which are discussed in the next section.

### 6.3 Integral HF Acoustic Jump Conditions

The linearised conservation of mass, momentum and energy are the governing equations for any analytical jump condition. However, different strategies exist in aero-/thermoacoustic literature to obtain integral acoustic jump conditions from the governing equations.

The linearised momentum conservation in the low Mach number limit yields an acoustic pressure coupling condition for acoustic network elements. The proper choice of the conservation equation concerning the acoustic velocity transfer function, however, is less trivial and a discussion of the state-of-the-art is worthwhile. The linearised acoustic mass (Eq. 3.7), energy (Eq. 3.9) or disturbance energy (Eq. 3.10) conservation are possible choices used in literature. The LF acoustic literature is dominated by the use of the linearised mass conservation for the acoustic velocity transfer function across an area

change [47, 71, 74]. The use of the linearised energy conservation Eq. 3.9 is common practice for the derivation of LF thermoacoustic jump conditions across a flame [3, 4, 6]. Both the linearised mass and energy conservation yield the volume velocity  $\int u'_x dA = \text{const.}$  as the conservation quantity across area changes and flames. Generally, the conservation of the acoustic disturbance energy has to be considered as indicated by Pierce et al. [88] which implies the acoustic power flux  $p'u'$ . In the LF limit, the acoustic power flux  $p'u'$  transmitted across a sudden area expansion also yields the volume velocity as the conservation quantity since  $p' = \text{const.}$  applies. Thus, the jump condition is independent of the choice of the linearised mass, energy or power conservation for an LF acoustic area expansion. In the HF limit, axial acoustic compactness  $p'_{mn}(x) = \text{const.}$  is a reasonable approximation particularly close to the cut-on frequency. However, the acoustic mode shape in the cross-sectional direction needs to be taken into account. Thus, the integral linearised momentum conservation and the integral disturbance energy conservation according to Chapter 3 are employed to obtain the acoustic jump conditions across sudden area expansions and flames, with the restriction to low Mach numbers. The linearised momentum conservation and the integral disturbance energy conservation read in frequency domain

$$\int i\omega\bar{\rho}\hat{u}_i dV + \oint \hat{p}n_i dA = 0, \quad (6.13)$$

$$\int \frac{\partial}{\partial t} \left( \frac{\Re[\tilde{p}^* \tilde{p}]}{2\bar{\rho}\bar{c}^2} + \frac{\bar{\rho}}{2} \Re[\hat{u}_j^* \tilde{u}_j] \right) dV + \oint \Re[\tilde{p}^* \tilde{u}_j] n_j dA = \frac{\bar{\kappa} - 1}{\bar{\rho}\bar{c}^2} \int \Re[\tilde{p}^* \tilde{q}] dV, \quad (6.14)$$

where the frequency domain representation of the acoustic disturbance energy conservation is given by the period average of the real-valued disturbance energy conservation (Eq. 3.11) [4]. Note that the period average of the non-linear product of two complex numbers  $z_1, z_2$  is given by the real value of the product with the complex conjugate  $\frac{1}{T} \int_0^T z_1 z_2 dT = \frac{1}{2} \Re[z_1^* z_2]$ . The time-dependent amplitude of the acoustic pressure  $\tilde{p}(t) = \hat{p}e^{\alpha_g t}$ , acoustic velocity  $\tilde{u}_j(t) = \hat{u}_j e^{\alpha_g t}$  and the HRR density  $\tilde{q}(t) = \hat{q} e^{\alpha_g t}$  fluctuations generally depend on the growth rate  $\alpha_g$ , assuming their time scale is large  $1/\alpha_g \gg 1/f$  compared to the acoustic time scale, i.e. the period  $T = 1/f$  [4].

The first term on the left-hand side of the integral momentum conservation Eq. 6.13 accounts for the unsteady change of momentum in the control

volume, i.e. the oscillating mass. The second term is the pressure force, i.e. the momentum flux at the boundaries of the control volume. Similarly, the period-averaged disturbance energy conservation Eq. 6.14 accounts for the unsteady change of the acoustic energy  $E_a = \int \frac{\partial}{\partial t} \left( \frac{1}{2\bar{\rho}\bar{c}^2} \Re[\hat{p}^* \hat{p}] + \frac{\bar{p}}{2} \Re[\hat{u}_j^* \hat{u}_j] \right) dV$  (Eq. 3.12) in the control volume, i.e. the growth of the instability, by the first term on the left-hand side and the acoustic power flux  $F_a = \oint \Re[\hat{p}^* \hat{u}_j] n_j dA$  (Eq. 3.13) over the system boundaries via the second term and an additional source term  $S_a = \frac{\bar{\kappa}-1}{\bar{\rho}\bar{c}^2} \int \Re[\hat{p}^* \hat{q}] dV$  (Eq. 3.14) due to unsteady heat release. In the following a quasi-steady model for the area jump and flame transfer matrices is derived, such that  $E_a$  vanishes. The objective is to obtain the modal acoustic pressure jump condition from the integral momentum conservation (Eq. 6.13) and the modal axial acoustic velocity jump condition from the disturbance energy conservation (Eq. 6.14).

Before the resulting jump conditions for the specific cases of a flame and a sudden area change are provided (see Secs. 6.4 and 6.5) the integration boundaries in cross-sectional direction of Eqs. 6.13 and 6.14 for HF modes are discussed, introducing the concept of effective acoustic modal areas  $A_{mn}$ . Therefore, the integration boundaries applied to the integral conservation equations (Eqs. 6.13 and 6.14) are obtained by the separation of the HF acoustic mode at the acoustic pressure nodal lines  $p'(r, \theta) = 0$  and the transverse/radial acoustic velocity nodal lines  $u'_{r,\theta}(r, \theta) = 0$ . This corresponds to the separation of the acoustic mode into multiple domains of constant positive or negative sign of the real-valued acoustic pressure and the corresponding axial acoustic velocity in cross-sectional direction. The resulting integration boundaries in cross-sectional direction are, thus, determined by the transverse/radial nodal lines of the acoustic power flux  $(p' u')(r, \theta) = 0$ , which yields

$$\oint \Re[\hat{p}^* \hat{u}_j] n_j dA = \int_{r_{\min}}^{r_{\max}} \int_{\theta_{\min}}^{\theta_{\max}} \Re[(\hat{p}^* \hat{u}_x)(x_{do})] r d\theta dr - \int_{r_{\min}}^{r_{\max}} \int_{\theta_{\min}}^{\theta_{\max}} \Re[(\hat{p}^* \hat{u}_x)(\theta, x_{up})] r d\theta dr. \quad (6.15)$$

Thus, the choice of the integration boundaries at  $(p' u')(r, \theta) = 0$  simplifies the closed surface integral of the acoustic power flux in Eq. 6.14 to the difference of the axial acoustic power flux from  $x_{up}$  upstream to  $x_{do}$  downstream of the acoustic element. The conditions for the integration boundaries  $u'_{r,\theta}(r, \theta) = 0$

and  $p'(r, \theta) = 0$  simplify to

$$J_n(r)P_m(\theta) = 0, \quad (6.16)$$

$$\frac{\partial J_n(r)}{\partial r} = 0, \quad (6.17)$$

with restriction to cylindrical combustors, see Eq. 3.20 and 3.19. The integration boundaries in radial and azimuthal direction obtained via Eqs. 6.16 and 6.17 are indicated with  $r_{\min}$ ,  $r_{\max}$  and  $\theta_{\min}$ ,  $\theta_{\max}$ , respectively, in the following. Making use of the modal acoustic pressure  $\hat{p}_{mn}$  (Eq. 3.25) and the modal axial acoustic velocity  $\hat{u}_{mn}$  (Eq. 3.26) the axial acoustic power fluxes (Eq. 6.15) are split into the axial and cross-sectional dependency

$$\Re\left[\int \hat{p}^* \hat{u}_x dA\right] = \Re\left[(\hat{p}^* \hat{u})_{mn}(x) \int_{r_{\min}}^{r_{\max}} \int_{\theta_{\min}}^{\theta_{\max}} J_n(r)^2 P_m(\theta)^2 r d\theta dr\right]. \quad (6.18)$$

For ease of notation the index applied to the bracket reads  $(\hat{p}^* \hat{u})_{mn}(x) = \hat{p}_{mn}^* \hat{u}_{mn}(x)$  in the following. The axial dependency  $(\hat{p}^* \hat{u})_{mn}(x)$  is of the dimension  $\text{Wm}^{-2}$ . The cross-sectional integral  $\int_A J_n(r)^2 P_m(\theta)^2 dA$  is of the dimension  $\text{m}^2$  since the radial and azimuthal ansatz functions of the acoustic field  $J_n(r)$  and  $P_m(\theta)$ , respectively, are non-dimensional. Therefore, the effective modal acoustic area  $A_{mn}$  is introduced depending on the cross-sectional ansatz functions of the acoustic field, which is further separated into

$$A_{mn} = \int_{r_{\min}}^{r_{\max}} \int_{\theta_{\min}}^{\theta_{\max}} J_n(r)^2 P_m(\theta)^2 r d\theta dr = \int_{\theta_{\min}}^{\theta_{\max}} P_m(\theta)^2 d\theta \int_{r_{\min}}^{r_{\max}} J_n(r)^2 r dr. \quad (6.19)$$

The effective modal acoustic area (Eq. 6.19) simplifies the notation of the acoustic power flux in axial direction to

$$\Re\left[\int \hat{p}^* \hat{u}_x dA\right] = \Re\left[(\hat{p}^* \hat{u})_{mn}(x) A_{mn}(r, \theta)\right], \quad (6.20)$$

which is used in the following derivations of the transfer matrices. The separation of the acoustic domain is illustrated in Fig. 6.1 for the investigated configuration in the present thesis and a generic configuration with a single injector tube showing the cross-sectional acoustic pressure mode shape

of the T1 mode and the R1 mode, respectively. The cross-sectional injector tube position is indicated at  $r_T, \theta_T$  relative to the cylindrical coordinate system. The vertical axis starting from the radial origin  $r = 0$  in the centre of the chamber is indicated as the azimuthal origin  $\theta = 0$ . The injector tubes are acoustically compact in transverse/radial direction for the considered T1 and R1 mode. Thus, the effective modal acoustic area simplifies to the discretised sum of the geometrical injector tube areas  $A_T = \pi/4 d_T^2$  weighted with the transverse/radial acoustic field  $A_{mn,T} = \sum_i A_T J_n(r_T)^2 P_m(R_\theta, \theta_T)^2$  at the injector tube position  $r_T, \theta_T$  within the cross-sectional integration boundaries according to Eqs. 6.16 and 6.17. The integration boundaries in radial direction, illustrated with the R1 mode on the right-hand side of Fig. 6.1, are determined by the combustion chamber wall (Eq. 6.17) and the nodes of the Bessel function  $J_1(r) = 0$  (Eq. 6.16) indicated by the dashed circle at  $r = 0.63 d_C/2$ . Solely the effective modal acoustic area (Eq. 6.19) of the inner circle of the R1 mode  $A_{01,C} = \int_{-\pi}^{+\pi} P_0(\theta)^2 d\theta \int_0^{0.63 d_C/2} J_1(r)^2 r dr$  and the single injector tube  $A_{01,T} = A_T J_1(r_T = 0)^2 P_0(R_\theta, \theta_T = 0)^2$  have to be considered for the axial modal acoustic velocity jump condition (Eq. 6.15). The nodal line  $\theta_m$  of the T1 mode is indicated by the horizontal dashed line and is given by  $\theta_1 = \pm\pi/2$ . The generalisation to higher azimuthal mode numbers  $m > 1$  is straightforward and yields the nodal line positions  $\theta_m = \pm\pi/2^m$ . Thus, the azimuthal integration boundaries are determined solely by the azimuthal acoustic pressure nodal line position  $P_m(\theta) = 0$  (Eq. 6.16), which yields  $\theta_{\min} = -\pi/2^m$  and  $\theta_{\max} = +\pi/2^m$ . The radial integration boundaries are provided by the combustor wall for the case of the T1 mode. The effective modal acoustic area according to Eq. 6.19 yields  $A_{10,C} = \int_{-\pi/2}^{+\pi/2} P_1(\theta)^2 d\theta \int_0^{d_C/2} J_0(r)^2 r dr$  and for the 4 injector tubes in each half of the mode  $A_{10,T} = \sum_i^4 A_T J_0(r_T)^2 P_1(R_\theta, \theta_T)^2$ , which have to be considered for the axial modal acoustic velocity jump condition (Eq. 6.15) for the depicted case of the T1 mode.

The integral momentum and the quasi-steady acoustic disturbance energy conservation according to Eqs. 6.13 and 6.14 are rewritten using the effective modal acoustic area (Eq. 6.19), the modal acoustic pressure (Eq. 3.25) and the modal axial acoustic velocity (Eq. 3.26), which yields

$$\hat{p}_{mn}(x_{do}) - \hat{p}_{mn}(x_{up}) = - \int i\omega \bar{\rho} \hat{u}_{mn} dx, \quad (6.21)$$

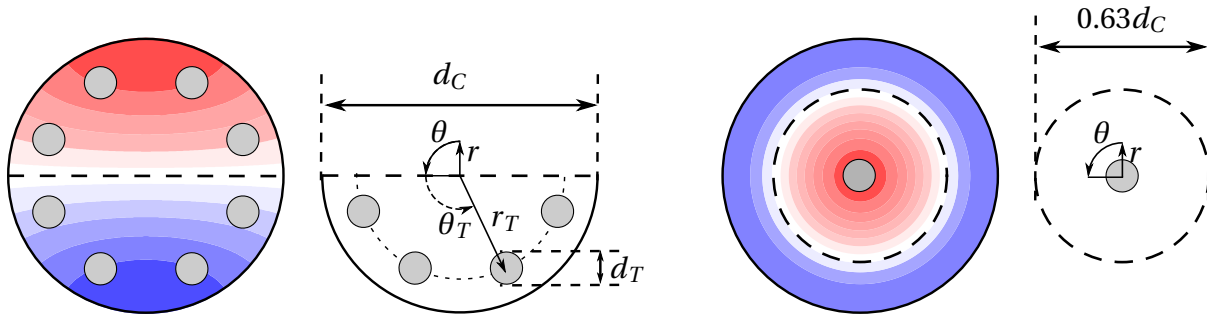


**Figure 6.1:** Cross-sectional acoustic pressure mode shape of the T1 mode for the injector coupling at the dump plane of the MJC configuration in the present thesis and for a generic configuration of a single injector tube coupled to the R1 mode to illustrate the separation of the acoustic domain at the transverse nodal lines and the combustor wall to obtain the cross-sectional integration boundaries of Eqs. 6.13 and 6.14.

$$\Re[(\hat{p}^* \hat{u}A)_{mn}(x_{do})] - \Re[(\hat{p}^* \hat{u}A)_{mn}(x_{up})] = \frac{\bar{\kappa} - 1}{\bar{\rho} \bar{c}^2} \int \Re[\hat{p}^* \hat{q}] dV, \quad (6.22)$$

to deduce the transfer matrices according to Eq. 6.1. For the sake of brevity the dependencies of the effective modal acoustic area on radial and azimuthal coordinates are omitted such that Eq. 6.20 reads  $(\hat{p} \hat{u}A)_{mn}(x)$ , where the axial dependency originates from  $(\hat{p} \hat{u})_{mn}$  (Eqs. 3.25 and 3.26). The assumption of cross-sectional compactness of the injector tubes in relation to the transverse/radial acoustic field is used to obtain the momentum conservation according to Eq. 6.21.

The next sections provide the thermoacoustic network elements covering a straight duct, a sudden area expansion and a flame, making use of the integral conservation equations according to Eqs. 6.21 and Eq. 6.22.

## 6.4 Area Change Transfer Matrix

The momentum conservation reduces to a local constant pressure jump condition since only the open interface upstream and downstream of the area jump has to be considered. The first term in the momentum conservation (Eq.

6.21) represents the oscillating mass at the exit of a duct due to the acoustic inertia at the area change, which yields an effective length correction of the duct

$$\int i\omega\bar{\rho}\hat{u}_{mn} dx = i\omega\bar{\rho}\hat{u}_{mn,up}L_{\text{eff}}, \quad (6.23)$$

similar to common LF acoustics [47, 88]. The effective length  $L_{\text{eff}}$  might be non-negligible concerning the predicted frequencies. The first term in Eq. 6.14 might be accounted equivalent to a reduced length [47]. However, assuming an axially compact area jump the reduced length is negligible. Thus, the jump conditions across a compact sudden area expansion obtained from the linearised acoustic momentum and disturbance energy conservation yield

$$\hat{p}_{mn,do} = \hat{p}_{mn,up} - i\omega\bar{\rho}L_{\text{eff}}\hat{u}_{mn,up}, \quad (6.24)$$

$$(\hat{u}A)_{mn}(x_{do}) = (\hat{u}A)_{mn}(x_{up}). \quad (6.25)$$

The acoustic transfer matrix of a sudden area expansion neglecting convective effects yields

$$\text{TM}_{pu,A} = \begin{bmatrix} 1 & -i\omega\bar{\rho}L_{\text{eff}} \\ 0 & \frac{A_{mn,up}}{A_{mn,do}} \end{bmatrix}, \quad (6.26)$$

a constant acoustic pressure and an axial acoustic velocity jump condition dependent on the ratio of the effective modal acoustic areas  $\frac{A_{mn,up}}{A_{mn,do}}$ . The equivalent expression according to Eq. 6.4 yields the f- and g-wave transfer matrix

$$\text{TM}_{fg,A} = \begin{bmatrix} \frac{\rho_{do}c_{do}}{\rho_{up}c_{up}} \frac{A_{mn,up}}{A_{mn,do}} \frac{\kappa_{up+} - 1}{\kappa_{do-}} & \frac{\rho_{do}c_{do}}{\rho_{up}c_{up}} \frac{A_{mn,up}}{A_{mn,do}} \frac{\kappa_{up-} - 1}{\kappa_{do-}} \\ \frac{\kappa_{do+} - 1}{\kappa_{do-}} & \frac{\kappa_{do+} - 1}{\kappa_{do-}} \\ \frac{\rho_{do}c_{do}}{\rho_{up}c_{up}} \frac{A_{mn,up}}{A_{mn,do}} \frac{\kappa_{up+} - 1}{\kappa_{do+}} & \frac{\rho_{do}c_{do}}{\rho_{up}c_{up}} \frac{A_{mn,up}}{A_{mn,do}} \frac{\kappa_{up-} - 1}{\kappa_{do+}} \\ \frac{\kappa_{do-} - 1}{\kappa_{do+}} & \frac{\kappa_{do-} - 1}{\kappa_{do+}} \end{bmatrix}, \quad (6.27)$$

of the compact area change for  $L_{\text{eff}} = 0$ . The major differences compared to the LF case is the ratio of the effective, modal areas  $\frac{A_{mn,up}}{A_{mn,do}}$  instead of the geometrical areas and the additional frequency dependency associated with the ratio of the normalised wave numbers  $\frac{\kappa_{up\pm}}{\kappa_{do\pm}}$ . The normalised axial acoustic wave number in the low Mach number limit  $\kappa_{\pm} = \frac{k_{\pm}}{k} = \pm\sqrt{1 - k_{mn}/k^2}$  depends on the axial acoustic wave number of the acoustic mode  $k_{\pm}$  (Eq. 3.24) and thus on the cross-sectional mode shape (T1,R1,...). Restriction to LF acoustics is applied by the argument of the Bessel function  $\alpha_{mn} = 0$ , which implies  $k_{mn} = \frac{\alpha_{mn}}{r} = 0$  for longitudinal wave propagation.

## 6.5 Flame Transfer Matrix

The Flame Transfer Matrix (FTM) captures the acoustic pressure and axial acoustic velocity transfer function of the flame. The momentum conservation (Eq. 6.13) across the HRR zone of all flames reduces to a constant modal acoustic pressure coupling condition

$$\hat{p}_{mn,b}(x) = \hat{p}_{mn,u}(x) \quad (6.28)$$

considering Eq. 3.25 for the azimuthal mode number  $m$  and the radial mode number  $n$  for a quasi-steady flame response in a duct of constant cross-section. The quasi-steady assumption might be omitted for a generalised model, solving the integral of the acoustic inertia on the left-hand side of Eq. 6.21 for the modal axial acoustic velocity mode shape  $\hat{u}_{mn}$ . The non-compact thermoacoustic driving potential of unsteady heat release is commonly evaluated by the Rayleigh integral [12] in the disturbance energy conservation. Thus, in order to obtain a non-compact FTF, the integral disturbance energy conservation (Eq. 6.22) is considered. Similar, to the acoustic inertia, the volume integral on the left-hand side of Eq. 6.22 might be solved for the modal acoustic pressure and modal axial velocity mode shape in a duct of constant cross-section (Eqs. 3.25 and 3.26). The disturbance energy conservation according to Eq. 6.22 is used to obtain the acoustic energy volume flux downstream of the flame assuming constant gas properties

$$\Re[(\hat{p}^* \hat{u}A)_{mn,b}] - \Re[(\hat{p}^* \hat{u}A)_{mn,u}] = \frac{\bar{\kappa} - 1}{\bar{\rho} \bar{c}^2} \int \Re[\hat{p}^* \hat{q}] dV. \quad (6.29)$$

Although a quasi-steady flame response is assumed, the acoustic non-compactness of the flame and thus the integral of the local Rayleigh indices is still accounted by Eq. 6.29. Considering cylindrical combustion chambers the thermoacoustic jump condition across the flame accounts for the cross-sectional and axial non-compactness of the mode by the radial, azimuthal and axial acoustic mode ansatz functions  $J_n(r)$ ,  $P_m(\theta)$  and  $f(x)$ ,  $g(x)$ , respectively.

The mean gas properties are commonly expressed via the burned and unburned gas temperature employing the integral thermal power  $\bar{Q} = \bar{\rho} \bar{u}_u A_u \bar{Y}_F \bar{H}_u$  [48]. The burned gas temperature at adiabatic conditions (Eq.

2.12) yields  $\bar{c}_p(\bar{T}_b - \bar{T}_u) = \bar{Y}_F \bar{H}_u$  which gives  $\bar{Q} = \bar{\rho} \bar{u}_u A_u \bar{c}_p (\bar{T}_b - \bar{T}_u)$ . In order to obtain the dependency on the heat capacity ratio  $\bar{\kappa}$  the isobaric heat capacity  $\bar{c}_p = \bar{\kappa} \bar{c}_v$  and the ideal gas law  $\bar{\rho}_u \bar{T}_u = \frac{\bar{p}}{R_u}$  is employed to obtain  $\frac{\bar{\kappa}-1}{\bar{\kappa} \bar{p}} = \frac{\bar{u}_u A_u}{\bar{Q}} \left( \frac{\bar{T}_b}{\bar{T}_u} - 1 \right)$  which in combination with Eq. 6.29 yields

$$\frac{\Re[(\hat{p}^* \hat{u} A)_{mn,b}]}{\Re[(\hat{p}^* \hat{u} A)_{mn,u}]} = 1 + \left( \frac{\bar{T}_b}{\bar{T}_u} - 1 \right) \frac{\int \Re[\hat{p}^* \hat{q}] dV / \bar{Q}}{\Re[(\hat{p}^* \hat{u} A)_{mn,u}] / (\bar{u} A)_u}. \quad (6.30)$$

In order to obtain a modal acoustic velocity jump condition from Eq. 6.30 a duct of constant cross-section is considered, which implies  $A_{mn,u} = A_{mn,b}$ . In combination with the acoustic pressure coupling condition  $p'_{mn,b} = p'_{mn,u}$  (Eq. 6.28) the ratio of the unburned and burned acoustic energy flux in Eq. 6.30 simplifies to  $\frac{\Re[(\hat{p}^* \hat{u} A)_{mn,b}]}{\Re[(\hat{p}^* \hat{u} A)_{mn,u}]} = \frac{\hat{u}_{mn,b}}{\hat{u}_{mn,u}}$ . Thus, the transfer matrix coupling the modal acoustic pressure and axial acoustic velocity ( Eq. 6.1) of the flame is obtained

$$\text{FTM} = \begin{bmatrix} 1 & 0 \\ 0 & \left( 1 + \left( \frac{\bar{T}_b}{\bar{T}_u} - 1 \right) \text{FTF} \right) \end{bmatrix}, \quad (6.31)$$

where the FTF according to

$$\text{FTF} = \frac{\int \hat{p}^* \hat{q} dV / \bar{Q}}{(\hat{p}^* \hat{u} A)_{mn,u} / (\bar{u} A)_u} \quad (6.32)$$

accounts for the local Rayleigh indices  $ri = \hat{p} \hat{q}$  due to all possible flame driving mechanisms for longitudinal and transverse mode propagation. The real part is omitted since  $(\hat{p}^* \hat{u})_{mn,u}$  at the unburned reference position  $x_u = 0$  and  $A_{mn,u}$  are real numbers and thus the imaginary part depends solely on the Rayleigh integral. In the LF limit the acoustic pressure is constant over the entire flame volume and the effective modal acoustic area is equal to the geometrical cross-section and the FTF reduces to  $\text{FTF} = \frac{\hat{Q} / \bar{Q}}{\hat{u}_u / \bar{u}_u}$ . For HF modes, the local Rayleigh indices  $ri$  might be obtained from the pressure mode shape and the local HRR density fluctuations to account for non-compact flame dynamics.

The Rayleigh integral according to Eq. 6.32 might be separated into the radial, azimuthal and axial dependency considering can combustors. The modal

acoustic pressure (Eq. 3.25) depends solely on the axial coordinate  $p'_{mn}(x)$ . Considering compact flames with respect to the axial acoustic pressure mode the FTF might be simplified to

$$\text{FTF} = \frac{\int J_n(r)P_m(\theta)\hat{q}dV/\bar{Q}}{(\hat{u}A)_{mn,u}/(\bar{u}A)_u} \quad (6.33)$$

In similarity to the exiting LF thermoacoustic theory, the global modal HRR fluctuations

$$\dot{Q}'_{mn} = \Re[\int J_n(r)P_m(\theta)\hat{q}dV] \quad (6.34)$$

might be interpreted as the acoustic pressure weighted, integral HRR fluctuations for non-compact flames. The integral pressure weighted HRR fluctuations  $\dot{Q}'_{mn} = \int \dot{Q}'_{mn,x}dx$  might be expressed via the cross-sectional integrated modal HRR density fluctuations

$$\dot{Q}'_{mn,x} = \Re[\int J_n(r)P_m(\theta)\hat{q}dA] \quad (6.35)$$

in the following.

The radial and azimuthal dependency  $J_n(r)P_m(\theta)$  are crucial to obtain the correct non-compact flame response according to Eq. 6.34 since the phase of the acoustic mode varies due the transverse/radial acoustic mode shape. The axial acoustic pressure mode shape is neglected in Eq. 6.33 assuming acoustic compactness of the flame in axial direction. An axially acoustic compact flame is justified for a small axial Helmholtz number  $\text{He}_x = L_{\text{Fl}}k_{\pm} \ll 1$  given by the axial flame length  $L_{\text{Fl}}$  and the axial acoustic wave number  $k_{\pm}$  (Eq. 3.24), which is particularly reasonable close to the cut-on frequency of the HF mode ( $k_{\pm} = 0$ ).

The FTF is discussed in the following section with focus on the convective flame response.

## 6.6 Axially Distributed Convective FTF in a MJC

This section provides the relation of the integral convective FTF to the radially integrated but axially resolved  $\text{FTF}_x$  based on  $\hat{Q}'_{mn,x}$  in MJs. A simplified in-

tegral convective FTF for MJC's is discussed to emphasise the dominant mean flow dependency of the non-compact FTF.

The flame response might be expressed via an axially resolved  $\text{FTF}_x$  based on the axially resolved modal HRR fluctuations

$$\text{FTF}_x = \frac{\hat{Q}_{\text{mn},x} / \bar{Q}_x}{(\hat{u}A)_{\text{mn},u} / (\bar{u}A)_u}, \quad (6.36)$$

using the cross-sectional integrated, yet axially resolved modal HRR density fluctuations according to Eq. 6.35 and the cross-sectional integrated mean HRR reads  $\bar{Q}_x = \int \bar{q} dA$ . Replacing  $\hat{Q}_{\text{mn},x}$  in the integral FTF (Eq. 6.33) yields

$$\text{FTF} = \int_x \xi(x) \text{FTF}_x(x) dx. \quad (6.37)$$

The factor  $(\hat{u}A)_{\text{mn},u} / (\bar{u}A)_u$  vanishes due to the normalisation of the FTF. The axial mean HRR density distribution

$$\xi = \frac{\bar{Q}_x}{\bar{Q}} \quad (6.38)$$

is introduced. The resulting global FTF (Eq. 6.37) is given by the convolution of the  $\text{FTF}_x$  with the axial mean HRR density distribution (Eq. 6.38). The convolution in cross-sectional direction is captured by  $\hat{Q}_{\text{mn},x}$  (Eq. 6.35) in the  $\text{FTF}_x$  (Eq. 6.36). Since the optical measurements of the flame dynamics by  $\text{OH}^*$  chemiluminescence provide line-of sight integrated images, the axially resolved  $\text{FTF}_x$  can be estimated from the optical results for validation of the flame response model in Chapter 9.4.

The objective in the following is to deduce the dependency of the axially resolved  $\text{FTF}_x(x)$  and the global FTF on the locally resolved  $\text{ftf}(x, r, \theta)$  to obtain a simplified analytical convective FTF for MJC's. Therefore, consider a MJC with multiple injector tubes of the same diameter and length flush-mounted in a planar front plate, as depicted in Fig. 6.2. The overall mass flow is split equally to each jet flame resulting in similar fluid-dynamical conditions at each flame. Concerning negligible flame-flame interaction, symmetric flame stabilisation results in the same reaction rate at each flame in cross-sectional direction. The

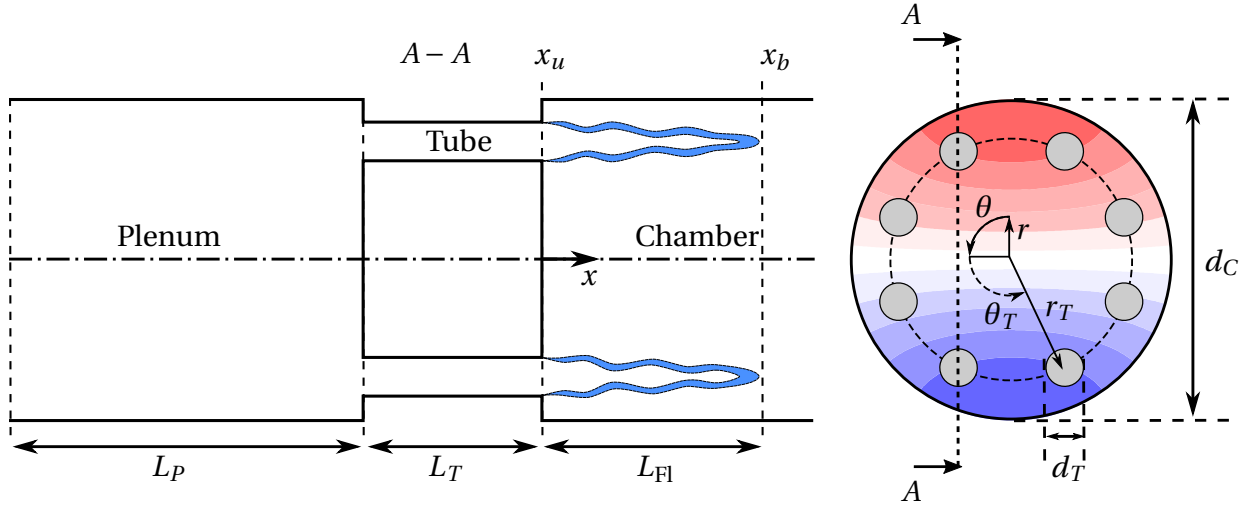


**Figure 6.2:** Sketch of the investigated MJC configuration and the acoustic pressure mode shape of the T1 mode and the expected convective flame response to illustrate the dependency of the locally resolved  $\text{ftf}(x, r, \theta)$  to the axially resolved  $\text{FTF}_x(x)$  and the global FTF.

locally resolved  $\text{ftf}$  yields the HRR density fluctuations  $\hat{q}_{\text{conv}}(x, r, \theta) = \frac{\bar{q}}{\bar{u}_u} \hat{u} \text{ftf}$  in Eq. 6.35 for the axially resolved  $\text{FTF}_x$  according to Eq. 6.36. The result for Eq. 6.35 yields

$$\hat{Q}_{mn,x} = \int_A J_n(r) P_m(\theta) \frac{\hat{u}_u}{\bar{u}_u} \cdot \bar{q} \text{ftf}(x, r, \theta) dA. \quad (6.39)$$

The axial acoustic velocity  $\hat{u}_u(x_u, r, \theta)$  at the fixed axial position  $x_u$  upstream of the flame at unburned conditions, see Fig. 6.2, is expressed via Eq. 3.26. The modal axial acoustic velocity  $\hat{u}_{mn,u} \neq f(r, \theta)$  upstream of the flame is constant in cross-sectional direction, mind the normalisation with  $J_n(r) P_m(\theta)$  in Eq. 3.26. The mean velocity  $\bar{u}_u \neq f(r, \theta)$  is the same at each jet flame, for an even mass flow split. Thus, the normalisation of the  $\text{FTF}_x$  (Eq. 6.36) using Eq. 6.39, yields

$$\text{FTF}_x = \frac{\int J_n(r)^2 P_m(\theta)^2 \cdot \bar{q} \text{ftf}(x, r, \theta) dA / \bar{Q}_x}{A_{mn,u} / A_u}, \quad (6.40)$$

since  $\hat{u}_{mn,u} / \bar{u}_u \neq f(r, \theta)$  vanishes. Considering acoustically compact flames in transverse/radial direction, the integral, cross-sectional mean value of

$J_n(r)^2 P_m(\theta)^2$  is used to simplify the cross-sectional integral in Eq. 6.39 to

$$\int J_n(r)^2 P_m(\theta)^2 \cdot \bar{q} \text{ftf}(x, r, \theta) dA = \frac{A_{mn,u}}{A_u} \int \bar{q} \text{ftf}(x, r, \theta) dV. \quad (6.41)$$

Thus, the effective modal acoustic area  $A_{mn,u} = \int_{A_u} J_n(r)^2 P_m(\theta)^2 dA$  and the integral injector tube cross-section at the reference plane  $A_u$  in Eq. 6.40 vanish, considering a duct of constant cross-section. The axially resolved  $\text{FTF}_x$  according to Eq. 6.40 simplifies to

$$\text{FTF}_x(x) = \frac{1}{\bar{Q}_x} \int \bar{q} \cdot \text{ftf}(x, r, \theta) dA. \quad (6.42)$$

Thus, the cross-sectional area average of the local flame transfer function  $\text{ftf}(x, r, \theta)$  weighted with the HRR density yields the axially distributed  $\text{FTF}_x$ , i.e. the axial projection of the local, generally three-dimensional flame transfer function according to Eq. 6.42. The integration of the local flame transfer function  $\text{ftf}$  in cross-sectional direction might generally include a variable phase, i.e. time delay, of the locally resolved  $\text{ftf}$ . In this case, the axially distributed  $\text{FTF}_x$  might be modelled by the superposition of multiple flame transfer functions of different time delay.

In the following, a local time delay model is considered  $\text{ftf} = n(x) e^{i\omega\tau(x)} = n(x) e^{ik_{\text{conv}}(x-x_u)}$ . Similar fluid-dynamical conditions by means of the Strouhal number of the jet flames are assumed. In this case, the time delay of the locally resolved  $\text{ftf}$  is similar at each flame since the mean axial flow velocity of the convective HRR density fluctuations averaged at each jet flame is the same. Thus, the cross-sectional average of the convective wave number at each jet flame is invariant in cross-sectional direction  $k_{\text{conv}} \neq f(r, \theta)$ . Furthermore, for similar Strouhal numbers at each jet flame the hydrodynamic gain, see Section 5.3.1, and thus the interaction index  $n$  of the locally resolved  $\text{ftf}$  is assumed invariant in cross-sectional direction  $n \neq f(r, \theta)$ . The axially resolved  $\text{FTF}_x$  (Eq. 6.42) simplifies to  $\text{FTF}_x(x) = \text{ftf}(x)$ , accounting for an axially resolved gain and phase of the  $\text{ftf}$ .

Concerning the HF flame response, an axially distributed gain and phase of the  $\text{FTF}_x$  might become important as discussed in Section 5.3.1 for the considered MJC configuration depicted in Fig. 6.2. In the following, however,

the focus is put on the phase of the integral FTF. Thus, the gain is assumed to be constant over the extent of the flame. Consistent with the  $n$ - $\tau$ - $\sigma$  approach in LF thermoacoustics, a Gaussian distribution of the axial HRR density  $\xi \approx \frac{1}{\sqrt{2\pi}\sigma_{\dot{q}}} \exp\left(-\frac{1}{2}\left(\frac{x-\bar{x}_{\dot{q}}}{\sigma_{\dot{q}}}\right)^2\right)$  is applied, such that the convolution integral according to Eq. 6.37 can be solved analytically to obtain

$$\text{FTF} = n e^{-i k_{\text{conv}} \bar{x}_{\dot{q}}} e^{-\frac{1}{2}(k_{\text{conv}} \sigma_{\dot{q}})^2}. \quad (6.43)$$

Equation 6.43 is an equivalent spatial formulation of the distributed time delay model in LF thermoacoustics and assumes an acoustically axial compact flame. The FTF phase is given by the mean convective wave number and the axial "centre of gravity" of the flame  $\bar{x}_{\dot{q}}$ , where the relation  $\bar{\tau}_{\dot{q}} = \bar{x}_{\dot{q}}/\bar{u}$  yields the mean time delay  $k_{\text{conv}} \bar{x}_{\dot{q}} = \omega \bar{\tau}_{\dot{q}}$ . The product of the variance and the convective wave number yields a decreasing slope of the gain for increasing frequency, i.e. a low pass behaviour of the gain. The intuitive conclusion might thus be that the integral convective heat release fluctuations are negligible in the HF regime. However, the decreasing gain might be over-compensated by an increasing flow velocity or decreasing flame length due to the Strouhal number dependency of Eq. 6.43. The scaling of the FTF might be expressed via the Strouhal number  $\text{St} = \frac{L_{\text{FI}}}{\lambda_{\text{conv}}} = f \frac{L_{\text{FI}}}{\bar{u}}$ , obtained from the axial flame length in relation to the convective wavelength. The variance might be expressed as a fraction  $a_{\sigma} = \mathcal{O}(1)$  of the entire flame length  $\sigma_{\dot{q}} = a_{\sigma} L_{\text{FI}}$  and the convective wave number as  $k_{\text{conv}} = \frac{\omega}{\bar{u}}$ , which yields  $\text{FTF} \propto e^{-\frac{1}{2}(a_{\sigma} 2\pi \text{St})^2}$ . The Strouhal number represents the number of changes in the phase angle between zero and  $\pi$  of the HRR fluctuations in axial direction, which lead to a decreasing gain with increasing frequency. At the same frequency, but for increasing axial mean flow, the convective wave length in axial direction increases and thus the number of phase changes of the HRR within the flame length decreases and the gain increases proportional to the change in the Strouhal number. Thus, the ratio of flame length to convective wavelength, i.e. the Strouhal number, is a parameter as crucial as the cut-on frequency of the HF mode for the low pass behaviour, which operating conditions and injector design might influence via the mean flow velocity and the flame length. Consequently, short flame lengths, high convection velocities and low cut-on frequencies due to large combustor diameters might overcompensate the low pass behaviour of the

flame response at higher frequencies, leading to HF combustion instabilities.

## 7 Validation of the Transfer Matrices

The non-reactive acoustic transfer matrices are validated by the results of a generic acoustic experiment and verified by the equivalent numerical Helmholtz model in this section.

### 7.1 Generic Experimental Setup

The derived transfer matrices are validated by the generic non-reactive forced response injector-coupling experiment shown in Fig. 7.1. The geometrical parameters of the generic setup are provided in Tab. 7.1. Two tubes of diameter

**Table 7.1:** Geometry of the generic experiment in [mm]

$d_T$	$r_T$	$d_C$	$L_T$	$L_C$
20	46	158	202.2	187

$d_T$  and length  $L_T$  are coupled to a chamber of diameter  $d_C$  and length  $L_C$  at the radial displacement of the tubes  $r_T$  relative to the chamber centre. The first transverse mode is forced upstream of the tubes and subsequently downstream of the chamber to obtain a set of two frequency sweeps for the transfer matrix reconstruction according to Chapter 4.2. The acoustic pressure and axial velocity fields are measured at three axial positions in the tube and the chamber. Additionally, two pressure sensors  $C_4$  and  $C_5$  at the same axial position as sensor  $C_1$  reveal the transverse mode shape and the spin ratio of the T1 mode. Similar to the transfer matrix reconstruction of the experimental results, the numerical transfer matrices are reconstructed from an equivalent numerical forced response study of the generic setup employing the weak formulation of the Helmholtz equation according to Section 4.3.

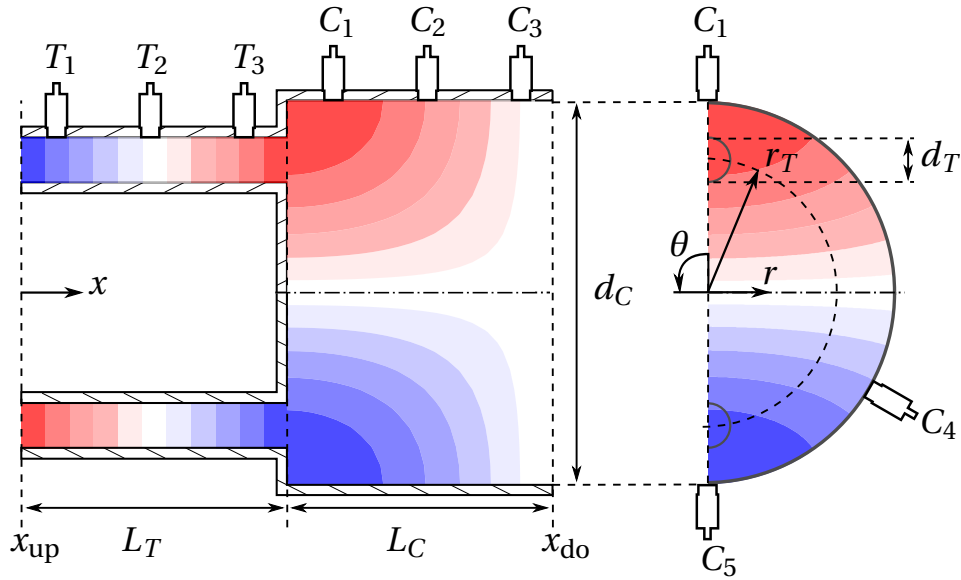


**Figure 7.1:** Generic injector coupling experimental setup to validate the acoustic transfer matrices with a forced response of the T1 mode with upstream and downstream forcing and pressure sensors at positions  $T_1 - T_3$  in the tube and  $C_1 - C_5$  in the cylindrical chamber.

## 7.2 Global and Area Change Transfer Matrix

The LF wave propagation in the tube  $\text{TM}_{pu,T} = \text{TM}_{pu,D}(L_T, \alpha_{mn} = 0)$ , the area change  $\text{TM}_{pu,A}$  and the HF wave propagation in the chamber  $\text{TM}_{pu,C} = \text{TM}_{pu,D}(L_C, \alpha_{mn} = 1.841)$ , see Secs. 6.2 and 6.4, yield the transfer matrix from up- to downstream of the generic experiment

$$\text{TM}_{pu} = \text{TM}_{pu,T} \text{TM}_{pu,A} \text{TM}_{pu,C}. \quad (7.1)$$

The transfer matrix  $\text{TM}_{pu}$  coupling the modal acoustic pressure and axial velocity is non-dimensionalised to reveal the relative contribution of the four transfer matrix elements on the overall response. The transfer matrix defined by the non-dimensional modal acoustic pressure and axial velocity  $\hat{p}_{mn}/\bar{\rho}\bar{c}^2$  and  $\hat{u}_{mn}/\bar{c}$  respectively yields the normalisation of the transfer matrix elements  $\text{TM}_{pu,12}/\bar{\rho}\bar{c}$  and  $\text{TM}_{pu,21}\bar{\rho}\bar{c}$  by the mean density and speed of sound. The diagonal elements  $\text{TM}_{pu,11}$  and  $\text{TM}_{pu,22}$  remain unaffected by the normalisation.

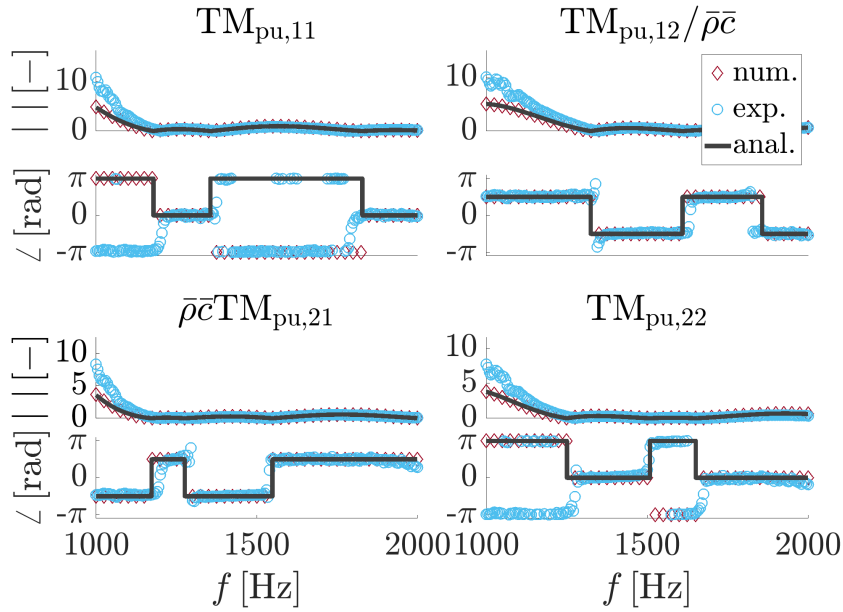


**Figure 7.2:** Validation of the analytical and numerical model of the transfer matrix  $TM_{pu}$  (Eq. 7.1) of the generic experiment Fig. 7.1 for the forced T1 mode.

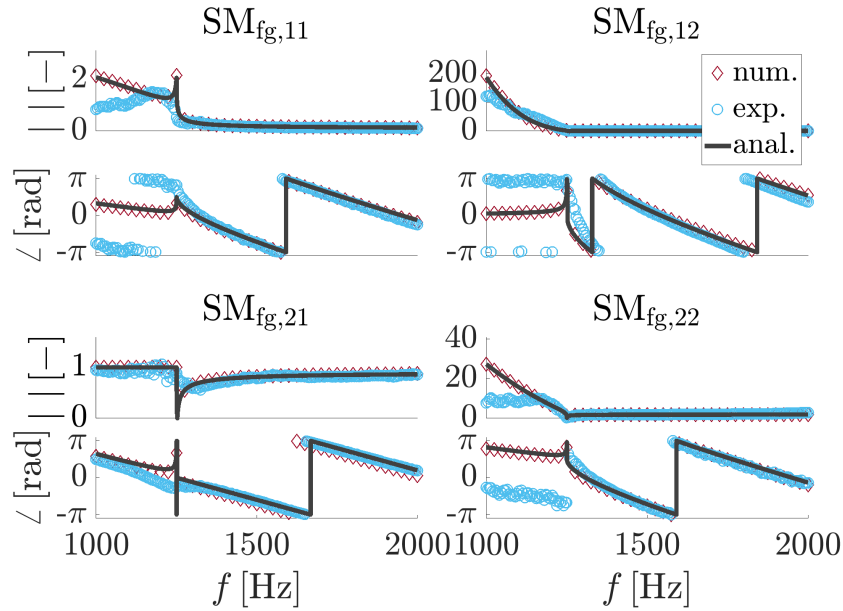


**Figure 7.3:** Validation of the analytical and numerical model of the scattering matrix  $SM_{fg}$  obtained from Eq. 6.26 with Eq. 6.6 of the generic experiment Fig. 7.1 for the forced T1 mode.

The analytical and numerical transfer and scattering matrices in Figs. 7.2 and 7.3 are in good agreement with the experimental results in the depicted frequency range 1000 – 2000 Hz around the T1 cut-on frequency at  $f_{T1} = 1250$  [Hz]. Below  $f < 0.9f_{T1}$  the experimental results of the transfer matrix amplitude and phase deviate, however, the numerical model precisely agrees with the analytical model.

Additionally, the reconstructed transfer and scattering matrix of the area change are provided in Figs. 7.4 and 7.5. The transfer matrix elements  $TM_{pu,11}$  and  $TM_{pu,22}$  of the analytical and numerical model agree perfectly. Except for the deviations below the cut-on frequency, the experiment's results agree very well. However, a slight offset to lower values than the analytical and numerical model is present. The deviation might be due to the neglect of acoustic losses in the model. The transfer matrix element  $TM_{pu,12} = -i\omega\bar{\rho}L_{\text{eff}}$  reveals a noticeable influence on the phase and thus eigenfrequencies. The transfer matrix element  $TM_{pu,21}$  is assumed to be zero in the analytical model, which is reasonable since the numerical and experimental results reveal amplitudes in the order of  $TM_{pu,21} = \mathcal{O}(10^{-4})$  for frequencies  $f > 0.9f_{T1}$ .

The corresponding scattering matrix elements  $SM_{fg,11}$  and  $SM_{fg,21}$  are in very good agreement even below  $f < 0.9f_{T1}$ , see Fig. 7.5. On the contrary, the scattering matrix elements  $SM_{12}$  and  $SM_{22}$  show deviations in the frequency range below the cut-on. Note that the injector tube transmission and reflection at the area change are represented by  $SM_{fg,11}$  and  $SM_{fg,21}$ , respectively, and the chamber transmission and reflection at the area change is represented by  $SM_{fg,22}$  and  $SM_{fg,12}$ , respectively. Thus, the deviations below the cut-on frequency are attributed to the f- and g-waves and, thus, the pressure field reconstruction in the chamber. The reason is a bad signal-to-noise ratio from the downstream forcing experiment. The T1 mode is of evanescent type below the cut-on frequency and decays exponentially from the downstream side of the chamber to the area change.

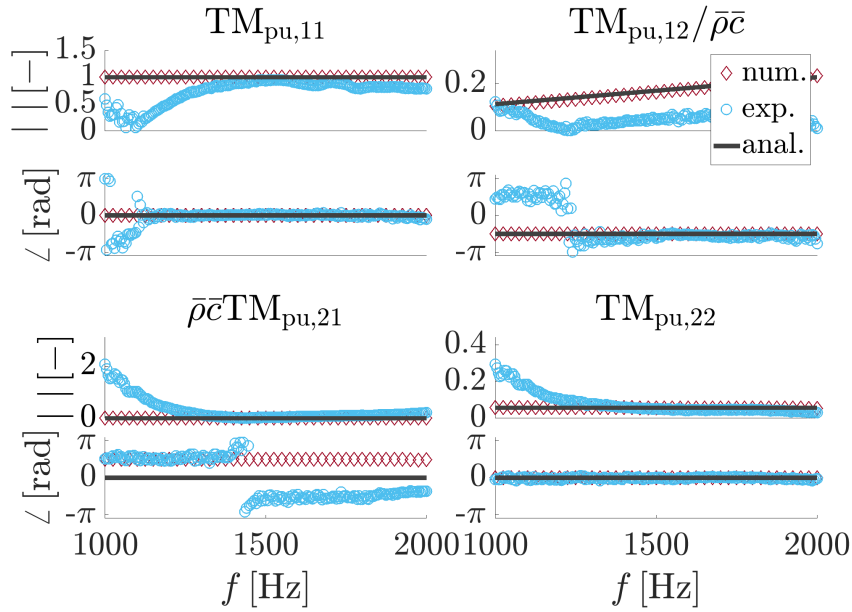


**Figure 7.4:** Validation of the analytical and numerical model of the transfer matrix  $\text{TM}_{pu,A}$  of the area change (Eq. 6.26) of the generic experiment Fig. 7.1 for the forced T1 mode.

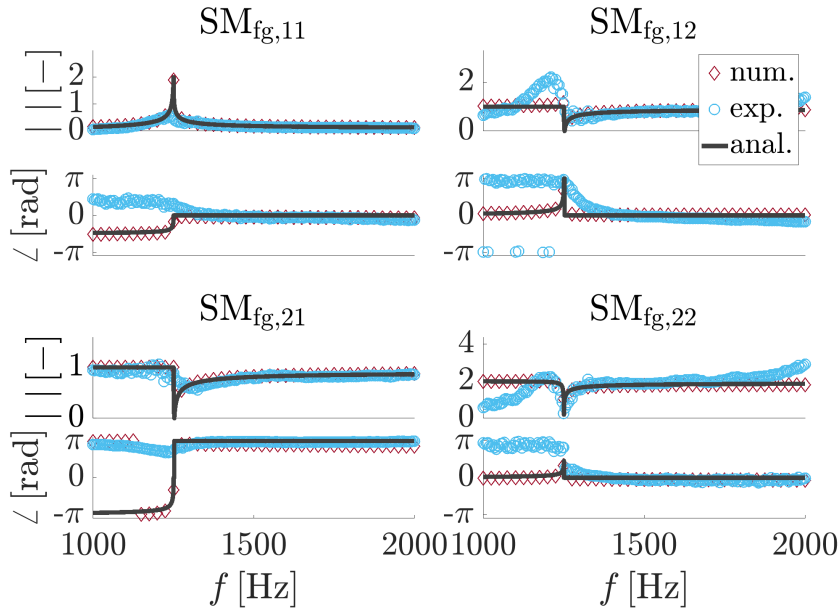


**Figure 7.5:** Validation of the analytical and numerical model of the scattering matrix  $\text{SM}_{fg,A}$  obtained from Eq. 6.26 with Eq. 6.6 of the area change of the generic experiment Fig. 7.1 for the forced T1 mode.

The scattering matrix shows two distinct regions below and above the cut-on frequency. At  $f_{T1}$  the transmission from tube to the chamber is at its maximum  $SM_{fg,11} = 2$  and the reflection is close to  $SM_{fg,21} = 0$  for the analytical and numerical model. The experimental results show lower values of  $SM_{fg,11} = 0.55$  and  $SM_{fg,21} = 0.89$ , due to losses at the area change.

# 8 Investigation of the Premixed Flame Response

This section investigates the perfectly premixed flame response by line-of-sight integrated  $\text{OH}^*$  chemiluminescence and dynamics pressure measurements. The phase-averaged images are provided for two test rig configurations, with and without a swirl-stabilised pilot burner. Different operation conditions using 100% natural gas and 100% hydrogen are provided to reveal physical insights on the driving mechanisms for HF thermoacoustic instabilities.

## 8.1 Experimental Setup With Pilot Burner

Figure 8.1 depicts the modular experimental setup used for the forced flame response experiments. The geometrical parameters of the plenum, injector tubes and combustion chamber are provided in Tab. 8.1. The nomenclature of the geometrical parameters is similar to the sketch of the MJC configuration in Fig. 1.1. The mixture of fuel and air enters the plenum of diameter  $d_p$  through a low Mach number perforated plate on the upstream side of the MJC. After the flow passed the plenum length of  $L_p$ , a mass fraction of  $Y_{\text{pilot}} = 0.1$  splits to the swirl-stabilised pilot flame, while the remaining mass fraction  $Y_{\text{jet}} = 0.9$  flows through 8 jet flame injector tubes of diameter  $d_T$  and variable length  $L_T$ . The length of the injector tubes is adjustable via a straight duct element stuck between the rounded inlet section (plenum side) and the front plate (combustion chamber side). The combustion chamber consists of a quartz glass section of the diameter  $d_{C,\text{quartz}}$  with optical access to the flames and a metallic combustion chamber of the diameter  $d_{C,\text{metallic}}$  with various ports for dynamic pressure measurements. Note that the quartz glass length of  $L_{C,\text{quartz}} = 203$

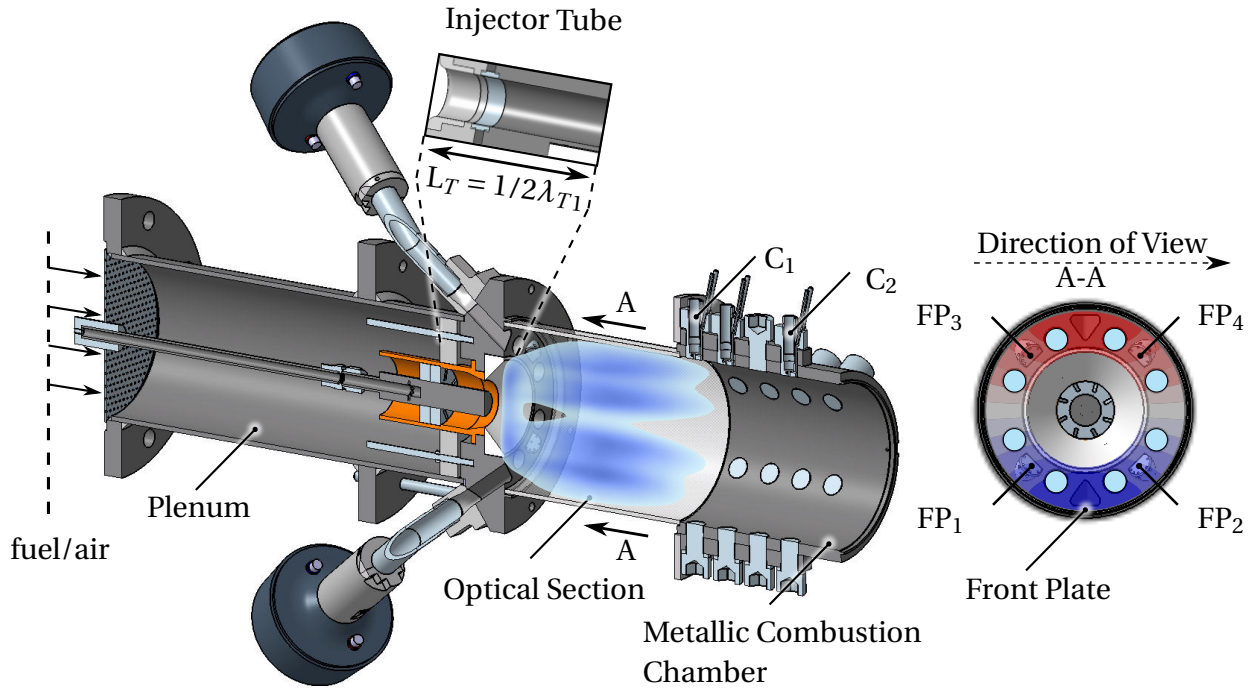


**Figure 8.1:** Experimental setup for the integrated  $\text{OH}^*$  images and simultaneous pressure measurements at the positions  $\text{FP}_1 - \text{FP}_4$ ,  $C_1 - C_2$  and  $T_1 - T_2$ .

mm given in Tab. 8.1 includes two sealings at both ends of the quartz glass chamber of 1.5 mm each. The length of the metallic combustion chamber  $L_{C,\text{metallic}}$  considers the remaining flow path to the exit of the metallic combustion chamber. After the metallic combustion chamber the burned gas enters an approximately 1.6 m long exhaust section of a similar diameter. Acoustic

**Table 8.1:** Geometry of the MJC with pilot burner in [mm]

$d_P$	$d_T$	$r_T$	$d_{C,\text{quartz}}$	$d_{C,\text{metallic}}$	$L_T \approx (1/2, 3/4)\lambda_{T1}$	$L_P$	$L_{C,\text{quartz}}$	$L_{C,\text{metallic}}$
150	18	58.5	155	158	73.5, 110.5	$453.5 - L_T$	203	187

drivers (Monacor KU-516) at the top and the bottom of the front plate are used to force the first transverse mode. The acoustic field is excited via two triangular forcing inlets, one at the top and one at the bottom of the front plate. The measurement data is acquired by two National Instruments *USB-4432* analogue input cards with four input channels for acoustic pressure measurements and one additional channel solely attributed for triggering. The front

plate provides four positions  $FP_1 - FP_4$  for acoustic pressure measurements. In the metallic combustion chamber, the sensors at the positions  $C_1$  and  $C_2$  measure the axial acoustic pressure mode shape. Piezoelectric water-cooled pressure transducers (*PCB 106B*, sensitivity  $\approx 45 \pm 1\%$  mV Pa $^{-1}$ ) are used.

The operating condition of an unburned gas temperature of  $T_u = 673$  K and an air excess ratio of  $\lambda_{CH_4} = 1.8$  with an air mass flow rate of  $\dot{m}_{air} = 120$  g s $^{-1}$  implies an injector tube bulk velocity of  $\bar{u}_T = 114.7$  ms $^{-1}$ , a thermal power of  $P_{th} = 195$  kW and an adiabatic flame temperature of  $T_b = 1880$  K. The operation condition of the experimental results presented within this section is summarised in Tab. 8.2. The design of the swirl-burner to reach The pilot massfraction of  $Y_{pilot} = 0.1$  is assured by the analytical design of the swirl-burner based on a analytical model for the pressure drop provided in Appendix A.2. Moreover, the estimation of the exhaust gas temperature by the adiabatic flame temperature is justified by a heat loss estimation including convective and radiative heat transfer in Appendix A.3.

**Table 8.2:** Operating Conditions for the MJC with Pilot Burner

fuel	$\lambda_F$ [-]	$T_u$ [K]	$T_b$ [K]	$Y_{pilot}$ [-]	$\dot{m}_{air}$ [g s $^{-1}$ ]	$\bar{u}_T$ [m s $^{-1}$ ]	$P_{th}$ [kW]
CH $_4$	1.8	673	1880	0.1	120	114.7	192

Line-of-sight integrated OH\* chemiluminescence images of the eight jet flames are recorded by a *Photron FastCam SAX-2* high-speed camera and a Hamamatsu image intensifier. The raw chemiluminescence images are cropped to the quartz glass combustion chamber using the length scales provided by a reference image. The resulting mean HRR density fluctuations for the experimental setup with pilot burner (see Fig. 8.1) is shown in Fig. 8.2. The absence of OH\* signal at the beginning of the flame is due to a small metallic step of 8 mm length at the outer radial position of the front plate, which partially hides the flames from the camera. An initial pilot-burner-dominated region of roughly 30 mm length is observed in the radially integrated HRR. The  $L_{FI} \approx 200$  mm long natural gas flames yield an axial maximum in the HRR at  $\approx 95$  mm. The jet flames show a nearly symmetric HRR distribution in axial direction, with the exception of the pilot burner region. The radial heat release

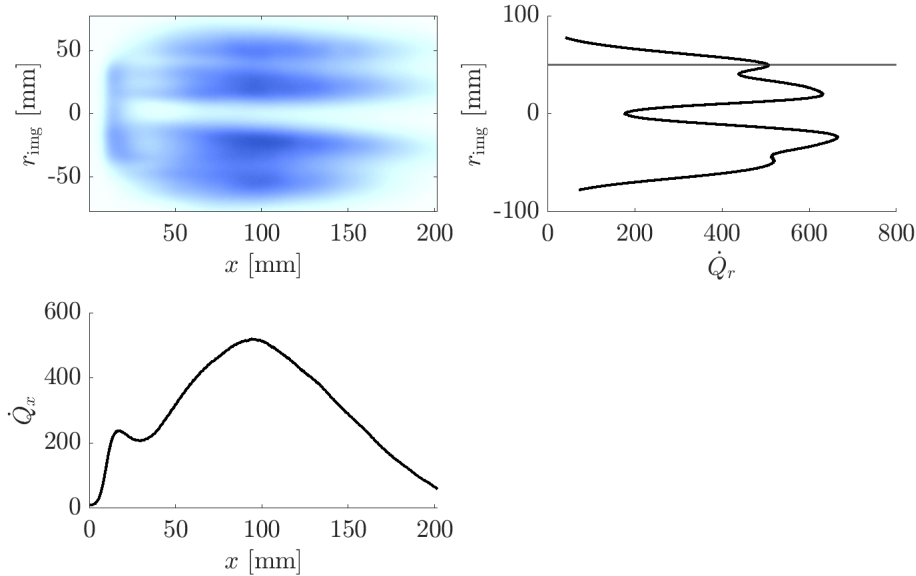


**Figure 8.2:** Line-of-sight integrated mean HRR density distribution (top-left) and the corresponding integral axial (bottom-left) and radial (top-right) distribution for the MJC without pilot burner for the conditions summarised in Tab. 8.2.

distribution of the natural gas flames indicates a clear overlap of the upper two and the lower two flames since no clear local minimum in axially integrated HRR is present.

Before the phase-locked results are presented, the differences in the acoustic response of the two designed injector tube lengths are discussed on the basis of the experimental acoustic forced response (section 8.1.1) and a non-reactive numerical Helmholtz model (section 8.1.2).

### 8.1.1 Acoustic Forced Response Study

The injector tube length is a crucial design parameter of the combustor regarding the injector-coupling of the HF thermoacoustic instability [35, 90]. The variation of the injector tube length reveals insights into different levels of axial and transversal velocity fluctuations at the injector tube exit to the overall flame response. Two cases are referred to in the following. The case of

1. an acoustic pressure anti-node coupling ( $L_T = 3/4\lambda_{T1}$ ) and
2. an acoustic pressure node coupling ( $L_T = n \cdot 1/2\lambda_{T1}$  with  $n = 1, 2$ )

at the dump plane designed with the estimated cut-on frequency of the T1 mode  $\lambda_{T1} = \frac{c_b}{f_{T1}}$  for a constant preheat temperature of  $T_u = 673$  K and a flame temperature in the range of  $T_b = 1800 - 2100$  K. Ideally, the pressure node coupling case is dominated by axial acoustic velocity and the pressure anti-node coupling, on the contrary, yields low axial acoustic velocity fluctuations at the dump plane. The experimental forced response study discussed in this section validates the distinct acoustic behaviour of the two injector tube lengths for pressure anti-node and pressure node coupling at the injector tube exit. An equivalent numerical model reveals detailed insights into the acoustic injector coupling of the two cases to verify the injector tube design.

The forced response for both injector tube lengths is shown in Figs. 8.3 and 8.4. The forced response phase difference of the sensors in the front plate is given relative to the fourth sensor  $FP_4$  on the top right side of the front plate. The sensor  $FP_3$  is in-phase due to the position on the top left side, and the two sensors  $FP_1$  and  $FP_2$  show a phase difference of  $\pi$  indicating a standing T1 mode in transverse direction. The pressure sensors in the metallic chamber  $C_1$  and  $C_2$  show approximately the same amplitudes at the T1 peak for pressure anti-node coupling. Consequently, the T1 mode extends into the metallic combustion chamber and the 1.6 m long exhaust section. The phase difference of zero between the sensors  $C_1$  and  $C_2$  at the T1 eigenfrequency indicates the axial wave number of approximately zero. Previous publications on swirl flames and rocket engines show a substantial attenuation of the T1 mode towards the downstream side.

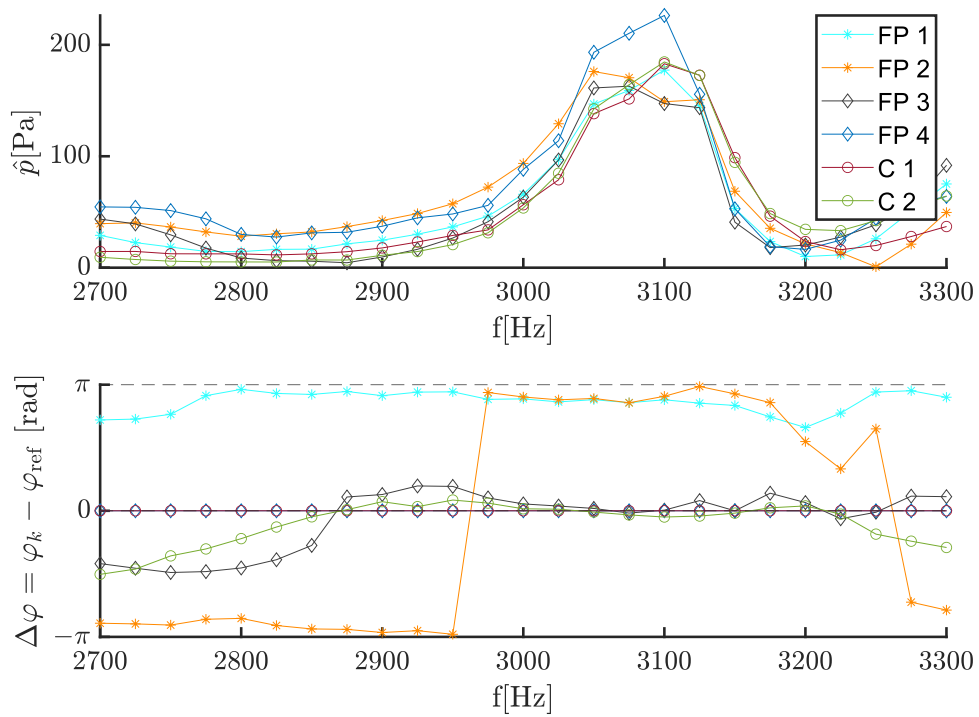


**Figure 8.3:** Experimental forced response of the MJC for pressure anti-node coupling.

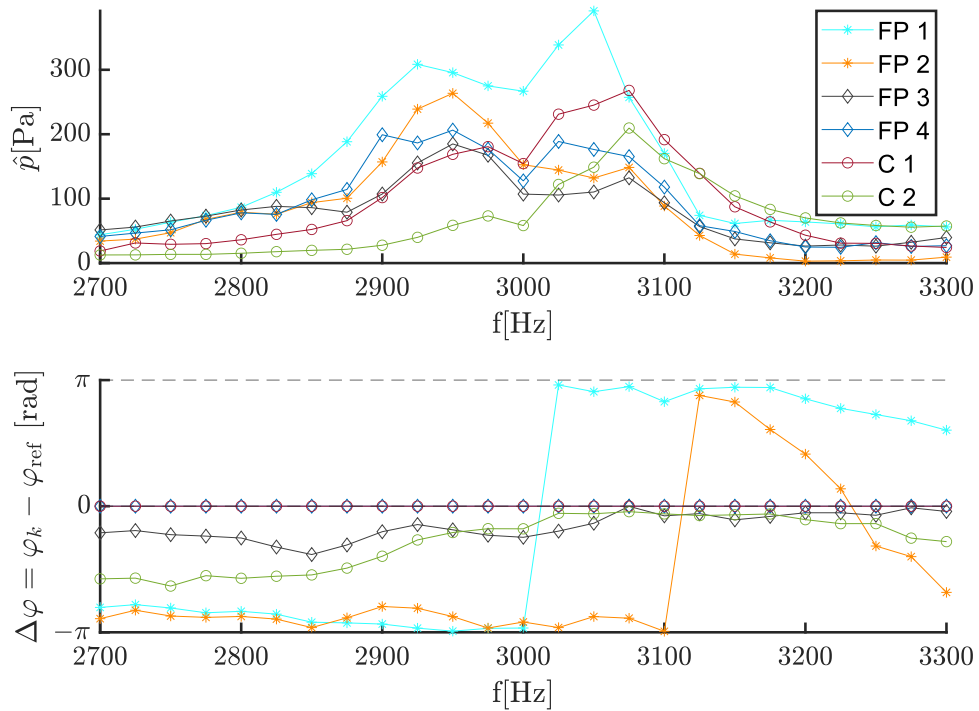


**Figure 8.4:** Experimental forced response of the MJC for pressure node coupling.

The increase in cross-sectional mean temperature in the combustion chamber yields a thermal cut-off and, thus, an evanescent mode. However, the forced response of the pressure anti-node coupled case reveals no attenuation in the acoustic pressure towards the downstream side. The cross-sectionally averaged temperature gradient is too small in the investigated configuration. A clear difference in the forced response of the two injector tube lengths is an additional peak at  $f_{T1} = 2925 - 2950$  Hz for the acoustic pressure node coupled injector tube, see Fig. 8.4. Note that this frequency is below the T1 cut-on, and consequently, an evanescent, axially decaying T1 mode is observed. The decreasing amplitudes in the axial direction of the pressure sensors  $C_1$  and  $C_2$  confirm the evanescent type of the mode at  $f_{T1} = 2925 - 2950$  Hz. However, no such mode is found in the case of the quarter wavelength injector tubes. The cross-sectionally standing T1 mode shape is crucial for the upcoming optical  $OH^*$  results since the  $OH^*$  intensities in the images as shown in Fig. 8.2 originate from two line-of-sight integrated jet flames. Therefore, a crucial assumption is the standing transverse T1 mode shape, which is indicated by the phase shift of  $\pi$  between the top and the bottom sensors in the front plate in the forced response for variable frequency. However, a more detailed analysis of the transverse mode shape for the investigated phase-locked  $OH^*$  images is provided to ensure a similar phase of the acoustic injector coupling at each of the two line-of-sight integrated flames. The angle of the nodal line  $\theta_m$  and the spin ratio  $SR$  are calculated as described in Section 4.2 with the data of the simultaneous pressure measurements used for the phase averaged images for both investigated injector tube lengths. Fig. 8.5 depicts the angle of the nodal line relative to the forcing inlets and the spin ratio for both injector tube lengths. The pressure anti-node coupling and the pressure node coupling yield a nodal line angle close to the dashed line in Fig. 8.5 corresponding to  $\theta_m = \pi/2 = 90^\circ$  relative to the vertical axis. The spin ratio is close to the dashed line of  $SR = 0$ . The spin ratio and the nodal line position confirm the required standing T1 mode shape for both cases due to counter-phase forcing. Thus, the coherent response of the line-of-sight integrated  $OH^*$  chemiluminescence is assured for the optical results of the HRR fluctuations in the following.

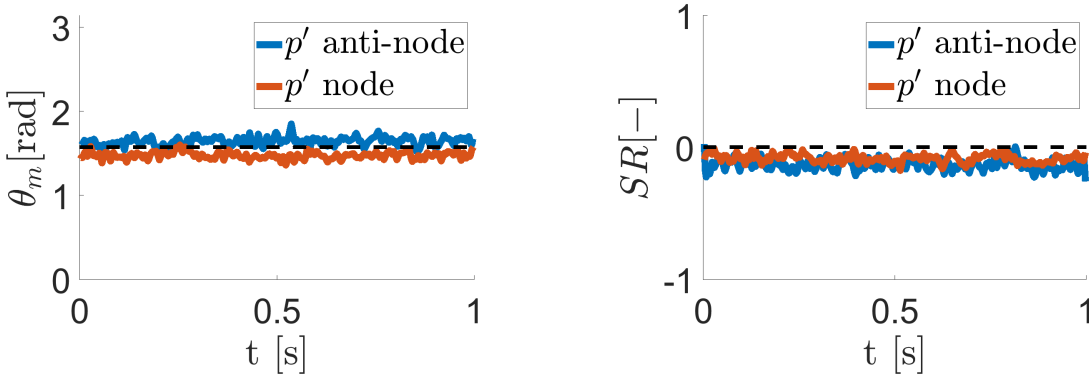


**Figure 8.5:** Experimental results for the nodal line (left) and the spin ratio (right) for pressure anti-node coupling and pressure node coupling at  $f = 3100$  Hz with zero angles at the triangular forcing inlet at the top.

### 8.1.2 Numerical Helmholtz Model

The numerical Helmholtz model covers the entire geometry of the test rig, see Fig. 8.6 [91], in order to verify the acoustic design and to reveal the differences in injector coupling of the different injector tube lengths. The weak formulation of the Helmholtz equation is solved numerically within the hybrid CFD/CAA framework, see Section 4.3. The mean speed of sound is es-

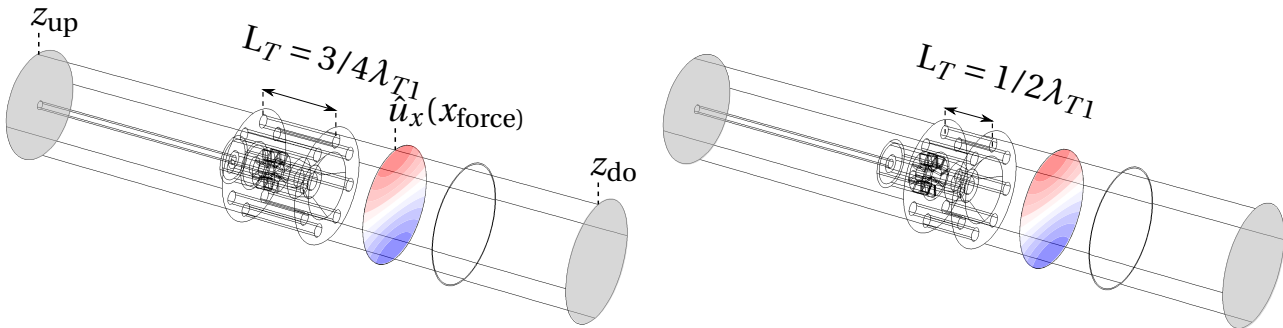


**Figure 8.6:** Numerical setup for pressure anti-node coupling (top) and pressure node coupling (bottom) with the forced axial acoustic velocity at  $x_{\text{force}} = 0.25 L_C$  and impedance boundary conditions according to Tab. 8.3.

timated from the preheat temperature  $T_u = 673$  K and the adiabatic flame

temperature at  $T_b = 1880$  K, which yields  $c_u = 517$  ms<sup>-1</sup> and  $c_b = 840$  ms<sup>-1</sup>, for the unburned and burned gas, respectively. Note that the axial extent of the unburned core region of the flame is simplified by a cross-sectional area-averaged speed of sound  $c_{b,av} = 804$  ms<sup>-1</sup>. The low Mach number of the perforated plate at the upstream side of the plenum yields an impedance boundary condition of  $z_{up} \approx 2$  [16]. The downstream impedance is set to  $z_{do} = 100$ , which corresponds to the reflective boundary condition measured in the experimental forced response. The reflection coefficient in the azimuthal direction is set constant  $R_\theta = 1$  corresponding to a spin ratio of  $SR = 0$ , see Section 3.4, representing the standing T1 mode shape of the experiment. The boundary conditions are summarised in Tab. 8.3. Similar to the experiment, a forced response study is carried out. The forcing is applied via an internal flux in axial acoustic velocity  $u'_x$  at the position  $x_{force}$ .

**Table 8.3:** Numerical Domain and Boundary conditions

$z_{up}$ [-]	$z_{do}$ [-]	$c_u$ [ms <sup>-1</sup> ]	$c_b$ [ms <sup>-1</sup> ]	$c_{b,av}$ [ms <sup>-1</sup> ]
2	100	517	840	804

The computed mode shapes at the peak frequencies of the numerical forced response analysis are provided in Fig. 8.7 [91]. Contrary to the pressure anti-node coupling case, the injector tube length  $L_T = 1/2\lambda_{T1}$  reveals two peaks around the cut-on frequency shifted to slightly lower and higher frequencies. The distinct differences in the acoustic pressure modes between the case with a pressure node and anti-node coupling at the dump plane are explained by the analytical acoustic area jump condition according to Eq. 6.24. The pressure anti-node coupled case at the injector tube exit in combination with the high axial acoustic wave number of the T1 mode yields an integral acoustic energy flux coupling condition close to zero  $(\hat{p}\hat{u}A)_{mn} = 0$  since the gradient in acoustic pressure and thus the modal axial acoustic velocity at the T1 mode is very low. Thus, the case of a pressure anti-node at the injector tube exit couples predominantly via the constant acoustic pressure  $\hat{p} = \text{const.}$  condition across the area change and perfectly supports the axial T1 mode shape at the cut-on frequency. Contrary, the acoustic pressure coupling condition for the pressure anti-node coupled case is close to zero  $\hat{p} = 0$  due to the axial

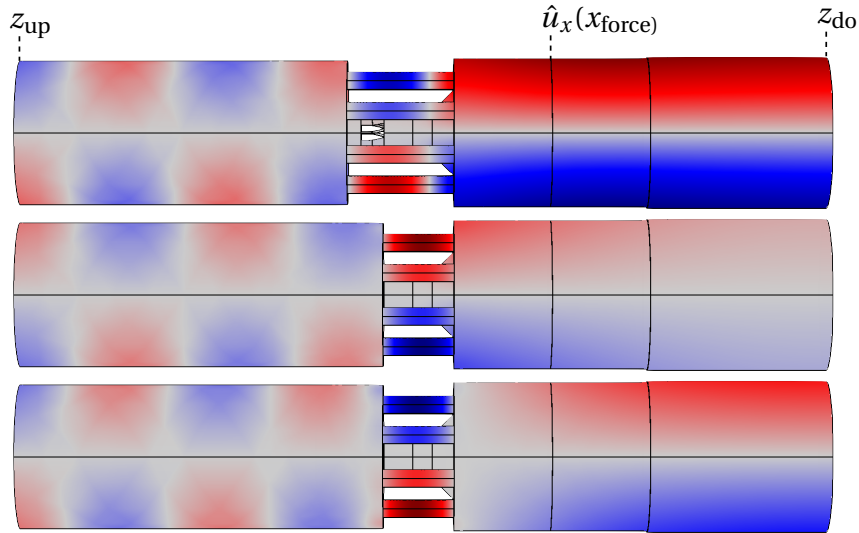


**Figure 8.7:** Numerical results of the acoustic pressure mode shapes at the peak frequencies of the forced response simulation with pressure anti-node coupling ( $L_T = 3/4\lambda_{T1}$ ) at  $f = 3110$  Hz (top) and with pressure node coupling ( $L_T = 1/2\lambda_{T1}$ ) at  $f = 3020$  Hz (middle) and at  $f = 3150$  Hz (bottom) with the boundary conditions according to Tab. 8.3.

acoustic pressure node. Precisely at the T1 cut-on the frequency, the acoustic energy flux coupling condition is also close to zero  $(\hat{p}\hat{u}A)_{mn} = 0$  due to the infinite axial wavelength. Thus, the entire response is damped at the T1 cut-on frequency, which explains the local minimum of the experimental forced response between the two peaks. In order to reach resonance with a pressure anti-node coupled injector tube, a non-zero acoustic energy flux condition is required and thus axial pressure gradients at the area change are required  $(\hat{p}\hat{u}A)_{mn} = \text{const}$ . Thus, the first resonant T1 eigenmode is shifted towards lower frequencies of evanescent type, i.e. with a longitudinal exponential decay of the pressure mode. The shift of the HF eigenmodes dependent on the injector tube length is demonstrated in more detail by Rosenkranz et al. [90].

The effect of a shift in the T1 resonance peak due to injector-tube coupling effects the possible instabile thermoacoustic modes as indicated by the experimental results of Philo et al. [35] of a self-sustained first transverse mode in a rectangular MJC combustor. Different coupling conditions at the dump plane due to non-compact injector tube acoustics yields two competing self-

sustained transverse eigenmodes observed for the pressure node-coupled case at the injector tube exit. Moreover, the split of the T1 mode into two separate eigenmodes occurs in the design of quarter-wavelength dampers for rocket combustion chambers [5].

Note, however, that the ideal coupling conditions  $u' = 0$  and  $p' = 0$  are not reached for the two injector tube lengths  $L_T = 3/4\lambda_{T1}$  and  $L_T = 1/2\lambda_{T1}$  respectively. However, the two injector tube lengths show distinct differences in their acoustic response close to the desired pressure anti-node and node coupling as shown in the forced response study. The axial acoustic velocity at the in-

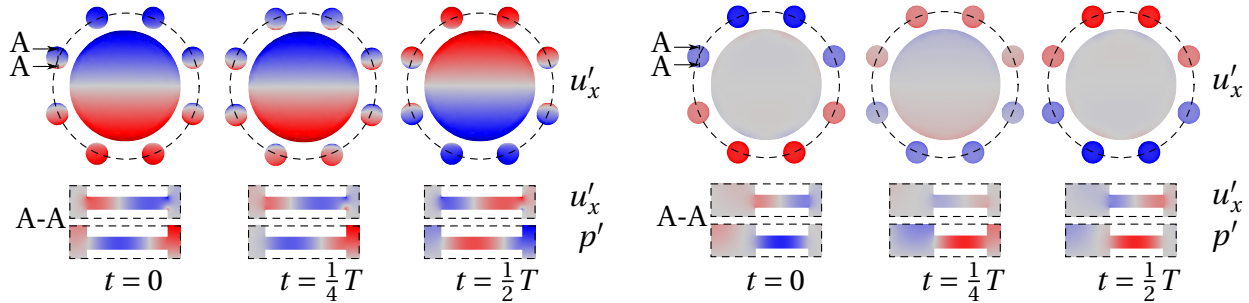


**Figure 8.8:** Numerical results of the normalised axial acoustic velocity at the exit of the injector tube three times during the period  $T = 1/f$  for the two cases with pressure anti-node coupling ( $L_T = 3/4\lambda_{T1}$ ) at  $f = 3110$  Hz (left) and with pressure node coupling ( $L_T = 1/2\lambda_{T1}$ ) at  $f = 3150$  Hz (right).

jector tube exit shown in Fig. 8.8 emphasises the dominating axial acoustic velocity at the injector tube exit for the pressure node coupled case, which shows a constant phase over the injector tube cross-section. Due to the transverse mode shape, the axial acoustic velocity of the upper and lower two injector tubes is higher than the injector tubes in the centre. Thus, concerning the convective flame response of the jet flames of this configuration, an axial HRR pattern with a constant phase over the cross-section of the jet flame is expected. In contrast, the pressure anti-node coupled case shows a phase shift of  $\pi$  over the cross-section, which is caused by a transverse to longitudinal velocity coupling. The longitudinal mode propagation in the injector tube yields a pressure anti-node condition at the injector tube exit, as shown in Fig. 8.7 and therefore the axial acoustic velocity at the injector tube exit is small in relation

to the transverse velocity. Since the injector tube diameter is non-compact compared to the transverse mode near field, a transverse acoustic pressure gradient is present at the exit of the injector tube. The transverse acoustic velocity follows the contour of the injector tube and thus couples to the axial direction. Therefore, the phase shift is more pronounced at the centred injector tubes, and the expected flame response due to convective vortex shedding of the jet flames yields an axial HRR pattern with a phase shift of  $\pi$  over the cross-section of the jet flame.

### 8.1.3 Flame Response - Pressure Anti-Node and Pressure-Node Coupling

The results of the phase-locked images for the two injector tube lengths are shown in Fig. 8.9 by means of the phase-locked HRR density  $\dot{q}(\varphi)$  according to Eq. 4.2 including the 25, 50 and 75% iso-contour of  $\dot{q}(\varphi)$ . The phase in the temporal oscillation  $\varphi$  is given by the mean phase angle of the time bin of the phase-locked image, see Section 4.1, relative to the phase of the acoustic pressure sensor  $C_1$ . The HRR density fluctuations  $\dot{q}'$  are normalised by the maximum of  $\dot{q}(\varphi)$  i.e.  $\dot{q}_{\max}$  and by the mean  $\bar{\dot{q}}$  according to Eqs. 4.4 and 4.5 and are depicted in the middle and the bottom of Fig. 8.9. The  $\dot{q}(\varphi)$  iso-contours at 25, 50 and 75 % are shown in all plots for convenience.

On the one hand, the flame response of both investigated injector tube configurations share several similarities. The beginning of the flame is influenced by the central swirl-stabilised pilot burner, which yields a higher intensity at the jet flame shear layers pointing to the combustor centre. The phase-locked HRR fluctuations  $\dot{q}'(\varphi) = \dot{q}(\varphi) - \bar{\dot{q}}$  in the middle of Fig. 8.16 reveal coherent consumption rate fluctuations as the dominant local flame response. The top and the bottom half of the image reveal a symmetry in amplitude with an opposed sign, in accordance with the standing T1 mode, i.e. the spin ratio of zero and the nodal line of the forced response depicted in Fig. 8.5. The highest HRR amplitudes align with the maximum in mean heat release at  $x_C \approx 95$  mm. The normalised HRR fluctuations  $\dot{q}'(\varphi)/\bar{\dot{q}}$  at the bottom of Fig. 8.16 reveal the scaling of the HRR fluctuations with the mean heat release field. An attenuation of the normalised HRR fluctuations in the axial direction due to turbulent

and molecular diffusion can hardly be observed. The amplitude of the normalised fluctuations is approximately preserved for both cases. The phase of the convective HRR density fluctuations increases in axial direction due to the transport with the mean flow field, which yields multiple phase changes in the HRR density fluctuations. The change in sign of the  $\dot{q}'_{\pm}$  patches corresponds to half a period in the oscillation. Therefore, an increased distance between the nodal lines  $\dot{q}' = 0$  is attributed to an acceleration of the mean flow. Thus, the distance of the HRR fluctuation nodal lines in axial direction  $\dot{q}(x)' = 0$  corresponds to half of the convective wavelength. The axial vortex length scale  $\lambda_{\text{vort}} = \frac{1}{2} \frac{\bar{u}}{f}$  might be estimated by the ratio the mean convection velocity in the injector tubes  $\bar{u} \approx \bar{u}_T$  and the forcing frequency  $f$ . The estimated mean flow velocity in the injector tubes yields an axial vortex length scale of one injector tube diameter  $\lambda_{\text{vort}} \approx 18$  mm, which is consistent with the depicted flame response.

On the other hand, the flame response of the two injector tube lengths shows distinct differences. The phase of the HRR fluctuations in radial direction of the top and the bottom half of the images reveals insights on the contribution of the longitudinal and the transverse acoustic field. HRR density fluctuations with zero phase shift in cross-sectional direction originate from the purely longitudinal acoustic pressure field in the injector tube. This is observed on the right side of Fig. 8.9 with pressure node coupling in the radially outer flames and in line with the numerical reconstruction of the acoustic velocity field in Fig. 8.8. Contrary, for the case with pressure anti-node coupling on the left side of Fig. 8.9, the HRR fluctuations reveal a phase shift of  $\pi$  in radial direction within one half of the image, which reveals a modulation due to the transverse pressure field. In accordance with the numerical results of the pressure anti-node coupled case, the flame response shows counter-phase oscillations of the single flames in cross-sectional direction. This effect is stronger for the inner flames close to the radial centre of the chamber, due to the increase transverse acoustic pressure gradient in comparison to the outer flames.

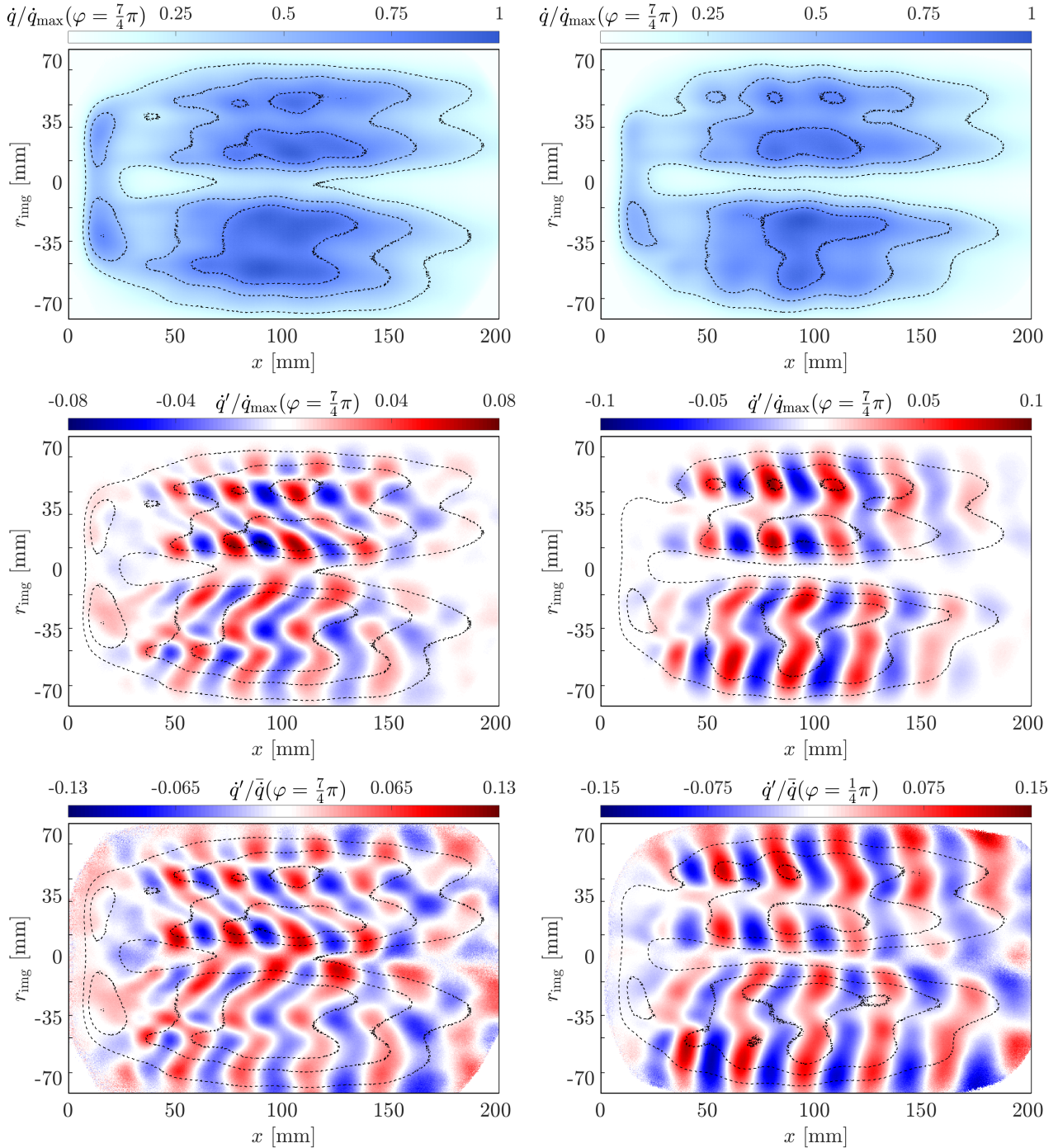


**Figure 8.9:** Phase-locked HRR  $\dot{q}(\varphi)$  (top), fluctuations  $\dot{q}'(\varphi)$  (middle) and normalised HRR fluctuations  $\dot{q}'(\varphi)/\bar{q}$  (bottom) with pressure anti-node coupling (left) and with pressure node coupling (right) for natural gas (Tab. 8.2) at 3100 Hz.

The axial sequence of the HRR patches  $\dot{q}'_{\pm}$  yields a high degree of compensation of the integral flame response  $\int \dot{q}'_{\pm} dx$ . The additional phase shift in radial direction results in an increased compensation of the local HRR patches  $\dot{q}'_{\pm}$  in radial direction, which yields a lower contribution of the convective driving mechanism to the overall flame response. The contribution of the local, instantaneous flame compression and displacement mechanisms are not directly observable from the optical results. For a more detailed analysis, the cross-sectionally weighted integral HRR fluctuations according to Eq. 6.35 might be considered accounting for the convolution of the local HRR fluctuations with the local amplitude and phase of  $J_0 P_1 = |J_0| |P_1| e^{i\angle(J_0 P_1)}$ , see Section 6.6. However, for simplicity, the amplitude dependency is neglected  $|J_0| |P_1| = 1$ . Thus, the cross-sectionally phase-aligned integral HRR fluctuations  $\hat{Q}'_{10,x} \approx \int_A e^{i\angle(J_0 P_1)} \hat{q}' dA$  are considered, which accounts for the sign of the acoustic pressure amplitude. Therefore, the real-valued axially resolved HRR density fluctuations yield

$$\dot{Q}'_x = \int_0^{R_C} \dot{q}' dr - \int_0^{-R_C} \dot{q}' dr \quad (8.1)$$

$$\bar{Q}_x = \int_{-R_C}^{R_C} \bar{q} dr \quad (8.2)$$

accounting for the phase shift of  $\pi$  between the top and bottom half. The cross-sectional integration yields the axially distributed flame response, which reveals further insights into the driving potential and the driving mechanisms for the two cases of acoustic pressure anti-node and node coupling. The radially integrated HRR fluctuations  $\dot{Q}'_x$  as well as the normalised fluctuations by the mean HRR  $\dot{Q}'_x / \bar{Q}_x$  for both injector tube lengths are shown in Fig. 8.10. Three characteristic phases in the oscillation, namely with maximum ( $\varphi = 0$ ), zero ( $\varphi = 1/2\pi$ ) and minimum ( $\varphi = \pi$ ) acoustic pressure amplitude according to the pressure sensor C<sub>1</sub> are depicted. The results for the case with acoustic pressure anti-node coupling on the left side show four times lower cross-sectional integrated HRR fluctuations (mind the scale of the vertical axis), which is due to the phase shift of  $\pi$  of the local heat release patches  $\dot{q}'_{\pm}$  between the lower and upper part of the shear layer in each flame.

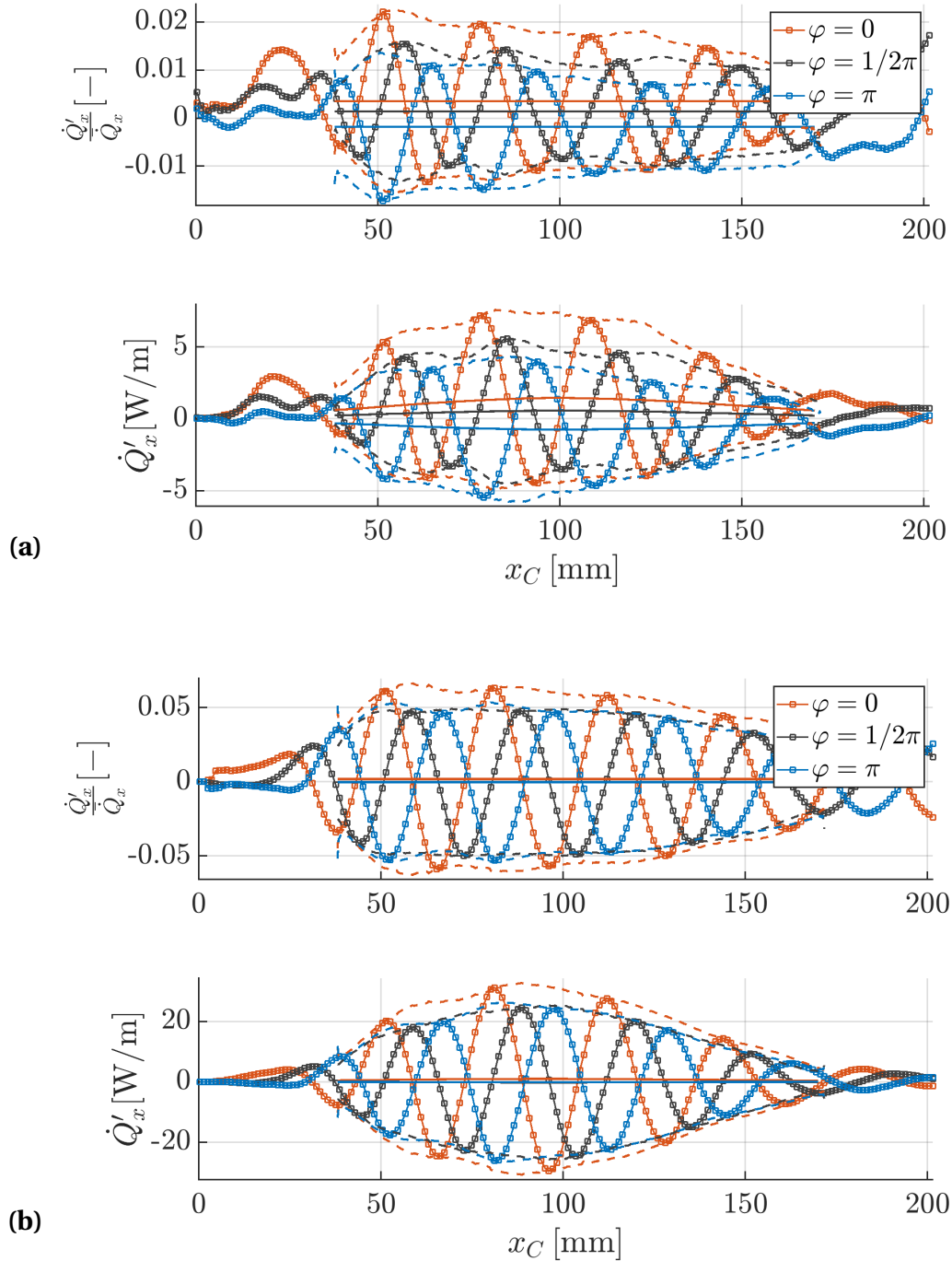


**Figure 8.10:** Axially resolved HRR fluctuations  $\dot{Q}'_x$  (bottom,  $\square$ ), normalised fluctuations  $\dot{Q}'_x/\bar{Q}_x$  (top,  $\square$ ), their respective offset (—) and envelopes (—) for pressure anti-node coupling **(a)** and pressure node coupling **(b)** with maximum, zero and minimum acoustic pressure amplitude at  $\varphi = 0, 1/2\pi, \pi$ , respectively.

This effect yields high compensation as long as the upper and lower reactive shear layer modulation propagates at the same velocity. Especially for the case on the left-hand side with acoustic pressure anti-node coupling, a positive and negative offset of  $\dot{Q}'_x(\varphi = 0)$  and  $\dot{Q}'_x(\varphi = \pi)$ , respectively, are observed. The root cause of this offset in normalised radially integrated HRR fluctuations are coupling mechanisms, which are directly proportional to the instantaneous, local acoustic pressure and velocity field, such as flame displacement and flame compression. This offset in cross-sectional integrated HRR fluctuation is quantified by the mean of the upper and lower envelopes  $E_{\text{up}}$  and  $E_{\text{low}}$ , respectively, of the normalised fluctuations

$$\frac{\dot{Q}'_{x,\text{off}}}{\bar{\dot{Q}}_x} = \frac{1}{2} \left( E_{\text{up}} \left( \frac{\dot{Q}'_x}{\bar{\dot{Q}}_x} \right) + E_{\text{low}} \left( \frac{\dot{Q}'_x}{\bar{\dot{Q}}_x} \right) \right). \quad (8.3)$$

The analytical envelope function of Matlab estimates the envelopes of the heat release signal. The minimum peak distance is defined via the vortex length scale  $\lambda_{\text{vort}} = \frac{1}{2} \frac{\bar{u}_T}{f}$ . In order to obtain the solely jet flame dynamics, the axial limits of the envelope estimation are set to  $45 < x_C < 175$  mm in both cases. Since the signal coherence diminishes at the tip of the flame for the case with pressure anti-node coupling, this region is omitted for the offset calculation in both cases for similarity in the evaluation.

In the next step, the global Rayleigh integral is used to quantify the driving potential. The quantification of the Rayleigh integral from an estimated local Rayleigh index is provided in a previous publication [92]. However, the estimated local Rayleigh index is only an indirect experimental measure since additional assumptions and post-processing are required to estimate the pressure mode shape. Therefore, a simplified form of the Rayleigh integral

$$\text{RI}_{\text{jet}} = p'_{C_1} \dot{Q}'_{\text{jet}} \quad (8.4)$$

is calculated with the acoustic pressure  $p'_{C_1}$  at the sensor position  $C_1$  and the globally integrated HRR fluctuations in the jet-flame-dominated region

$$\dot{Q}'_{\text{jet}} = \int_{x_{\text{pilot}}}^{L_C} \dot{Q}'_x dx = \int_{x_{\text{pilot}}}^{L_C} \left( \int_0^{R_C} \dot{q}' dr - \int_0^{-R_C} \dot{q}' dr \right) dx \quad (8.5)$$

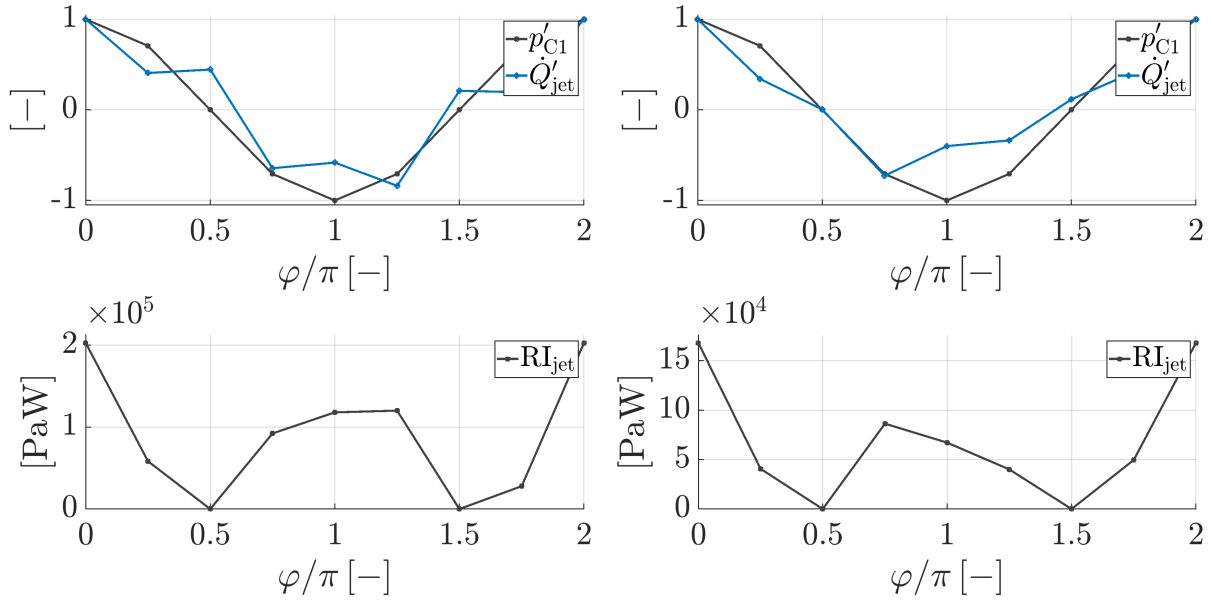


**Figure 8.11:** Integrated HRR fluctuations (top) and Rayleigh integral (bottom) with pressure anti-node coupling (left) and with pressure node coupling (right) over the phase-averaged period of the oscillation.

is chosen to obtain a direct experimental measure of the driving potential. The Rayleigh integral according to Eq. 8.4 is obviously only a qualitative measure since the local weighting of the HRR with the local pressure amplitude is omitted. However, the phase  $\angle(p'_{C1})$  in the upper and lower half of the phase-locked images is constant due to the standing mode shape, and thus, the phase relation of acoustic pressure and heat release is adequately captured by the simplified Rayleigh integral.

The results in Fig. 8.11 show an in-phase oscillation of acoustic pressure and integral HRR for both injector tube lengths. The Rayleigh integral is positive over the entire period, which yields a possible driving behaviour of HF instability. The differentiation between the convective and the local instantaneous driving mechanisms requires further investigation. Therefore, the total HRR fluctuations might be separated into

$$\dot{Q}'_x = \dot{Q}'_{x,\text{conv}} + \dot{Q}'_{x,\text{off}} \quad (8.6)$$

in order to distinguish the relative contributions of the local unsteady HRR fluctuations and the convective HRR fluctuations due to coherent vortex

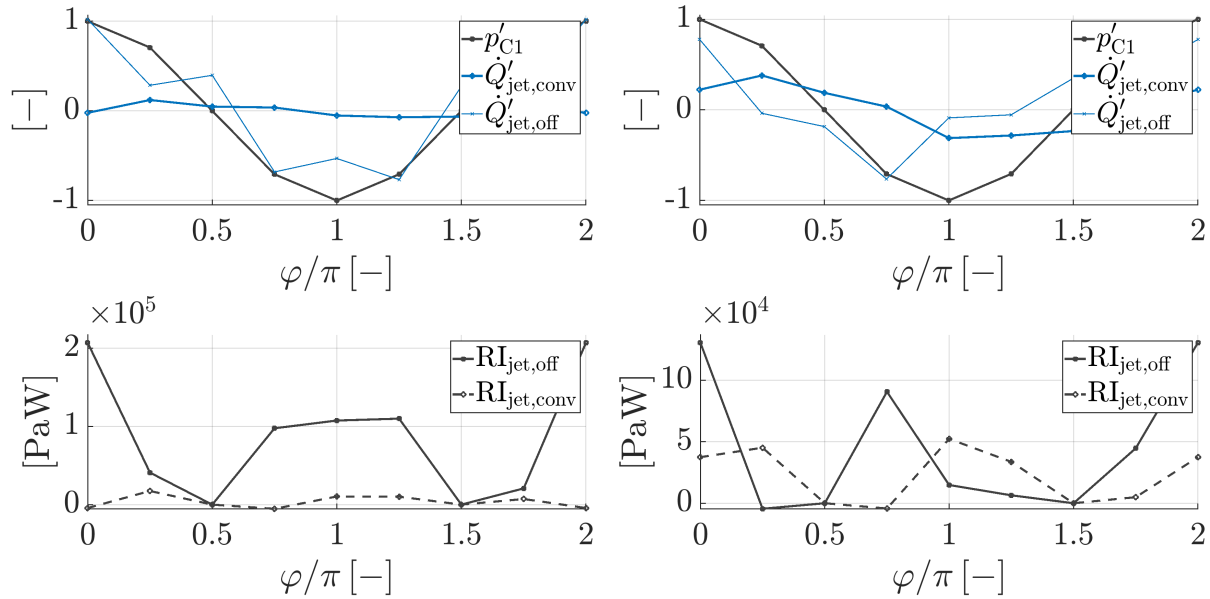


**Figure 8.12:** Integrated HRR fluctuations (top) and Rayleigh integral (bottom) separated into convective and offset contribution with pressure anti-node coupling (left) and with pressure node coupling (right) over the phase-averaged period of the oscillation.

shedding. Consequently, the convective contribution is obtained by subtraction of the offset from the overall HRR fluctuations. The results shown in Fig. 8.12 reveal a dominating contribution of the offset in HRR fluctuations  $\dot{Q}'_{x,off}$  due to the instantaneous flame response in phase with the pressure oscillations. The contribution of the convective consumption rate fluctuations is generally lower in both cases due to the high degree of compensation in the convective HRR  $\dot{Q}'_{x,conv}$  in the axial integration. Additionally, the radial phase shift of  $\pi$  between the upper and lower shear layer of each flame in the anti-node coupled case yields an even lower contribution of the convective consumption rate fluctuations in the pressure anti-node coupled case. The instantaneous flame response dominates the pressure anti-node coupled case, and the convective driving mechanism is of minor importance. Note that this cannot be observed from the local flame response plots in Fig. 8.9 since the high local amplitudes of the consumption rate fluctuations hide the low amplitudes of the instantaneous flame response mechanisms. This explains the in-phase fluctuation of the overall HRR fluctuations in Fig. 8.11 since the con-

tribution with the larger amplitude typically dominates the phase for both cases. Nonetheless, the acoustic pressure anti-node coupled case indicates a noticeable contribution of the convective flame response. The relative contribution of the convective mechanism depends on the operating condition and the combustor geometry, which determine the Strouhal number and thus the gain and phase of the integral FTF according to Eq. 6.43. Higher injector tube velocities, lower cut on frequencies or shorter flames due to smaller injector tube diameters or more reactive fuels might yield a dominating contribution of the convective driving mechanism due to lower Strouhal numbers, see also Section 6.6.

## 8.2 Experimental Setup Without Pilot Burner for Natural Gas and Hydrogen

The results provided in the previous Section 8.1 reveal detailed insights into the flame response mechanisms of premixed jet flames. The results suggest a significant contribution of axial acoustic velocity perturbations at the dump plane as a source of HF vortex shedding and coherent reaction rate fluctuations at the flame front for the resonant, pressure-node coupled injector tube length. However, the acoustic field in the injector tubes has not been measured and the pilot flame limits the observability, which is the motivation for the modified test rig design used in this section.

The pilot burner in the experimental setup depicted in Fig. 8.13 is removed to eliminate the influence of the pilot flame. The geometrical parameters of the test rig are provided in Tab. 8.4. In comparison to the former geometry, a constant injector tube length of  $L_T = \lambda_{T1} = 147$  mm is used. The upgraded test rig provides the option of pressure measurements in the injector tubes at  $T_1$  and  $T_2$  using high-temperature pressure transducers (*PCB 176A02*, sensitivity  $87 \pm 20\%$  pC bar<sup>-1</sup>) and charge amplifiers (*PCB-045M19B/010*, amplification 4 mV pC<sup>-1</sup>) with a total sensitivity of  $\approx 3.5 \pm 20\%$  mV Pa<sup>-1</sup>. Relative calibration of the high-temperature PCBs (*PCB 176A02*) with a reference sensor of *PCB 106B* reveals that the relatively high uncertainty of  $\pm 20\%$  is only valid for very

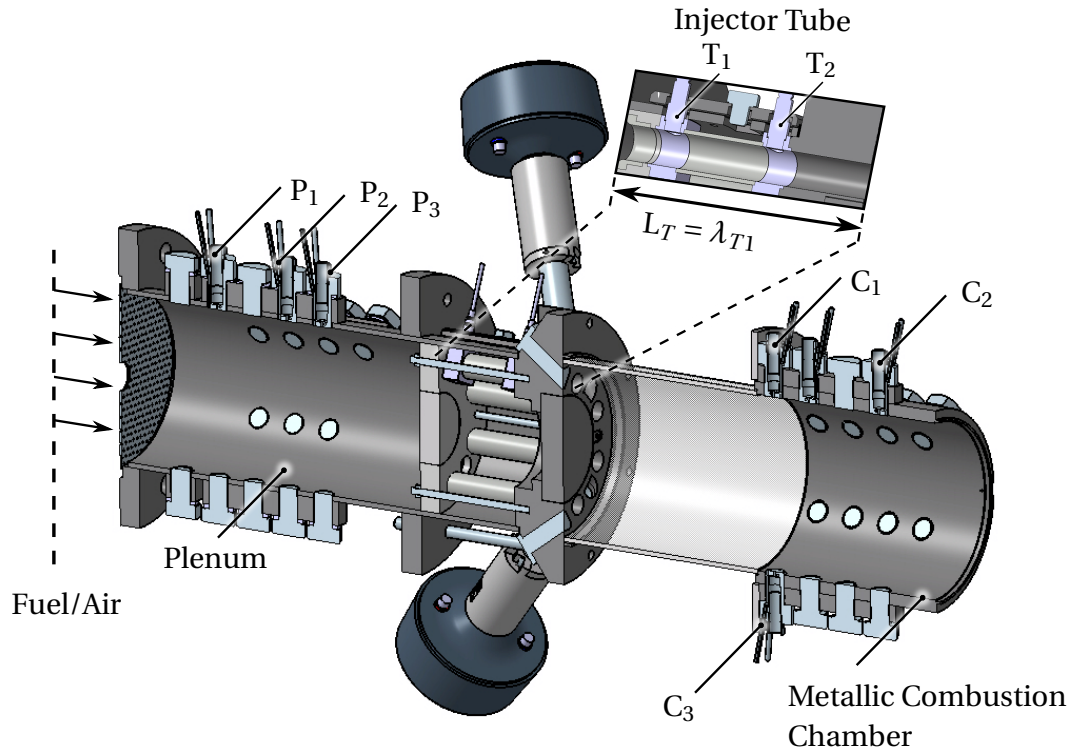


**Figure 8.13:** Experimental setup for the integrated  $\text{OH}^*$  images and simultaneous pressure measurements at the positions  $C_1 - C_2$ ,  $P_1 - P_3$  and  $T_1 - T_2$  without pilot burner.

small pressure amplitudes  $< 50$  Pa. In the measurement region of interest  $> 50$  Pa, the uncertainty reduces to less than  $\pm 5\%$ . The T1 mode is forced by four acoustic drivers located at the former  $\text{FP}_1 - \text{FP}_4$  positions to obtain higher forcing amplitudes. The former triangular forcing inlets are closed.

The investigation of the acoustic field in the injector tubes is part of the validation of the flame response model in Section 9. This section focusses solely on the perfectly premixed flame response of the natural gas and hydrogen jet flames with an injector tube designed for pressure anti-node coupling at the

**Table 8.4:** Geometry of the MJC without pilot burner in [mm]

$d_P$	$d_T$	$r_T$	$d_{C,\text{quartz}}$	$d_{C,\text{metallic}}$	$L_T \approx \lambda_{T1}$	$L_P$	$L_{C,\text{quartz}}$	$L_{C,\text{metallic}}$
150	18	58.5	155	158	147	306.5	203	187

dump plane of the test rig configuration without pilot burner.

Similarity of the acoustic injector response is achieved using a constant unburned gas temperature of  $T_u = 673$  K for hydrogen and natural gas for the investigated injector tube length. The operation conditions are summarised in Tab. 8.5.

**Table 8.5:** Operating Conditions for the MJC without Pilot Burner

fuel	$\lambda_F$ [-]	$T_u$ [K]	$T_b$ [K]	$Y_{\text{pilot}}$ [-]	$\dot{m}_{\text{air}}$ [g s <sup>-1</sup> ]	$\bar{u}_T$ [m s <sup>-1</sup> ]	$P_{\text{th}}$ [kW]
CH <sub>4</sub>	1.5	673	2070	0.0	110	117.6	211.4
H <sub>2</sub>	2.2	673	1880	0.0	108	112.5	175.4

The mean heat release distribution and the radially and axially integrated distributions are depicted for natural gas and hydrogen in Figs. 8.14 and 8.15, respectively. The hydrogen flame stabilises directly at the injector tube front plate, whereas the natural gas flames show a significant lift-off. The initial absence of OH\* intensity within the first eight mm is due to the metallic step covering the quartz glass chamber. The hydrogen flames point towards the chamber's centre due to the inner recirculation zone, which yields a slightly tilted, non-symmetric flame shape observed at the top and bottom flames. In the case of hydrogen, the maximum HRR is at  $x \approx 45$  mm for the  $L_{\text{FI}} \approx 100$  mm long flames. For the natural gas case, the HRR maximum is around  $x \approx 70$  mm for the  $L_{\text{FI}} \approx 200$  mm long flames. The radial heat release distribution of the natural gas flames indicates a reduced overlap of the upper two and the lower two flames compared to the former configuration with pilot burner. The single hydrogen flames yield distinct peaks in the radial heat release distribution. Thus, an increased observability of the shear layer dynamics is expected.

The results of the phase-locked images of hydrogen and natural gas are provided in Fig. 8.16. The HRR density fluctuations  $\dot{q}'(\varphi)$  in the middle of the plot are normalised by half of the maximum of the phase-locked HRR density indicated by  $\dot{q}_{\text{max}/2}$  for better observability of the fluctuations. Similar to the previous results, a clear pattern of HRR fluctuations due to acoustically induced coherent vortex shedding originating from the front plate is observed.

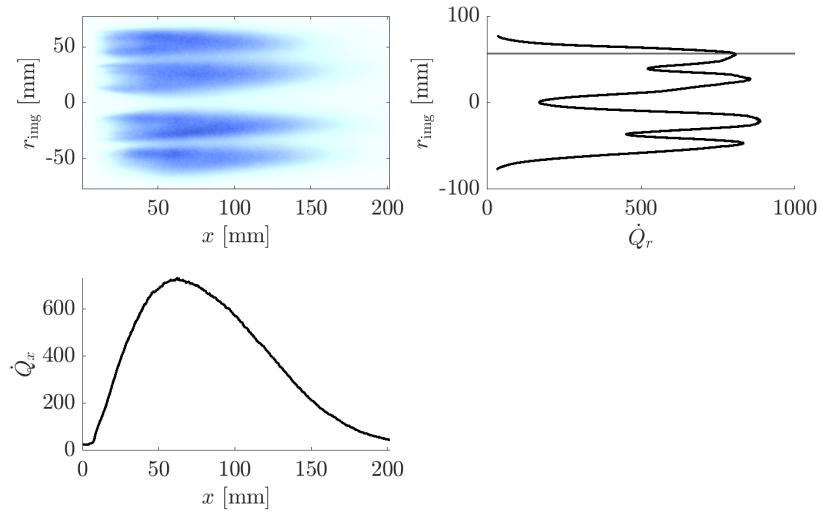


**Figure 8.14:** Line-of-sight integrated mean HRR density distribution (top-left) and the corresponding integral axial (bottom-left) and radial (top-right) distribution for the MJC without pilot burner for natural gas operation according to Tab. 8.5.

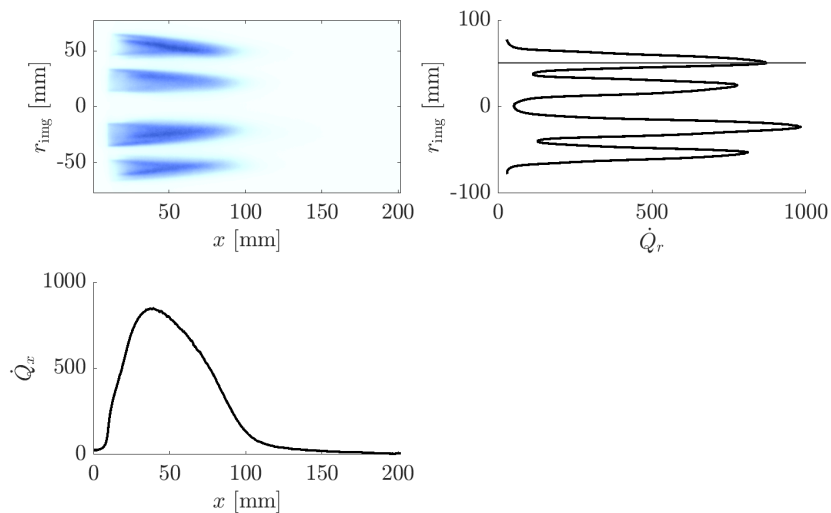


**Figure 8.15:** Line-of-sight integrated mean HRR density distribution (top-left) and the corresponding integral axial (bottom-left) and radial (top-right) distribution for the MJC without pilot burner for hydrogen gas operation according to Tab. 8.5.

The symmetry in amplitude with an opposed sign between the upper and the lower half of the combustor indicates the standing T1 mode. The axial evolution of the local phase of the HRR fluctuation originates from the initial phase of the acoustic velocity at the front plate and the local time delay of the coherent vortex at the respective flame position. The results reveal additional insights into the jet flame dynamics due to the increased observability of the shear layer dynamics.

In the following, the inner flames at approximately  $r_{\text{img}} = \pm 25$  mm are discussed for hydrogen and natural gas: The inner flames reveal competing effects indicated by a variation in the phase of the HRR fluctuation density. Consider only the upper half for hydrogen in the following. The HRR fluctuations at  $r_{\text{img}} = 35$  mm indicate a phase shift in HRR fluctuations by  $\pi$  compared to the fluctuations over the entire cross-section of the flames at  $r_{\text{img}} = \pm 25$  mm. The vortex shedding at the inner flames is non-uniform in cross-sectional direction due to the additional effect of the transverse acoustic velocity. On the one hand, the axial acoustic velocity component yields a constant phase in HRR fluctuations in cross-sectional direction. On the other hand, the transverse acoustic velocity adds additional vorticity with an opposed sign in the cross-sectional direction of the jet flame. Thus, a competing effect of HRR fluctuations due to axial and transverse velocity fluctuations is observed. The additional effect of vortex shedding due to transverse velocity is observable for the hydrogen flames. The inner flames of the natural gas flames show less distinct observations, probably due to stronger turbulent dissipation of the HRR fluctuations in the natural gas flames. Nevertheless, the same effect might cause the inclination of the HRR fluctuations of the inner flames for natural gas. Note that the HRR fluctuations of the inward pointing half of the inner flames of natural gas at the radial positions  $r_{\text{img}} = \pm 17.5$  mm are larger in comparison to the outward pointing half of the inner flames at  $r_{\text{img}} = \pm 35$  mm, which is caused by the transverse velocity. Note, however, that the net effect of the transverse velocity contribution is negligible for compact injector tube diameters compared to the transverse acoustic mode shape  $d_T \ll \lambda_{r,\theta}$ , if the injector tube is entirely placed within the domain of the T1 mode of constant phase in cross-sectional direction, i.e the upper or lower half of the optical section. If, however, the injector tube is placed in the centre of the

## 8.2 Experimental Setup Without Pilot Burner for Natural Gas and Hydrogen

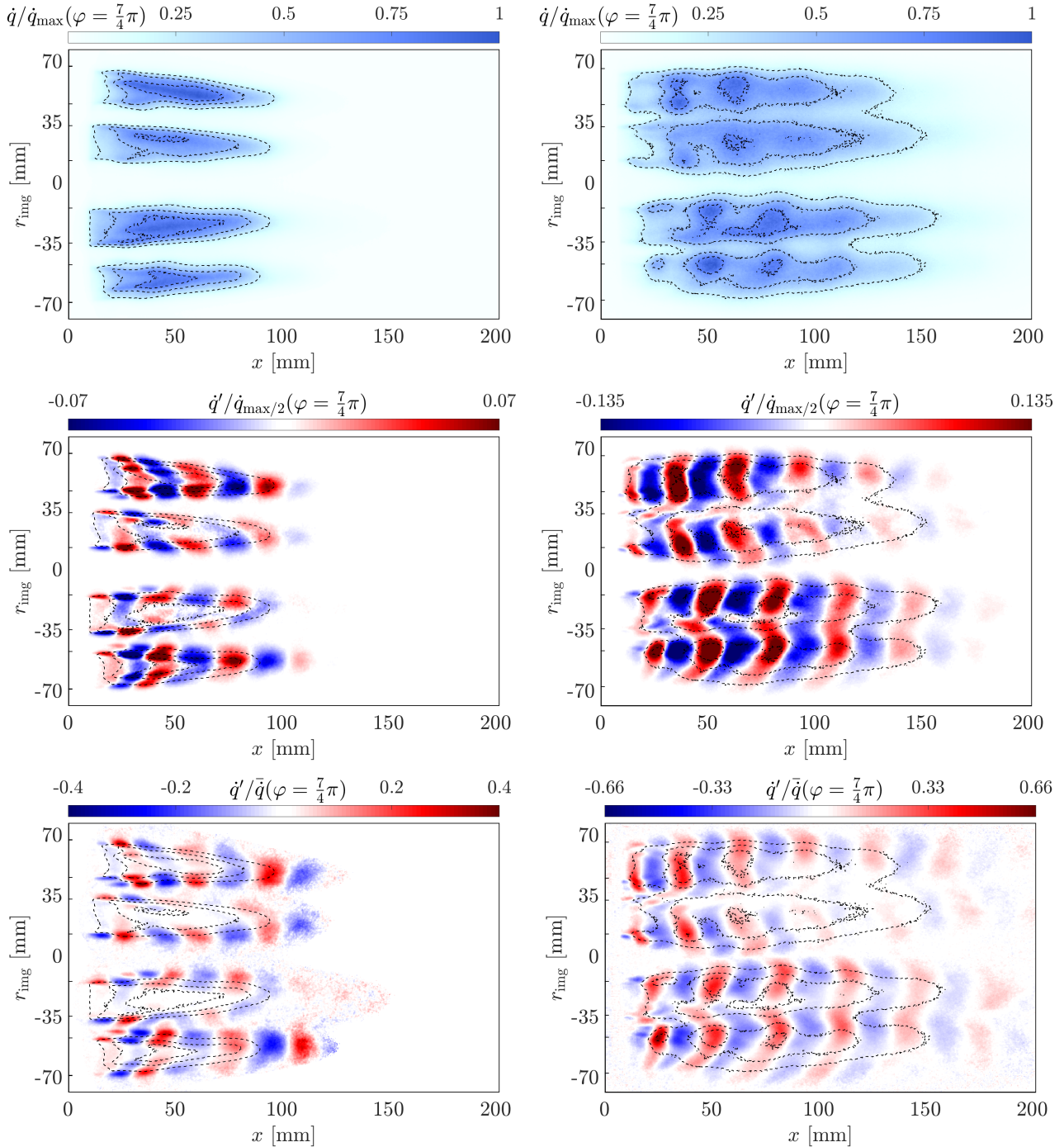


**Figure 8.16:** Phase-locked HRR  $\dot{q}(\varphi)$  (top), fluctuations  $\dot{q}'(\varphi)$  (middle) and normalised fluctuations  $\dot{q}'(\varphi)/\bar{q}$  (bottom) for H<sub>2</sub> (left) at  $f = 3175$  Hz and CH<sub>4</sub> (right) at  $f = 3100$  (Tab. 8.5).

transverse pressure node, the sign of the acoustic pressure varies between the cross-sectional T1 mode domains of constant positive or negative pressure. Thus, vortex shedding due to the transverse velocity might contribute to the driving potential of centred, single jet flames as, for instance, investigated by Sharifi et al. [39], McClure et al. [36] or Buschhagen et al. [34]. However, the net effect of the transverse velocity is arguably small in MJC, because the number of injector tubes at a transverse pressure node is small in comparison to the injector tubes placed at approximately constant positive or negative transverse acoustic pressure away from the nodal line.

Moreover, the outer flames at approximately  $r_{\text{img}} = \pm 55$  mm are discussed for hydrogen and natural gas. The outer flames show a clear, coherent pattern in HRR density with a constant phase over the entire cross-section. The HRR fluctuation nodal lines are oriented with an angle of close to  $90^\circ$ , which indicates the dominant cause of the coherent vortex shedding by axial acoustic velocity fluctuations at the dump plane. At the base of the hydrogen and natural gas flames higher intensities at the upper and lower part of the outer flames are observed. The vortical flow disturbance initiated at the edges of the injector tube exit yields a coherent vortex ring. Thus, the line-of-sight integrated HRR fluctuations are initially higher at the upper and lower part in comparison to the intensity in the centre of the flames due to the unburned core region. With increasing axial distance, the effect of the core region diminishes due to increased turbulent dissipation.

The flame response of the natural gas and the hydrogen jet flames of the investigated configuration without pilot burner shows a dominant convective flame response, consistent with the results of the configuration with pilot flame in Section 8.1. Contrary to the natural gas jet flames with pilot burner, a higher degree of dissipation in axial direction is noted. The normalised HRR fluctuations  $\dot{q}' / \bar{\dot{q}}$  show a significant decay with increasing axial position. Thus, the local coherent turbulent velocity fluctuations dissipate due to turbulent mixing. The hydrogen flames, however, show less turbulent dissipation, which is first of all due to their shorter length but second of all due to the flame stabilisation close to the unburned gas core region that includes lower turbulence compared to the shear layer. In contrast to the results of the configuration

with pilot burner, the flame response of the natural gas jet flames without pilot burner shows a significant initial increase in the distance of the HRR fluctuation nodal lines at the base of the flames. This indicates an acceleration in the axial convection velocity of the HRR patches. With increasing distance from the flame base, the turbulent flame speed increases due to the jet turbulence, and the flame moves closer to the unburned jet core region in radial direction, which yields higher axial velocity, i.e. higher distance between the HRR fluctuation nodal lines. The case with pilot burner yields stabilisation of the jet flames close to the unburned core region in cross-sectional direction also at the flame base. This implies higher initial axial convection velocity and less turbulent dissipation since the core region is dominated by the initial turbulence level in the injector tube, which is low compared to the turbulence in the shear layer of the jet.

In conclusion, the results for the MJC configuration with and without pilot burner emphasise the importance of flame stabilisation relative to the shear layer [10] concerning the convective flame response. For a flame stabilisation closer to the core region in cross-sectional direction the axial convection velocity of the HRR fluctuations increases and their dissipation decreases. Flame stabilisation in the shear layers yield a significant dissipation of the HRR fluctuations, which needs to be accounted for the modelling of the flame response, as also further analysed in the next chapter.

## 9 Validation of the Flame Response Model

The validation of the distributed flame response model derived in Chapter 5 is provided in this section based on the flame response of the natural gas jet flames with and without pilot burner for similar operating conditions. The unburned gas is preheated to  $T_u = 673$  K at an air excess ratio of  $\lambda_{\text{CH}_4} = 1.5$ , which yields the adiabatic flame temperature of  $T_b = 2070$  K. The air mass flow rate is slightly varied between  $\dot{m}_{\text{air}} = 120$  g s<sup>-1</sup> (with pilot) and  $\dot{m}_{\text{air}} = 110$  g s<sup>-1</sup> (without pilot) to maintain a similar injector tube bulk velocity of  $\bar{u}_T = 115$  ms<sup>-1</sup>.

### 9.1 Mean Heat Release and Flow Field

The axially resolved flame response model needs input data for the increase in axial mean velocity and possible turbulent dissipation over the extent of the flame. Therefore, the axial mean HRR density and axial mean flow velocity are obtained from a fit to the experimental data.

The mean heat release distribution in axial direction is fitted by a skew-normal distribution scaled with the integral heat release

$$\xi = \frac{\bar{Q}_x(x)}{\bar{Q}} = 2\phi(x)\Phi(x) \quad (9.1)$$

given by the probability normal distribution  $\phi(x)$  and the cumulative normal distribution  $\Phi(x)$

$$\phi(x) = \frac{1}{\sigma_{\dot{q}}\sqrt{2\pi}} \exp\left(-\frac{1}{2}\left(\frac{x - \bar{x}_{\dot{q}}}{\sigma_{\dot{q}}}\right)^2\right), \quad (9.2)$$

$$\Phi(x) = \frac{1}{2} \left( 1 + \operatorname{erf}\left(\frac{\alpha_{\dot{q}}(x - \bar{x}_{\dot{q}})}{\sqrt{2}\sigma_{\dot{q}}}\right) \right), \quad (9.3)$$

which are defined by the variance  $\sigma_{\dot{q}}$  and the weighted axial position of the mean HRR  $\bar{x}_{\dot{q}}$  and the skewness factor  $\alpha_{\dot{q}}$ . The axial coordinate of the flame  $x$  is zero at the injector tube exit.

Additionally, the mean flow velocity profile needs to be estimated from the experimental data. The local transport velocity might be assumed constant in cross-sectional direction at each flame, considering a uniform mass flow split between the eight injector tubes. The axial velocity at the flame  $\bar{u}(x)$  might deviate to lower values compared to the theoretical injector tube velocity  $\bar{u}_T = 115 \text{ ms}^{-1}$  due to first the boundary layer at the injector tube wall and second the mixing of the unburned gas with the recirculated exhaust gas. The mean axial propagation velocity of the HRR fluctuations is fitted to an Error Function distribution

$$\bar{u}(x_C) = \bar{u}_0 \left( 1 + a_{\bar{u}} \frac{1}{2} \left( 1 + \operatorname{erf} \left( \frac{(x - \mu_{\bar{u}})}{\sqrt{2}\sigma_{\bar{u}}} \right) \right) \right). \quad (9.4)$$

The phase slope of the radially integrated HRR fluctuations of the model  $\angle \dot{Q}'_{\text{model}}$  is fitted to the experimental phase slope  $\angle \dot{Q}'_{\text{exp}}$  employing Eq. 9.4 and the convective flame response model Eq. 5.22.

The radially integrated mean HRR distribution of the experimental results for natural gas with and without pilot burner alongside the fitted axial velocity profiles are depicted in Fig. 9.1. First, consider the results for the case without pilot burner on the right-hand side of Fig. 9.1. The fitted skew normal distribution reveals a good agreement with the experimental results without pilot burner. The skewness of the heat release distribution is a result of the superposition of the approximately conical jet flame shape with decreasing flame area in the axial direction and the reaction progress perpendicular to the flame surface. The fitted velocity profile to the phase slope  $\angle \dot{Q}'_{\text{exp}}$  starts in the Error Function's linear slope and captures the saturation for larger distances from the exit plane. The velocity profile reveals an approximately linear acceleration from the velocity of  $\bar{u}_C(x = 0) = 60 \text{ ms}^{-1}$  at the flame base and saturates at  $\bar{u} \approx 90 \text{ ms}^{-1}$  at the flame tip.

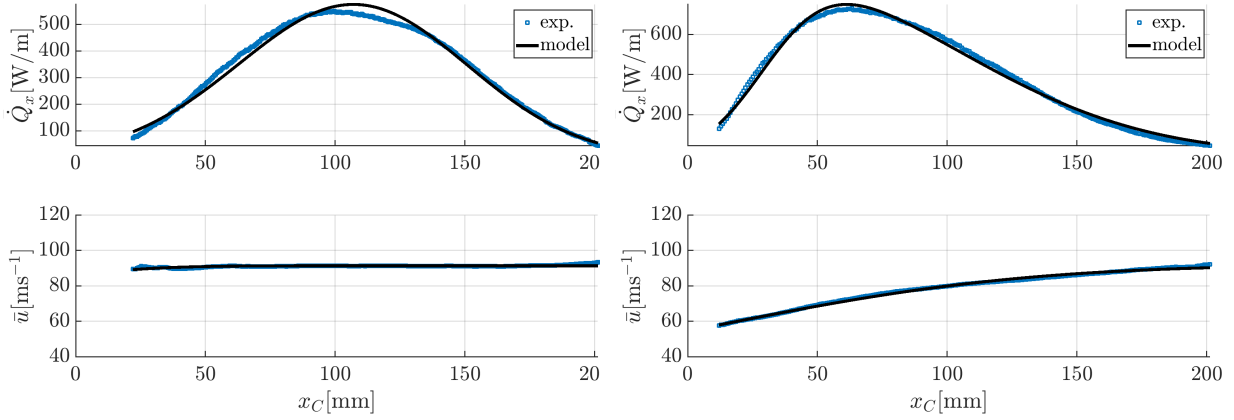


**Figure 9.1:** Axial mean HRR distribution  $\bar{Q}_x$  (top) and the axial velocity profile  $\bar{u}$  (bottom) fitted to the experimental results of natural gas with pilot burner (left) and without pilot burner (right) for  $T_u = 673$  K,  $\lambda_{\text{CH}_4} = 1.5$  and  $\bar{u}_T = 115$  ms<sup>-1</sup>.

Second, the case with pilot burner on the left-hand side of Fig. 9.1 can be fitted to a Gaussian axial mean HRR distribution with a skew factor close to zero. The axial mean velocity of the HRR fluctuations stays approximately constant over the extent of the flame at about  $\bar{u} \approx 90$  ms<sup>-1</sup>. The results suggest a flame stabilisation closer to the core region of the unburned jet in cross-sectional direction of the flames in the case with pilot burner due to the approximately constant and higher convection velocity compared to the case without pilot burner. On the contrary, flame stabilisation in the turbulent shear layer in the case without pilot seems reasonable due to the decreased axial flow velocities. The observation of decreasing normalised HRR density fluctuations in Fig. 8.16 for natural gas supports this hypothesis as a higher turbulent dissipation of the convective flame response is to be expected with flame stabilisation in the turbulent shear layer.

Therefore, turbulent dissipation becomes significant for the case without pilot flame and an estimate of the turbulent viscosity is required for the convective-diffusive transport model. In the similarity region of the turbulent jet, the turbulent viscosity is approximately constant [86, 93]. An estimate of the core region of the jet flames according to Hirsch [94]  $L_{\text{core}} = 6.57d_{\text{eq}}$  with the mo-

momentum weighted equivalent tube diameter  $d_{\text{eq}} = d_T \sqrt{\frac{\rho_u}{\rho_b}}$  yields an unburned jet core region length of  $L_{\text{core}} \approx 10d_T$  for engine-similar operation conditions as used in the experiments. Thus, the premixed jet flames stabilise within the axial distance of the core region of the unburned gas jet. The core region  $x/d_{\text{eq}} < 6.57$  [86, 94] is characterised by increasing stochastic turbulent length scales  $l_t$  and increasing stochastic turbulence intensity  $u'_t$  which are modelled via

$$\frac{u'_t}{\bar{u}_0} = \frac{0.2}{6.57} \frac{x}{d_{\text{eq}}} + \frac{u'_{t,0}}{\bar{u}_0}, \quad (9.5)$$

$$l_t = l_{t,0} + \left(0.108d_0 - \frac{l_{t,0}}{6.57}\right) \frac{x}{d_{\text{eq}}}, \quad (9.6)$$

according to Hirsch [94] based on the review of Lawn [86]. Thus, a first-order approximation of the turbulent viscosity following the Boussinesq hypothesis yields

$$\nu_t = 0.1u'_tl_t \quad (9.7)$$

a quadratic increase of the turbulent viscosity with the axial direction. The turbulent viscosity increases from the initial tube turbulence to a value of  $\nu_t = 0.025 \text{ [m}^2\text{s}^{-1}\text{]}$  according to the estimation according to Eqs. 9.5–9.7, which is in line with numerical and experimental results on jet turbulence for instance by Kuhn et al. [93]  $\nu_t = 0.0259 \text{ [m}^2\text{s}^{-1}\text{]}$ . The initial injector tube turbulence intensity and length scale might be estimated for a turbulent pipe flow [95, 96]. The initial turbulent length scale  $l_{t,0} \approx 0.1d_T$  and the initial stochastic turbulent velocity fluctuations  $u'_{t,0} \approx 0.05\bar{u}_T$  yield a low contribution to the turbulent viscosity compared to the development of the jet turbulence.

## 9.2 Convective Flame Response with Pilot Burner

Validation is provided by the experimental results on the flame response with pilot burner. The acoustic pressure field in the injector tube is not measured in the test rig configuration with pilot burner. Therefore, the CFD/CAA method including the distributed flame response model is applied and the acoustic pressure field is fitted to the experimental data of the dynamic pressure sensors.

The MJC with pilot burner is modelled numerically as depicted in Fig. 9.2. The mean temperature field is simplified to a constant preheat temperature of  $T_u = 673$  K in the plenum, the injector tubes, the swirl stabilised pilot burner and the unburned core region of the flames. The exhaust gas temperature  $T_b = 2070$  K is estimated at adiabatic conditions. The Gaussian mean HRR distribution in axial direction according to Fig. 9.1 is applied. The convective wave number in the numerical model is estimated by a constant flow velocity justified by Fig. 9.1. Impedance boundary conditions representing the low Mach number perforated plate  $z_{\text{up}} = 2$  and the boundary condition downstream of the combustor  $z_{\text{do}} = 100$ , which corresponds to the reflective axial boundary condition measured in the experimental forced response. The re-

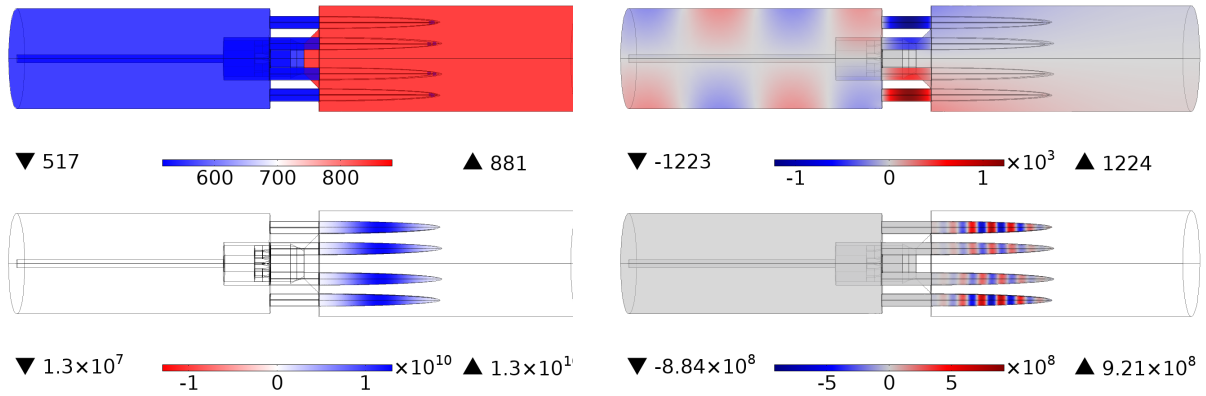


**Figure 9.2:** Mean speed of sound [ms<sup>-1</sup>] (top-left), mean HRR density [Wm<sup>-3</sup>] (bottom-left) and the resulting acoustic pressure mode shape [Pa] (top-right) and the convective HRR density fluctuations [Wm<sup>-3</sup>] (bottom-right) of the numerical Helmholtz model at 3100 Hz considering a preheat temperature of  $T_u = 673$  K and an adiabatic flame temperature of  $T_b = 2070$  K.

sulting acoustic pressure mode shape in Fig. 9.2 shows the strong axial acoustic pressure gradients indicating high axial velocity fluctuations at the injector exit in comparison to the evanescent T1 mode shape in the combustion chamber. The application of the distributed convective model (Eq. 5.22) to the CFD/CAA method provides a first qualitative validation of the flame response model as depicted in Fig. 9.2, which shows the similarity of the local numerical flame response to the experimental results. Despite the rough simplification

## 9.2 Convective Flame Response with Pilot Burner

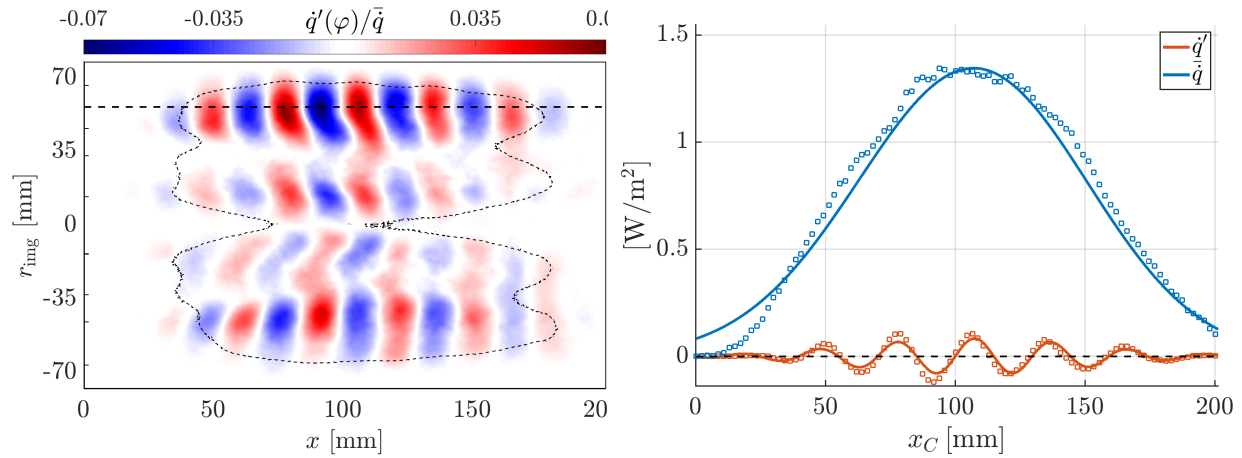


**Figure 9.3:** Forced flame response for  $\varphi = 0$  at a preheat temperature of  $T_u = 673$  K and an air excess ratio of  $\lambda_{\text{CH}_4} = 1.5$  at 3100 Hz of the MJC with pilot burner (left) and the comparison of the experimental flame response ( $\square$ ) to the flame response model (—) according to Eq. 5.22 for negligible turbulent dissipation (right) at the upper flames, indicated by the dashed line.

of the mean heat release field in cross-sectional direction, the numerical results show a good agreement in terms of the axial pattern of the heat release fluctuations. The amplitude dependency on the Bessel function observed in the experimental flame response in the radial direction is captured by the model. Note that the axial pattern in heat release fluctuations caused by axial acoustic velocity fluctuations at the dump plane determines the phase and the gain of the resulting global flame transfer function, see Section 6.6. Thus, the model captures the main physical contribution of the convective driving mechanism with a locally resolved flame response.

The upper dashed line in Fig. 9.3 indicates the fixed radial position used for quantitative validation depicted on the right-hand side of Fig. 9.3. The axially resolved, convective flame response according to Eq. 5.22 yields a good agreement to the experimental flame response assuming negligible turbulent dissipation and a constant flow velocity. The flame response is determined by the axial acoustic velocity, the axial convective wave number and the mean heat release. In the absence of acoustic pressure measurements in the injector

tube, the axial acoustic velocity amplitude at the reference position is reconstructed from the numerical model via a fit to the measured pressure sensor data. The fitted pressure field yields a normalised axial velocity fluctuation at the exit of the injector tube of  $\hat{u}_u = 6.5e^{i \cdot \angle \hat{u}_u} \text{ ms}^{-1}$ . The phase angle  $\angle \hat{u}_u = 2.3$  rad is extracted from the numerical results. Since the experimental flame response is phase-locked to the pressure sensor  $C_1$ , the phase difference of the complex axial acoustic velocity and the complex acoustic pressure at the sensor position  $C_1$  yields the phase-locked axial velocity fluctuations at the reference position  $\angle \hat{u}_u = \angle \hat{u}_{x,u} - \angle \hat{p}_{C_1}$  extracted from the numerical model. The resulting flame response shows good agreement between the experimental and analytical heat release rate fluctuations when assuming a gain of  $n \approx 1.1$ . The local phase of the flame response highly depends on the initial phase angle  $\angle \hat{u}_u$ . The result of the model for the phase of the convective flame response modelled by a constant convection velocity of  $\bar{u} \approx 90 \text{ ms}^{-1}$  and accounting for the fitted phase angle  $\angle \hat{u}_u$  yields excellent agreement with the experimental results. Moreover, the phase of the flame response depicted in Fig. 9.3 is constant in cross-sectional direction in the upper and lower halves, respectively, due to the standing T1 mode. Therefore, the phase-aligned and radially integrated HRR fluctuations in Fig. 9.4 yield the same phase of the HRR fluctuations at the same axial position.

The same velocity fluctuations at the reference position of  $\hat{u}_u = 6.5e^{i \cdot \angle \hat{u}_u} \text{ ms}^{-1}$  and the gain of  $n = 1.1$  reveal a good agreement of the experimental results to the cross-sectionally integrated model. Thus, the scaling of the local HRR density fluctuations (Fig. 9.3, right-hand side) to the phase-aligned cross-sectionally integrated fluctuations (Fig. 9.4) is appropriate. The normalised HRR fluctuations at the top of Fig. 9.4 reveal negligible attenuation due to turbulent dissipation of the coherent velocity fluctuations since the amplitude of  $\dot{Q}'_x / \bar{Q}_x$  is preserved over the length of the flame. Thus, the simplified turbulent diffusion model 9.7 using jet theory does not apply anymore since the interaction of the swirl-stabilised pilot flame and the jet flames results in a stabilisation of the jet flames in the core region of the unburned jet with significantly lower turbulence levels.

The results discussed above outline the applicability and efficiency of the con-

vective flame response model for complex three-dimensional geometries using the numerical CFD/CAA model. In the next section, the acoustic field in one injector tube is measured to provide a quantitative validation independent of the numerical acoustic pressure field reconstruction.

### 9.3 Convective Flame Response without Pilot Burner

This section aims to validate the local HRR flame response according to Eq. 5.22 with the optical experimental results of the MJC without pilot burner and including the measurement of the acoustic field in the injector tube.

The required axial acoustic velocity fluctuations  $\hat{u}_u$  at the reference position are reconstructed from the dynamic pressure sensors at the positions  $T_1$  and  $T_2$  of the experimental setup without pilot burner in Fig. 8.13 using the MMM, see Section 4.2. The Mach number of  $M_T \approx 0.23$  in the injector-tube is accounted for in the acoustic wave number for the mode shape reconstruction.

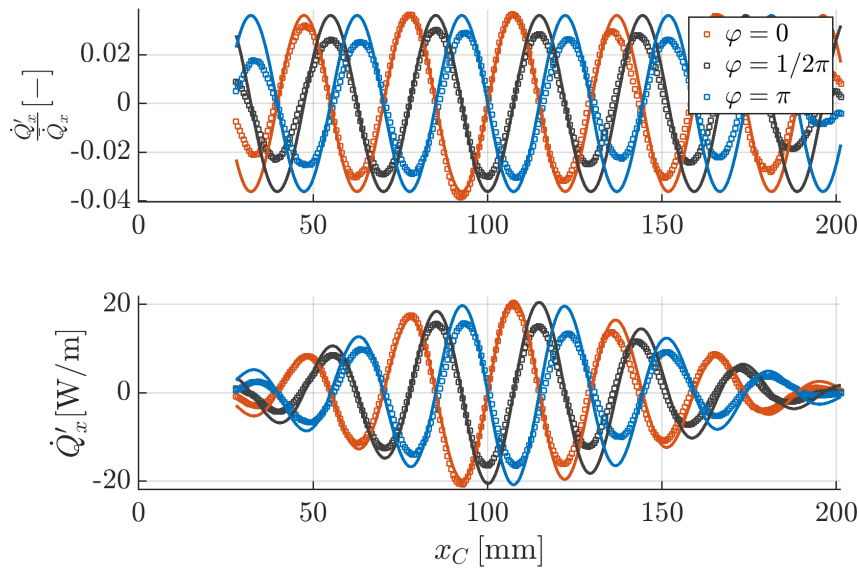


**Figure 9.4:** Validation of the axially resolved flame response model (—) with the phase-locked radially integrated HRR fluctuations of the experimental results (□) with pilot burner for natural gas.

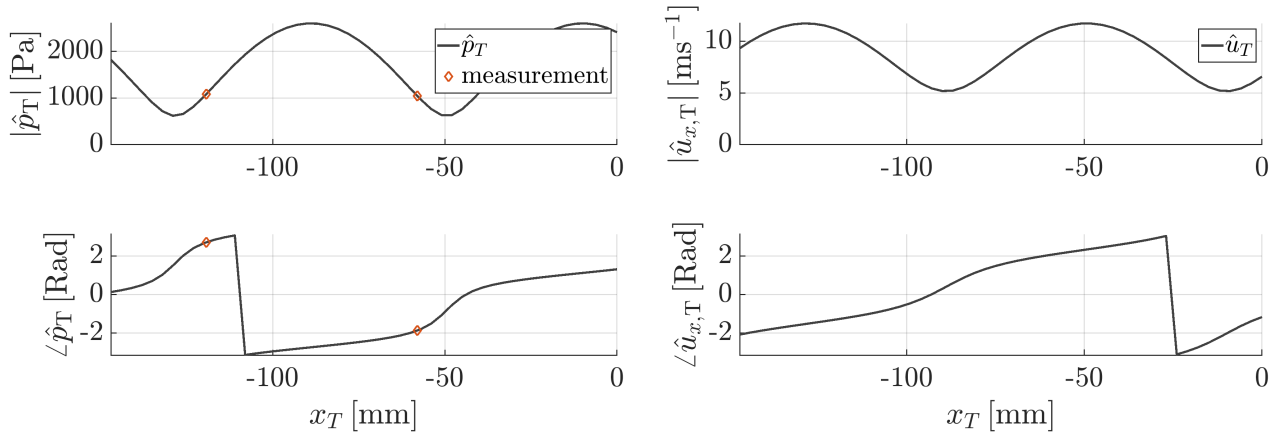


**Figure 9.5:** Reconstructed acoustic pressure (left) and axial acoustic velocity field (right) in the injector tube using the two dynamic pressure sensors  $T_1$  and  $T_2$ .

The reconstructed axial acoustic velocity mode shape in the injector tube is depicted in Fig. 9.5. The sensors  $T_1$  and  $T_2$  are indicated by the orange diamonds in the acoustic pressure mode shape. The resulting acoustic pressure and axial acoustic velocity at the injector tube exit  $x_T = 0$  yields  $|\hat{u}_T(x_T = 0)| \approx 6 \text{ ms}^{-1}$ .

The flame response model is validated with the cross-sectionally integrated HRR density fluctuations, consistent with the previous experimental results. The phase shift in cross-sectional direction is accounted by Eq. 8.1 such that the HRR density fluctuations are phase-aligned by the sign of the real-valued transverse acoustic pressure mode shape, which yields  $\dot{Q}'_x$ . The resulting prediction of the cross-sectional integrated flame response model according to Eq. 5.22 and the experimental results are depicted in Fig. 9.6 for the case of natural gas according to Fig. 8.16. The cross-sectionally integrated fluctuations  $\dot{Q}'_x$  are shown at the bottom and the normalised fluctuations  $\dot{Q}'_x/\bar{Q}_x$  at the top of Fig. 9.6.

The results are depicted for three different phase bins and generally show good agreement with the analytical model according to Eq. 5.22 using a prescribed gain of  $n = 5.5$ . The convective flame response according to Eq. 5.22 prescribes an initial gain of the FTF and accounts for convective-diffusive

transport of the coherent velocity fluctuation in the axial direction. Thus, the gain starts at the prescribed value  $n = 5.5$  and decreases with axial direction due to turbulent diffusion of the coherent velocity fluctuations. The turbulent dissipation yields a decreasing envelope of the normalised cross-sectionally integrated fluctuations  $\dot{Q}'_x / \bar{Q}_x$ . The decrease in the envelope of  $\dot{Q}'_x / \bar{Q}_x$  is captured very well, accounting for the simplicity of the turbulent viscosity model of the mean field, see Eq. 9.7. The phase of the HRR fluctuations is in excellent agreement with the model using the fitted axial velocity profile depicted in Fig. 9.1. In comparison to the previous results with pilot burner the local hydrodynamic gain rises to the value of  $n = 5.5$ , which might be due to the differences in the flame stabilisation in cross-sectional direction. The case with pilot flame stabilises closer to the core region in cross-sectional direction, which is characterised by less coherent and stochastic turbulence. Thus, the hydrodynamic instability in the shear layer might yield a higher gain in the case without pilot burner.

Moreover, the globally integrated HRR fluctuations and the simplified

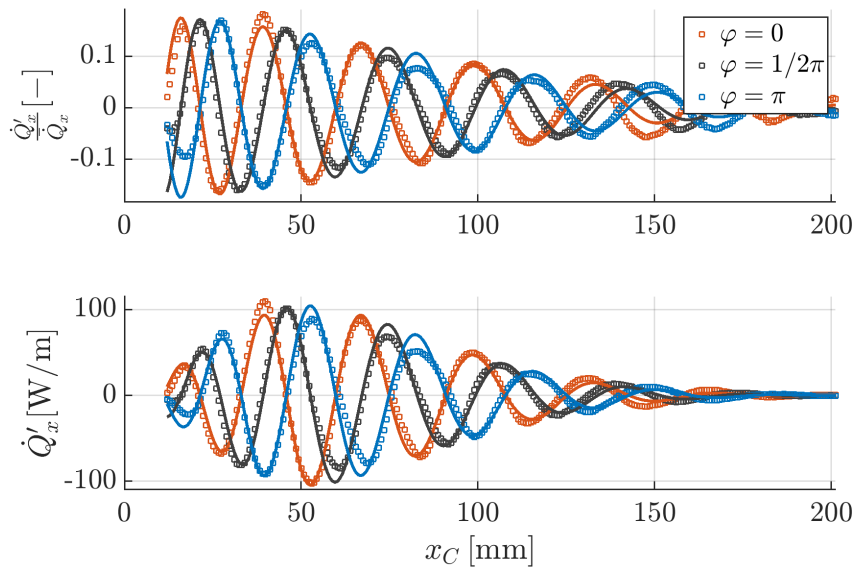


**Figure 9.6:** Validation of the axially resolved flame response model (—) with the phase-locked radially integrated HRR fluctuations of the experimental results (□) without pilot burner for natural gas.

Rayleigh integral according to Eq. 8.4 predicted by the model agree very well with the experimental HRR fluctuations as depicted in Fig. 9.7. The integral fluctuations are normalised with the thermal power and depicted over one period of the oscillation indicated by the normalised phase bin of the phase-locked images. Although the predicted amplitude of the model is lower compared to the experimental results, the trend of the amplitude and, in particular, the phase is captured by the model. The phase between the measured integral HRR rate and the acoustic pressure sensor  $C_1$  is below  $\pi/2$ , which yields a positive Rayleigh integral. The initial region  $0 < x_C < 12$  mm in Fig.

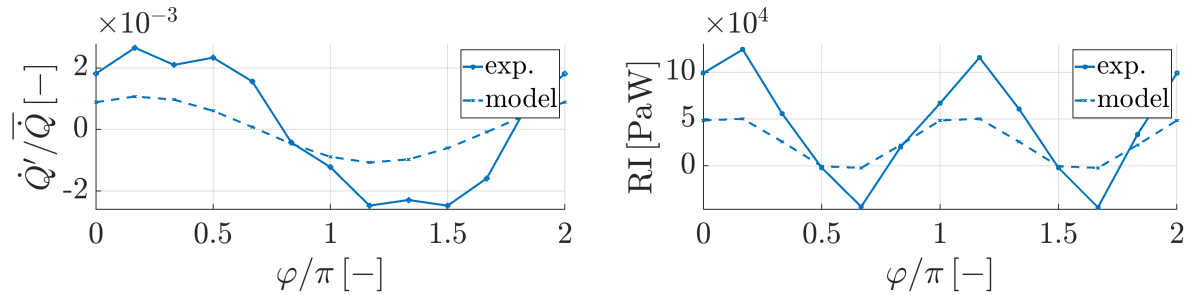


**Figure 9.7:** Globally integrated HRR fluctuations (left) and simplified Rayleigh integral (right) for all phase bins for the MJC without pilot burner.

9.6 is neglected for the validation. The initial region of  $0 < x_C < 8$  mm is covered by the metallic step of the front plate. In the small extent of  $8 < x_C < 12$  mm, the predicted amplitude of the flame response using a prescribed gain deviates to higher values compared to the experiment. The predicted global response in Fig. 9.7 deviates significantly from the experiment if the small extent of  $8 < x_C < 12$  mm is included. Thus, the initial increase in gain should be accounted for in an advanced model for increased accuracy, which is further stressed by the results of the distributed  $\text{FTF}_x$  in the next section.

The validation of the flame response model with the MJC configuration with pilot burner emphasises the capabilities of the CFD/CAA method to reproduce the measurement of the acoustic field in the injector tubes. The resulting fit of the acoustic field to the measured dynamic pressure sensor data results in high acoustic pressure gradients at the injector tube exit, which yields coherent vortex shedding as the reason for the flame response. The case without pilot burner with measurement of the acoustic field in the injector tubes val-

idates the axial acoustic velocity fluctuations at the injector tube exit as the root cause of the convective flame response. The differences in local gain and axial flow velocity of the configuration with and without pilot burner might be due to the stabilisation of the flame relative to the shear layer. The hypothesis is that the jet flames without the pilot burner stabilise further outside of the core region in cross-sectional direction, and the case with the pilot flame (or the hydrogen flames) stabilise further inside the core region in cross-sectional direction. This might explain the higher gain of  $n = 5.5$  due to stronger hydrodynamic instability in the shear layer of the case without pilot burner. Consistent with the hypotheses of flame stabilisation further outside of the core region in the turbulent shear layer, the initial axial convection velocity of the case without pilot burner is lower and the turbulent dissipation increases in comparison to the case with pilot burner. This hypothesis, however, requires further investigations in the future to be verified.

## 9.4 Axially Distributed Convective FTF

The previous section validates the model based on the integral cross-sectionally phase-aligned HRR fluctuations, which accounts solely for the phase of the transverse acoustic pressure field. In order to obtain the global or axially distributed flame transfer function  $\text{FTF}_x$  according to Eqs. 6.32 and 6.33, however, an estimate for the local Rayleigh index is required, which is provided in this section.

The axially distributed flame transfer function  $\text{FTF}_x$  according to Eq. 6.37 is obtained from the partial derivative in axial direction of the global FTF

$$\text{FTF}_x(x) = \frac{1}{\xi(x)} \frac{\partial \text{FTF}}{\partial x} = \frac{\hat{Q}_{mn,x} / \bar{Q}_x}{(\hat{u}A)_{mn,u} / (\bar{u}A)_u} \quad (9.8)$$

and is, thus, solely dependent on the cross-sectional integrated mean HRR and the cross-sectional integrated and acoustically weighted HRR fluctuations, see also Eq. 6.36. The convolution integral of the HRR fluctuations with the non-dimensional acoustic mode shape in cross-sectional direction according to Eq. 6.35 is determined from the phase-locked, line-of-sight inte-

grated  $\text{OH}^*$  images and the radial mode shape along the combustor centre line measured by the pressure sensors  $C_1$  and  $C_2$ . The Hilbert Transform [78] of the phase-locked and radially weighted and integrated HRR fluctuations reveals the axially resolved gain and phase of the cross-sectionally integrated HRR density fluctuations

$$\hat{Q}_{mn,x} = \mathcal{H} \left[ \int_A \Re[J_n(r)P_m(\theta)] \dot{q}'_{\text{exp}} dA \right] \quad (9.9)$$

accounting for the weighting with the non-dimensional transverse acoustic pressure mode shape.

The analytical FTF model is validated with the experimental results in Fig. 9.8. The absolute gain and phase of the experimentally determined axial FTF

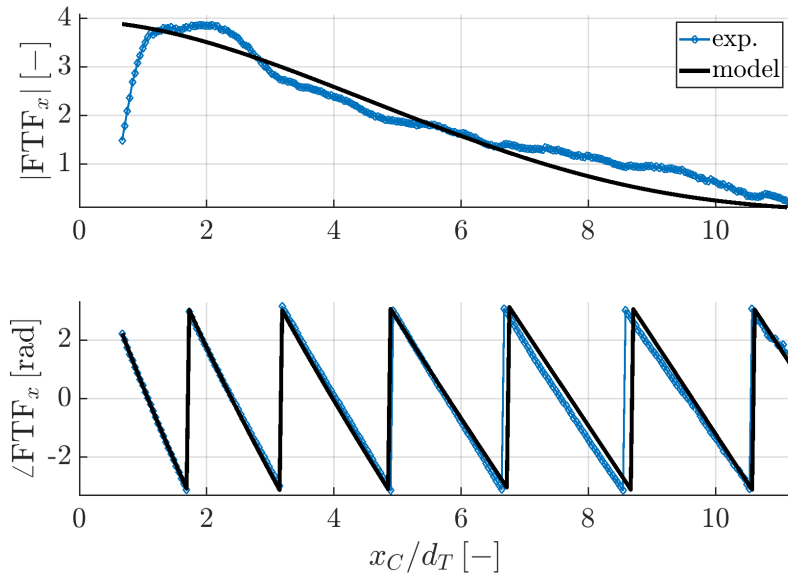


**Figure 9.8:** Validation of the axially resolved  $\text{FTF}_x$  with the radially integrated experimental flame response for natural gas.

using the flame response model provided by Eq. 9.8 and the analytical FTF according to Eq. 5.22. The prescribed initial gain of  $n = 5.5$  as used for the HRR response in Fig. 9.6 yields an amplitude of  $|\text{FTF}_x|(x_C = 0) \approx 4$  due to the cross-sectional weighting with the transverse acoustic field. The decreasing gain with increasing axial position confirms the prediction of the turbulent viscosity model, similar to the previous results in Fig. 9.6. The axial FTF gain

indicates a significant initial error of the model prediction compared to the experimental results within  $x_C/d_T < 2$ . A possible explanation for the deviations might be measurement errors of the  $\text{OH}^*$  signal due to high initial strain rates. However, the phase is in accurate agreement in the same region  $x_C/d_T < 2$  and thus measurement errors might be excluded. Thus, the initial increase in gain might be attributed to the increase in turbulence intensity of the coherent vortices due to radial velocity gradients, which are not accounted for by the flame response model according to Eq. 5.22.

The axial flame response according to Eq. 5.18 yields the flame response

$$\frac{\hat{q}_{\text{conv}}}{\bar{q}} = \frac{\hat{u}_{\text{ref}}}{\bar{u}_{\text{ref}}} e^{-ik_{\text{shear}}(x-x_{\text{ref}})}. \quad (9.10)$$

The convective wave number introduced in Eq. 5.18 indicates an increase in the hydrodynamic gain due to negative velocity gradients. Thus, the axial increase in the gain might originate from high radial velocity gradients in the shear layer close to the injector tube exit. Therefore, the axial evolution of the mean field gradients might be accounted for by the flame response model according to Eq. 9.10 to model the increase in the gain. However, detailed insights on the local mean flow field are required, which can hardly be estimated by first principles or extracted from the provided experimental results. The axial evolution of the mean radial velocity gradients at the flame might be extracted from a stationary CFD. The application of Eq. 9.10 to the CFD/CAA method with a CFD mean field might be considered in future work.

## 10 Summary and Conclusion

High frequency thermoacoustic instabilities in Multi-Jet Combustors occur at high cut-on frequencies, and therefore, the high-cycle fatigue limits of the combustor are reached within seconds. These instabilities' thermoacoustic coupling mechanisms are predominantly unknown. However, the fundamental understanding of the thermoacoustic coupling mechanisms is crucial to predicting and mitigating high-frequency instabilities. The thesis provides increased theoretical insights based on detailed experimental investigations of the local flame response of hydrogen and natural gas in a perfectly premixed, atmospheric MJC test rig. The thesis outlines the importance of a convective flame response mechanism for HF thermoacoustic instabilities with a particular focus on the first transverse mode in gas turbine combustors. The main findings concerning the three main objectives of the thesis, i.e. the experimental investigation of the flame response, the low order network modelling and the validation of a local and global flame response model, are summarised in the following.

The **low order modelling approach** for transverse, HF thermoacoustics provides a generalised transfer matrix theory covering low and high frequency acoustic mode propagation. Network elements for ducts, area changes and flames are provided and validated with good agreement to experimental and numerical results. The results demonstrate that by minor changes the existing LF network models can be extended to the HF case. The acoustic analysis and modelling of the longitudinal to transverse injector coupling is crucial for the predictability of convective driving mechanisms. The transverse to longitudinal coupling of an HF mode to the injector tubes is captured by an HF area change transfer matrix. The acoustic energy flux jump condition across the area change yields effective modal areas due to the weighting of the geometrical cross-section with the cross-sectional acoustic mode shape. The use

---

of effective modal areas instead of geometrical cross-sectional areas and the additional frequency dependent axial wave numbers are the key differences compared to LF acoustics.

The experimental investigation of the **premixed flame response** to the first transverse mode of the MJC by  $\text{OH}^*$  chemiluminescence images reveals coherent vortex shedding as the predominant flame response mechanism. The MJC is investigated with and without swirl-stabilised pilot flame. Both configurations reveal the dominant convective flame response due to vortex shedding. The contribution of the convective mechanism compared to the local instantaneous flame displacement and compression is investigated by the MJC with pilot burner for two injector tube lengths. A pressure anti-node coupling condition at the dump plane yields coherent vortex shedding with an opposed sign in the cross-sectional direction of each flame. Although, the local flame response might be dominated by convective reaction rate fluctuations, the instantaneous flame compression and displacement or additional local mechanisms dominate the integrated response. On the contrary, the pressure node coupled case is dominated by the flame response due to coherent vortex shedding at the dump plane, which yields a constant phase of the heat release rate fluctuations over the cross-section of each jet flame. The setup of the MJC without the pilot burner reveals a variation in both the gain and the phase of the flame response in the axial, main flow direction. Turbulent dissipation and the initial increase in intensity of the coherent vortical velocity fluctuations due to the hydrodynamic shear layer instability are two significant effects for the jet flame dynamics. Furthermore, the origin of the convective flame response by acoustic velocity fluctuations at the dump plane is confirmed by the reconstruction of the axial acoustic velocity fluctuations at the dump plane.

The network theory implies a **distributed flame transfer function** accounting for turbulent dissipation and a spatially resolved gain and phase. In extension to existing literature, the axially resolved flame transfer function is based upon the acoustic disturbance energy equation to include arbitrary convective and acoustically non-compact flames. Therefore, the local Rayleigh index and the global Rayleigh integral covers the non-compact flame dynamics and the resulting axial acoustic velocity jump condition across a flame. The non-

compact convective flame response model is validated with the optical results. It reveals the significance of modelling the variation in axial mean velocity and turbulent dissipation along the main flow direction of the jet flames. The initial build-up of the coherent vortex structures due to radial velocity gradients might be accounted for in an advanced model to correctly resolve the axial dependency of the flame transfer function gain and thus the global flame response.

# A Appendix

## A.1 Natural Gas Composition

The natural gas composition used for the evaluation of the unburned and burned gas properties are provided in Tab. A.1 according to [98].

<u>fuelcomponent</u>	<u>molarfraction</u>
<i>CH<sub>4</sub></i>	0.9602
<i>C<sub>2</sub>H<sub>6</sub></i>	0.03
<i>C<sub>3</sub>H<sub>8</sub></i>	0.008
<i>CO</i>	0.0
<i>H<sub>2</sub></i>	0.0
<i>O<sub>2</sub></i>	0.0
<i>CO<sub>2</sub></i>	0.0046
<i>H<sub>2</sub>O</i>	0.0
<i>N<sub>2</sub></i>	0.0036
others	0.0008

**Table A.1:** Natural gas composition according to the average of the year 2021 in munich.

## A.2 Pressure Loss and Massflow Split

The mass flow split between jet and pilot flames impacts the injector tube velocity and the flame stabilisation. First of all, the mass flow split contributes significantly to the flame stabilisation since the global swirl number and the injector tube exit velocity are influenced. Second of all, the observability of the OH\* images might be limited due to too much radiation of the swirl flame. Thus, the design value of the pilot burner mass flow split is chosen one mag-

nitude less than the mass flow of the injector tubes  $f_{\text{pilot}} = 0.1$ . This section provides an analytical design of the test rig pressure drop and the mass flow split between jet and pilot burner.

The flow distributes between the swirl pilot burner and the 8 injector tubes, as depicted in Fig. A.1 on the left. The design condition for the pilot burner mass flow split is

$$f_{\text{pilot}} = \frac{\dot{m}_{\text{pilot}}}{\dot{m}_{\text{Jet}} + \dot{m}_{\text{pilot}}} = 0.1. \quad (\text{A.1})$$

The results of the pressure drop for a constant mass flow split can be seen in on the right side of Fig. A.1. The design case of natural gas with an air access ratio  $\lambda = 1.8$  yields a desirable pressure drop of around 3% at a thermal power of  $P_{th} = 225[\text{kW}]$ . The details of the pressure drop estimation are provided in

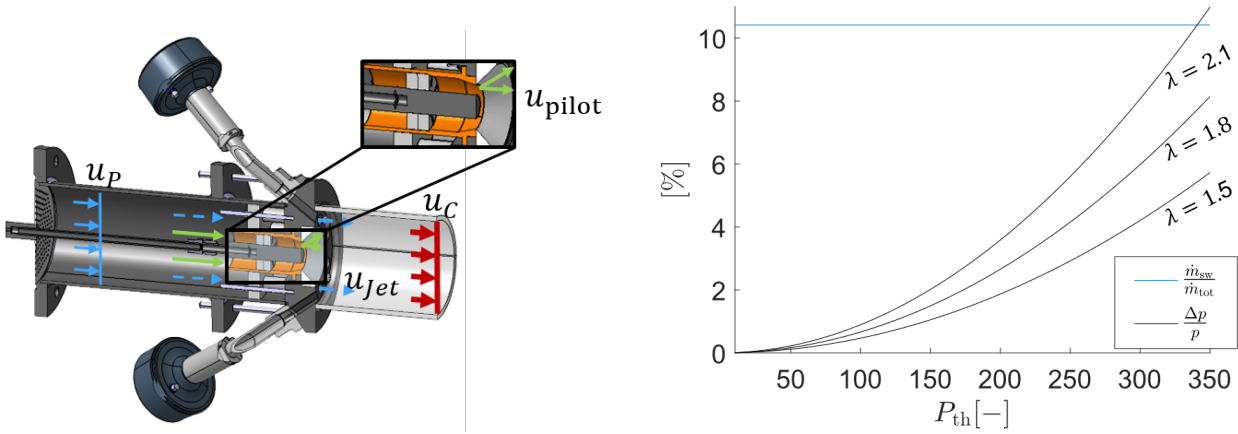


**Figure A.1:** Sketch of the mass flow split between injector tubes and pilot burner (left) and the estimated pressure drop of the test rig (right).

the following.

Continuity of mass applied to Eq. A.1 yields for the mass flow split

$$f_{\text{pilot}} = \frac{1}{\frac{u_{\text{Jet}}}{u_{\text{pilot}}} \frac{A_{\text{Jet}}}{A_{\text{pilot}}} + 1}. \quad (\text{A.2})$$

The energy balance applied in the form of Bernoulli's equation for a stream line through the jets and through the pilot burner respectively yields the con-

dition of an equal pressure drop from the plenum to the combustion chamber

$$\Delta p_{\text{Jet}} = \Delta p_{\text{tot,pilot}}. \quad (\text{A.3})$$

The pressure drop of the pilot burner and the jets are normalised with the dynamic pressure calculated with the unburned gas density and the axial velocity  $u_{\text{pilot}}$  at the exit of the pilot burner

$$\Delta p_{\text{tot,pilot}} = \zeta_{\text{pilot}} \frac{\rho_u}{2} u_{\text{pilot}}^2 \quad (\text{A.4})$$

and  $u_{\text{Jet}}$  at the exit of the injector tubes

$$\Delta p_{\text{Jet}} = \zeta_{\text{Jet}} \frac{\rho_u}{2} u_{\text{Jet}}^2. \quad (\text{A.5})$$

In combination with equation A.3 we obtain

$$\frac{u_{\text{Jet}}}{u_{\text{pilot}}} = \left( \frac{\zeta_{\text{pilot}}}{\zeta_{\text{Jet}}} \right)^{0.5}. \quad (\text{A.6})$$

Inserting Eq. A.6 in Eq. A.2 yields an explicit equation for  $f_{\text{pilot}}$  dependent on the area ratio and the ratio of the loss coefficients

$$f_{\text{pilot}} = \frac{1}{\frac{A_{\text{Jet}}}{A_{\text{pilot}}} \left( \frac{\zeta_{\text{pilot}}}{\zeta_{\text{Jet}}} \right)^{0.5} + 1}. \quad (\text{A.7})$$

The area ratio is calculated from the geometrical parameters.

The injector tube cross-section and the swirl slots of the pilot burner can be modelled as a perforated plate using a hydraulic diameter. Therefore, a flexible model for the loss coefficient of a perforated plate as a function of the hydraulic diameter, the length of the perforated plate, the Reynolds - Number and the contraction coefficient is required. The loss coefficient of perforated plates is modelled by a sudden area expansion accounting for the area ratio of the integral perforated cross-sectional area determined by the hydraulic diameter (index: h) to the total cross-sectional area after the flow expansion (index: tot) which yields

$$\varphi = \frac{A_h}{A_{\text{tot}}}. \quad (\text{A.8})$$

The contraction coefficient  $k_d$  accounts for the vena contracta (index: vc) at the Borda - Inlet

$$k_d = \frac{A_{vc}}{A_h}. \quad (\text{A.9})$$

The loss coefficient is estimated for a tube with  $L \gg d_h$  via

$$\zeta_{B.C.} = \underbrace{\left(1 - \frac{1}{k_d}\right)^2}_{\zeta_{\text{Borda}}} + \underbrace{\left(1 - \frac{A_h}{A_{\text{tot}}}\right)^2}_{\zeta_{\text{Carnot}}}. \quad (\text{A.10})$$

The first term accounts for the expansion due to the vena contracta (Borda inlet) and the second term accounts for the expansion due to the geometrical change in cross-section (Carnot diffusor). The expansion due to the Borda inlet and the Carnot diffusor in Eq. A.10 are separate from each other, which includes the assumption that the flow field re-attaches to the wall after the vena contracta before the expansion takes place.

The loss coefficient of the injector tubes  $\zeta_{\text{jet}}$  is directly estimated by the Borda-Carnot diffusor Eq. A.10. In reality, the loss is also dependent on the dimensionless length of the tube  $L/d_h$  as well as the Reynolds - Number as described in [99] which is accounted for the design of the mass flow split. The injector tube and swirl slot length and the Reynolds numbers of interest are in the critical range of  $\text{Re} \approx 10^3 - 10^4$  and  $L/d_h \approx 1$ . Equation A.10 yields the asymptotic value of  $\zeta = 1.41$ , for  $\frac{L}{d_h} > 10$  and above a critical Reynolds number of  $\text{Re} = 10^8$  [99].

The loss coefficient of the pilot burner requires a series of multiple pressure losses due to the pilot burner geometry depicted in Fig. A.2. The pilot burner consists of a cylindrical tube and a central pilot burner lance. The flow passes the straight swirl slots of the width  $d_{\text{slot}}$ . The swirl component of the flow is induced by the inclined swirl slots of the width  $d_{\text{slot},\alpha}$  with the angle  $\alpha = 14^\circ$ . The loss coefficient of the pilot burner is calculated via a series of Borda - Carnot pressure losses

$$\Delta p_{\text{tot,pilot}} = \zeta_{\text{pilot}} \frac{\rho_u}{2} u_{\text{pilot}}^2 = \Delta p_{\text{tot,slot}} + \Delta p_{\text{tot,slot},\alpha} + \Delta p_{\text{tot,Carnot}} \quad (\text{A.11})$$

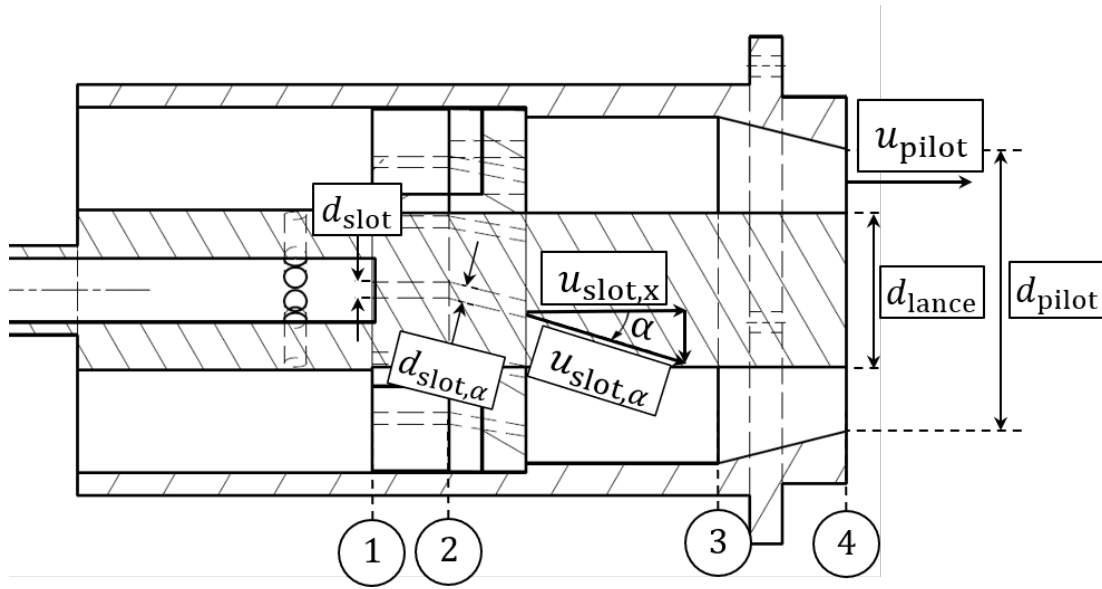


**Figure A.2:** Sketch of the pilot burner with the separation into the different pressure loss segments.

and is given in relation to the axial outlet velocity  $u_{\text{pilot}}$  of the pilot burner

$$\zeta_{\text{pilot}} = \frac{u_{\text{slot}}^2 \zeta_{\text{slot}} + u_{\text{slot},\alpha}^2 \zeta_{\text{slot},\alpha} + u_{\text{pilot}}^2 \zeta_{\text{Carnot}}}{u_{\text{pilot}}^2}. \quad (\text{A.12})$$

The first loss coefficient  $\zeta_{\text{slot}}$  of the straight slots from position 1 to 2 is a Borda - inlet, which accounts for the loss due to the expansion from the vena contracta to the swirl slot width  $d_{\text{slot}}$  by the first part of Eq. A.10. The second loss coefficient  $\zeta_{\text{slot},\alpha}$  is calculated as a Borda - Carnot loss from position 2 to 3 via Eq. A.10 with the hydraulic diameter of the inclined swirl slots. This accounts for the second vena contracta after the flow passes the angle  $\alpha$  of the inclined swirl slots. Here, the values of  $k_d$  are dependent on the swirl slot angle [97]. The last loss coefficient accounts for the Carnot loss due to the sudden area expansion from position 4 to the combustion chamber diameter by the second term in Eq. A.10. The loss due to the swirl component of the flow is considered by the absolute value of the velocity vector at the swirl slots

$$u_{\text{slot},\alpha} = u_{\text{slot},x} \sqrt{1 + \tan^2(\alpha)}. \quad (\text{A.13})$$

The use of the continuity equation replaces the ratios of the velocities in the numerator of Eq. A.12 to the reference velocity  $u_{\text{pilot}}$  by the respective area

ratios

$$\zeta_{\text{pilot}} = \frac{A_{\text{pilot}}^2}{A_{\text{slot}}^2} \zeta_{\text{slot}} + \frac{A_{\text{pilot}}^2}{A_{\text{slot},\alpha}^2} \zeta_{\text{slot},\alpha} + \zeta_{\text{Carnot}}, \quad (\text{A.14})$$

which finally yields the pilot burner loss coefficient.

### A.3 Heat Loss Estimation

Heat losses might have a major impact on flame stabilisation due to a lower reactivity as well as the acoustic behaviour of the combustor due to a different speed of sound compared to the adiabatic case. In order to determine the possible impact, the global heat losses are estimated with a black box model from in- to outlet of the combustor, see the left side of Fig. A.3. The goal is to extract design points of the combustor with a low sensitivity on heat losses for variable thermal power and as adiabatic design points as possible. The results of the heat loss estimation can be seen on the right side of Fig. A.3. Above a thermal power of  $P_{\text{th}} = 175$  [kW] the heat loss leads to a temperature drop of less than 5%, which is acceptable.

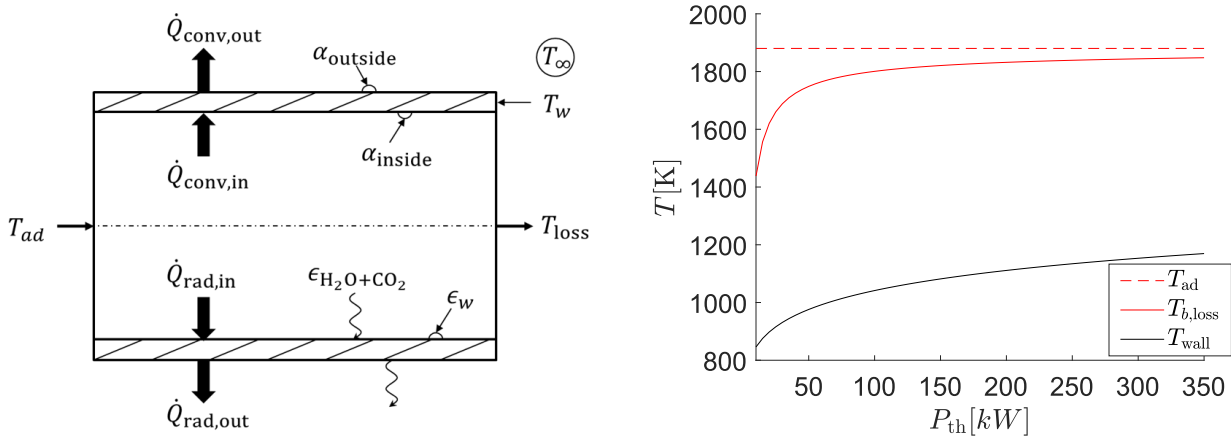


**Figure A.3:** Sketch of the heat loss model (left) and the estimated burned gas and wall temperature of the combustor (right).

The details on the heat loss estimation model are given below. Radiative as well as convective heat losses are estimated in the following. The heat flux

on the outside of the combustion chamber (index: out)  $\dot{Q}_{\text{loss,out}}$  over the area  $A_{M,\text{out}} = \pi d_{c,\text{out}} L_c$  is given by the sum of the convective and radiative heat fluxes

$$\dot{Q}_{\text{loss,out}} = \dot{Q}_{\text{conv,out}} + \dot{Q}_{\text{rad,out}}. \quad (\text{A.15})$$

The convective heat flux

$$\dot{Q}_{\text{conv,out}} = \alpha_a A_{M,\text{out}} (T_{W,\text{out}} - T_\infty) \quad (\text{A.16})$$

requires and estimate for the heat transfer coefficient  $\alpha_a$ . The radiative heat flux is given by

$$\dot{Q}_{\text{rad,out}} = \epsilon_{\text{quartz}} \sigma A_{M,\text{out}} (T_{W,\text{out}}^4 - T_\infty^4) \quad (\text{A.17})$$

with the Stephen-Boltzmann constant  $\sigma = 5.67 \cdot 10^{-8} [\text{W}^2 \text{m}^{-2} \text{K}^{-4}]$  and requires and estimate of the quartz glass emissivity  $\epsilon_{\text{quartz}}$ . View factors are neglected for the estimation of the radiative heat loss. The heat flow in the combustion chamber  $\dot{Q}_{\text{loss,in}}$  through the inner area  $A_{M,\text{in}} = \pi d_{c,\text{in}} L_c$  is given by

$$\dot{Q}_{\text{loss,in}} = \dot{Q}_{\text{conv,in}} + \dot{Q}_{\text{rad,in}}, \quad (\text{A.18})$$

with the inner convective heat flux

$$\dot{Q}_{\text{conv,in}} = \alpha_{\text{in}} A_{M,\text{in}} (T_{\text{ad}} - T_{W,\text{in}}) \quad (\text{A.19})$$

and the inner radiative heat flux

$$\dot{Q}_{\text{rad,in}} = \frac{\epsilon_{\text{quartz}}}{1 - (1 - \epsilon_{\text{quartz}})(1 - a_g)} \sigma A_{M,\text{in}} (\epsilon_g T_{\text{ad}}^4 - a_g T_{W,\text{in}}^4). \quad (\text{A.20})$$

Gas radiation of the cylindrical gas body to the quartz glass surface is considered according to [99]. The inner and the outer heat fluxes are connected via the thermal heat conduction inside the glas. If heat conduction should be taken into account, the instationary heat conduction must be considered according to

$$T_{W,a} = T_{W,\text{in}} + \frac{\dot{Q}_{\text{loss}}}{\lambda_{\text{quartz}} A_{M,\text{in}}} R_{W,\text{in}} \ln \left( \frac{R_a}{R_{\text{in}}} \right). \quad (\text{A.21})$$

However, the temperature gradients in the quartz glas due to convective heat transfer and heat radiation might be neglected for the thin wall thickness to obtain

$$T_W = T_{W,\text{in}} = T_{W,\text{out}} \quad (\text{A.22})$$

$i[-]$	$b_{0i}[-]$	$b_{1i}[\text{K}^{-1}]$	$k_{Gi}[\text{m}^{-1}\text{bar}^{-1}]$
1	0.130	+0.000265	0.0
2	0.595	-0.000150	0.824
3	0.275	-0.000115	25.907

**Table A.2:** Constants for the calculation of the emissivity of water - carbon-dioxide mixtures  $\epsilon_{H_2O,CO_2}$  for  $0.5 < \frac{p_{H_2O}}{p_{CO_2}} < 2$ .

The total heat flux stays constant in the stationary case, which yields

$$\dot{Q}_{\text{loss}} = \dot{Q}_{\text{loss,in}} = \dot{Q}_{\text{loss,out}} \quad (\text{A.23})$$

Finally, the burned gas temperature including heat losses is obtained

$$T_{\text{ad}} = T_u + \frac{\dot{m}_F H_u - \dot{Q}_{\text{loss}}}{\dot{m}_{\text{loss}} c_{p,b}}. \quad (\text{A.24})$$

The required heat transfer coefficients and gas mixture emissivity and absorption coefficients are taken from data of the VDI Wärmesatlas [99]. The radiative gas in the chamber is modelled by a  $H_2O - CO_2$  mixture and all other radiative components are neglected, which is a common assumption due to the high emissivities of  $H_2O$  and  $CO_2$  compared to the remaining components. The emissivity is calculated using

$$\epsilon_g = \sum_{i=1}^3 A_i \left( 1 - \frac{1}{e^{(k_i (x_{H_2O} + x_{CO_2}) p_{\infty} \cdot s_{gl})}} \right) \quad (\text{A.25})$$

which depends on the partial pressures, here split into molar fractions and total pressure. Furthermore, the equivalent thickness of the radiating gas body  $s_{gl}$  has to be specified, which is a geometrical factor. The considered radiating gas is cylindrical due to the combustor geometry. The radiation is considered only at the curved outward pointing area of the gas body, i.e. a cylinder without plane end areas. The height to diameter ratio  $h/d = 2$  yields  $s_{gl} = 0.76$  [99].

The weighting factors  $A_i$  are obtained from

$$A_i = b_{0i} + b_{1i} T_g \quad (\text{A.26})$$

and are calculated with the data given in Tab. A.2 according to [99] The convective heat transfer inside the chamber to the chamber wall is modelled by

the convective heat transfer coefficient  $\alpha_i$  between a parallel flow and a plate. The convective heat transfer coefficient outside of the chamber  $\alpha_a$  is modelled by the impingement of a single round jet since impingement cooling is used.

## **Previous Publications**

Parts of the Ph.D. thesis have been published by the author in conference proceedings and journal papers [90–92]. All of these publications are registered according to the valid doctoral regulations. Therefore, they are not necessarily quoted explicitly in the text. Whether they were referenced depends on maintaining comprehensibility and providing all necessary context.

## Supervised Student Theses

Associated with this Ph.D. thesis, a number of student theses and projects were supervised by the author of the present work. These theses were prepared at the Chair of Thermodynamics at TUM in the years 2021 to 2023 under the close supervision of the present author. Parts of these supervised theses may be incorporated into the present thesis. The author would like to express his sincere gratitude to all formerly supervised students for their commitment and support of this research project.

---

Name	Thesis
Kajetan Planötscher	Numerical Investigation of the Dynamics of a Multi-Jet-Combustor with the Hybrid CFD / CA Method
Sirine Kharfi	Verification of an Analytical Model for the Injector Coupling to Transverse Modes in Tubular Combustors
Leonard Dootz	Akustische Inbetriebnahme eines Multi-Jet Brenners zur Untersuchung von hochfrequenten Schwingungen durch vorgemischte Strahlflammen
Jonas Neu	Experimental Validation of an Analytical Model of the Transverse to Longitudinal Coupling of High Frequency Acoustic Waves

---

# Bibliography

- [1] Lammel, O., Schütz, H., Schmitz, G., Lückerath, R., Stöhr, M., Noll, B., Aigner, M., Hase, M. and Krebs, W. “FLOX combustion at high power density and high flame temperatures.” *Journal of Engineering for Gas Turbines and Power* (2010) DOI 10.1115/1.4001825.
- [2] Krebs, W., Schulz, A., Winzel, B., Johnson, C., Laster, W., Pent, J., Schilp, R., Wasif, S. and Weaver, A. “Advanced combustion system for high efficiency (ACE) of the new SGT/6-9000HL gas turbine.” *Proceedings of the ASME Turbo Expo* (2022) DOI 10.1115/GT2022-82299.
- [3] Lieuwen, T. C. and Yang, V. *Combustion instabilities in gas turbine engines*. American Institute of Aeronautics and Astronautics, Reston ,VA (2006).
- [4] Poinso, T. and Veynante, D. *Theoretical and numerical combustion*. Edwards, Philadelphia, Pa. (2001).
- [5] Harrje, D. T. and Reardon, F. H. *Liquid propellant rocket combustion instability*. Washington D. C. (1972).
- [6] Dowling, A. P. and Stow, S. R. “Acoustic analysis of gas-turbine combustors.” *Journal of Propulsion and Power* (2003) DOI 10.2514/5.9781600866807.0369.0414.
- [7] Glenn Research Center. “Apollo era testing.” (1958). Accessed 01.12.2023, URL <https://www1.grc.nasa.gov/historic-facilities/rocket-engine-test-facility/apollo-era-testing/>.

- [8] Goetz, O. K. and Monk, J. C. “Combustion device failures during space shuttle main engine development.” *5th International Symposium on Liquid Space Propulsion Long Life Combustion Device Technology* (2003).
- [9] Polifke, W. “Modeling and analysis of premixed flame dynamics by means of distributed time delays.” *Progress in Energy and Combustion Science* (2020) DOI 10.1016/j.pecs.2020.100845.
- [10] O’Connor, J., Acharya, V. and Lieuwen, T. “Transverse combustion instabilities: acoustic, fluid mechanic, and flame processes.” *Progress in Energy and Combustion Science* (2015) DOI 10.1016/j.pecs.2015.01.001.
- [11] Poinso, T. “Prediction and control of combustion instabilities in real engines.” *Proceedings of the Combustion Institute* (2017) DOI 10.1016/j.proci.2016.05.007.
- [12] Rayleigh, J.W.S. “The explanation of certain acoustical phenomena.” *Nature* (1878): pp. 319–321 DOI 10.1038/018319a0.
- [13] Hardi, J. S., Beinke, S. K., Oswald, M. and Dally, B. B. “Coupling of cryogenic oxygen–hydrogen flames to longitudinal and transverse acoustic instabilities.” *Journal of Propulsion and Power* (2014) DOI 10.2514/1.B35003.
- [14] Gröning, S., Hardi, J. S., Suslov, D. and Oswald, M. “Injector-driven combustion instabilities in a hydrogen/oxygen rocket combustor.” *Journal of Propulsion and Power* (2016) DOI 10.2514/1.B35768.
- [15] Armbruster, W., Hardi, J. S., Suslov, D. and Oswald, M. “Experimental investigation of self-excited combustion instabilities with injection coupling in a cryogenic rocket combustor.” *Acta Astronautica* (2018) DOI 10.1016/J.ACTAASTRO.2018.06.057.
- [16] Schulze, M., Wagner, M. and Sattelmayer, T. “Linearized euler equations for the determination of scattering matrices for orifice and perforated plate configurations in the high mach number regime.” *Aerospace* (2016) DOI 10.3390/aerospace3040033.

- [17] Urbano, A., Selle, L., Staffelbach, G., Cuenot, B., Schmitt, T., Ducruix, S. and Candel, S. "Exploration of combustion instability triggering using Large Eddy Simulation of a multiple injector liquid rocket engine." *Combustion and Flame* (2016) DOI 10.1016/j.combustflame.2016.03.020.
- [18] Urbano, A., Douasbin, Q., Selle, L., Staffelbach, G., Cuenot, B., Schmitt, T., Ducruix, S. and Candel, S. "Study of flame response to transverse acoustic modes from the LES of a 42-injector rocket engine." *Proceedings of the Combustion Institute* (2017) DOI 10.1016/j.proci.2016.06.042.
- [19] Schwing, J., Grimm, F. and Sattelmayer, T. "A model for the thermoacoustic feedback of transverse acoustic modes and periodic oscillations in flame position in cylindrical flame tubes." *Proceedings of the ASME Turbo Expo* (2012) DOI 10.1115/GT2012-68775.
- [20] Schwing, J. and Sattelmayer, T. "High-frequency instabilities in cylindrical flame tubes: feedback mechanism and damping." *Proceedings of the ASME Turbo Expo* (2013) DOI 10.1115/GT2013-94064.
- [21] Berger, F., Hummel, T., Hertweck, M., Kaufmann, J., Schuermans, B. and Sattelmayer, T. "High-frequency thermoacoustic modulation mechanisms in swirl-stabilized gas turbine combustors - part I experimental investigation." *Journal of Engineering for Gas Turbines and Power* (2017) DOI 10.1115/1.4035591.
- [22] Zellhuber, M., Schwing, J., Schuermans, B., Sattelmayer, T. and Polifke, W. "Experimental and numerical investigation of thermoacoustic sources related to high-frequency instabilities." *International Journal of Spray and Combustion Dynamics* (2014) DOI 10.1260/1756-8277.6.1.1.
- [23] Hummel, T., Berger, F., Hertweck, M., Schuermans, B. and Sattelmayer, T. "High-frequency thermoacoustic modulation mechanisms in swirl-stabilized gas turbine combustors: part two - modeling and analysis." *Proceedings of the ASME Turbo Expo* (2016) DOI 10.1115/GT2016-57500.
- [24] Veynante, D. and Vervisch, L. "Turbulent combustion modeling." *Progress in Energy and Combustion Science* (2002) DOI 10.1016/S0360-1285(01)00017-X.

## BIBLIOGRAPHY

---

- [25] Biagioli, F., Innocenti, A., Lamraoui, A. and Syed, K. J. “Analytical modelling of flame transfer functions for technically premixed flames.” *International Journal of Spray and Combustion Dynamics* (2022) DOI 10.1177/17568277221094403.
- [26] Baillot, F., Durox, D. and Prud’Homme, R. “Experimental and theoretical study of a premixed vibrating flame.” *Combustion and Flame* (1992) DOI 10.1016/0010-2180(92)90049-U.
- [27] Fleifil, M., Annaswamy, A. M., Ghoneim, Z. A. and Ghoniem, A. F. “Response of a laminar premixed flame to flow oscillations: a kinematic model and thermoacoustic instability results.” *Combustion and Flame* (1996) DOI 10.1016/0010-2180(96)00049-1.
- [28] Dowling, A. P. “A kinematic model of a ducted flame.” *Journal of Fluid Mechanics* (1999) DOI 10.1017/S0022112099005686.
- [29] Ducruix, S., Durox, D. and Candel, S. “Theoretical and experimental determination of the transfer function of a laminar premixed flame.” *Proceedings of the Combustion Institute* (2000) DOI 10.1016/S0082-0784(00)80279-9.
- [30] Schuller, T., Durox, D. and Candel, S. “A unified model for the prediction of laminar flame transfer functions: comparisons between conical and V-flame dynamics.” *Combustion and Flame* (2003) DOI 10.1016/S0010-2180(03)00042-7.
- [31] Sattelmayer, T. “Influence of the Combustor Aerodynamics on Combustion Instabilities From Equivalence Ratio Fluctuations.” *Journal of Engineering for Gas Turbines and Power* (2003) DOI 10.1115/1.1365159.
- [32] Schuermans, B., Bellucci, V., Guethe, F., Meili, F., Flohr, P. and Paschereit, C. O. “A detailed analysis of thermoacoustic interaction mechanisms in a turbulent premixed flame.” *Proceedings of the ASME Turbo Expo* (2004) DOI 10.1115/GT2004-53831.
- [33] Buschhagen, T., Gejji, R., Philo, J., Tran, L., Portillo Bilbao, J. E. and Slabaugh, C. D. “Experimental investigation of self-excited combustion

- instabilities in a lean, premixed, gas turbine combustor at high pressure.” *Journal of Engineering for Gas Turbines and Power* (2018) DOI 10.1115/1.4039760.
- [34] Buschhagen, T., Gejji, R., Philo, J., Tran, L., Portillo Bilbao, J. E. and Slabaugh, C. D. “Self-excited transverse combustion instabilities in a high pressure lean premixed jet flame.” *Proceedings of the Combustion Institute* (2019) DOI 10.1016/j.proci.2018.07.086.
- [35] Philo, J. J., Gejji, R. M. and Slabaugh, C. “Injector-coupled transverse instabilities in a multi-element premixed combustor.” *International Journal of Spray and Combustion Dynamics* (2020) DOI 10.1177/1756827720932832.
- [36] McClure, J., Berger, F. M., Bertsch, M., Schuermans, B. and Sattelmayer, T. “Observation of reactive shear layer modulation associated with high-frequency transverse thermoacoustic oscillations in a gas turbine reheat combustor experiment.” *International Journal of Spray and Combustion Dynamics* (2022) DOI 10.1177/17568277221088192.
- [37] Lee, T. and Kim, K. T. “High-frequency transverse combustion instabilities of lean-premixed multislit hydrogen-air flames.” *Combustion and Flame* (2022) DOI 10.1016/j.combustflame.2021.111899.
- [38] Grimm, F., Lourier, J. M., Lammel, O., Noll, B. and Aigner, M. “A selective fast fourier filtering approach applied to high frequency thermoacoustic instability analysis.” *Proceedings of the ASME Turbo Expo* (2017) DOI 10.1115/GT2017-63234.
- [39] Sharifi, V., Kempf, A. M. and Beck, C. “Large-eddy simulation of acoustic flame response to high-frequency transverse excitations.” *AIAA Journal* (2019) DOI 10.2514/1.J056818.
- [40] Sharifi, V. “Investigation of high-frequency thermoacoustic instabilities.” Ph.D. Thesis, University Duisburg-Essen. 2021.
- [41] Shipley, K. J. “Multi-injector modeling of transverse combustion instability experiments.” Ph.D. Thesis, Purdue University. 2014.

## BIBLIOGRAPHY

---

- [42] McClure, J., Bothien, M. R. and Sattelmayer, T. “High-frequency mode shape dependent flame-acoustic interactions in reheat flames.” *Journal of Engineering for Gas Turbines and Power* (2022) DOI 10.1115/1.4055531.
- [43] Campa, G. and Camporeale, S. M. “Prediction of the thermoacoustic combustion instabilities in practical annular combustors.” *Journal of Engineering for Gas Turbines and Power* (2014) DOI 10.1115/1.4027067.
- [44] Nicoud, F., Benoit, L., Sensiau, C. and Poinso, T. “Acoustic modes in combustors with complex impedances and multidimensional active flames.” *AIAA Journal* (2007) DOI 10.2514/1.24933.
- [45] Silva, S., Nicoud, F., Schuller, T., Durox, D. and Candel, S. “Combining a helmholtz solver with the flame describing function to assess combustion instability in a premixed swirled combustor.” *Combustion and Flame* (2013) DOI 10.1016/j.combustflame.2013.03.020.
- [46] Laera, D. and Camporeale, S. M. “A weakly nonlinear approach based on a distributed flame describing function to study the combustion dynamics of a full-scale lean-premixed swirled burner.” *Journal of Engineering for Gas Turbines and Power* (2016) DOI 10.1115/1.4036010.
- [47] Munjal, M. L. *Acoustics of ducts and mufflers*. Wiley, New York (1987).
- [48] Polifke, W., Poncet, A., Paschereit, C. O. and Döbbeling, K. “Reconstruction of acoustic transfer matrices by instationary computational fluid dynamics.” *Journal of Sound and Vibration* (2001) DOI 10.1006/jsvi.2001.3594.
- [49] Evesque, S. and Polifke, W. “Low-order acoustic modelling for annular combustors: validation and inclusion of modal coupling.” *Proceedings of the ASME Turbo Expo* (2002) DOI 10.1115/GT2002-30064.
- [50] Polifke, W., van der Hoek, J. and Verhaar, B. “Everything you always wanted to Know About f and g: Technical report, ABB Corporate Research, Baden, CH.” (2009).
- [51] Parmentier, J.-E., Salas, P., Wolf, P., Staffelbach, G., Nicoud, F. and Poinso, T. “A simple analytical model to study and control azimuthal instabilities

- in annular combustion chambers.” *Combustion and Flame* (2012) DOI 10.1016/j.combustflame.2012.02.007.
- [52] Fournier, G. J. J., Meindl, M., Silva, C. F., Ghirardo, G., Bothien, M. R. and Polifke, W. “Low-order modeling of can-annular combustors.” *Journal of Engineering for Gas Turbines and Power* (2021) DOI 10.1115/1.4051954.
- [53] Bauerheim, M., Nicoud, F. and Poinso, T. “Progress in analytical methods to predict and control azimuthal combustion instability modes in annular chambers.” *Physics of Fluids* (2016) DOI 10.1063/1.4940039.
- [54] Dowling, A. P. and Akamatsu, S. “Three dimensional thermoacoustic oscillation in a premix combustor.” *Proceedings of the ASME Turbo Expo* (2001) DOI 10.1115/2001-GT-0034.
- [55] You, D., Sun, X. and Yang, V. “A three-dimensional linear acoustic analysis of gas turbine combustion instability.” *Aerospace Sciences Meeting and Exhibit* (2003) DOI 10.2514/6.2003-118.
- [56] Sitek, A., Ville, J. M. and Foucart, F. “Multiload procedure to measure the acoustic scattering matrix of a duct discontinuity for higher order mode propagation c.” *Journal of the Acoustical Society of America* (2006) DOI 10.1121/1.2354040.
- [57] Sack, S. and Abom, M. “In-duct measurements: modal identification of ducted sources.” *NATO STO* (2017) DOI 10.14339/STO-EN-AVT-287.
- [58] Leandro, R. E. and Polifke, W. “Low-order modelling of distributed heat release.” *Proceedings of the International Congress of Sound and Vibration* (2012).
- [59] Campa, G., Camporeale, S. M., Cosatto, E. and Mori, G. “Thermoacoustic analysis of combustion instability through a distributed flame response function.” *Proceedings of the ASME Turbo Expo* (2012) DOI 10.1115/GT2012-68243.
- [60] Hofmeister, T. E. “Influence of acoustically induced vorticity perturbations on high-frequency thermoacoustic instabilities in gas turbine combustors.” Ph.D. Thesis, Technical University of Munich. 2021.

- [61] Peters, N. *Turbulent combustion*. Cambridge monographs on mechanics, Cambridge University Press, Cambridge England and New York (2000).
- [62] Hirsch, C., Fanaca, D., Reddy, P., Polifke, W. and Sattelmayer, T. “Influence of the swirler design on the flame transfer function of premixed flames.” *Proceedings of the ASME Turbo Expo* (2005) DOI 10.1115/GT2005-68195.
- [63] Chu, B. T. and Kovásznyai, L. S. G. “Non-linear interactions in a viscous heat-conducting compressible gas.” *Journal of Fluid Mechanics* (1958) DOI 10.1017/S0022112058000148.
- [64] Crow, S. C. and Champagne, F. H. “Orderly structure in jet turbulence.” *Journal of Fluid Mechanics* (1971) DOI 10.1017/S0022112071001745.
- [65] Hussain, A. K. M. F. *Controlled perturbation of circular jets*. University of Houston, Texas (1971).
- [66] Hussain, A. K. M. F. “Coherent structures and turbulence.” *Journal of Fluid Mechanics* (1986) DOI 10.1017/S0022112086001192.
- [67] Myers, M. K. “Transport of energy by disturbances in arbitrary steady flows.” *Journal of Fluid Mechanics* (1991) DOI 10.1017/S0022112091002434.
- [68] Nicoud, F. and Poinso, T. “Thermoacoustic instabilities: Should the Rayleigh criterion be extended to include entropy changes?” *Combustion and Flame* (2005) DOI 10.1016/j.combustflame.2005.02.013.
- [69] Brear, M. J., Nicoud, F., Talei, M., Giauque, A. and Hawkes, E. R. “Disturbance energy transport and sound production in gaseous combustion.” *Journal of Fluid Mechanics* (2012) DOI 10.1017/jfm.2012.264.
- [70] Delfs, J. *Basics of aeroacoustics, Lecture notes*. Technische Universität Braunschweig, Institut für Aerodynamik und Strömungstechnik Abteilung Technische Akustik (2017).
- [71] Ehrenfried, K. *Strömungsakustik 2, Vorlesungsskript*. Technische Universität Berlin (2003).

- [72] Heilmann, G., Liu, T., Romero Vega, P. and Sattelmayer, T. “A novel decomposition approach preventing spurious entropy generation in hybrid thermoacoustic stability calculations.” *Journal of Engineering for Gas Turbines and Power* (2022) DOI 10.1115/1.4055189.
- [73] Heilmann, G. and Sattelmayer, T. “On the convective wave equation for the investigation of combustor stability using FEM-methods.” *International Journal of Spray and Combustion Dynamics* (2022) DOI 10.1177/17568277221084470.
- [74] Ehrenfried, K. *Strömungsakustik 1, Vorlesungsskript*. Technische Universität Berlin (2003).
- [75] Kim, J., Gillman, W., Wu, D., Emerson, B., Acharya, V., Mckinney, R., Isono, M., Saitoh, T. and Lieuwen, T. “Identification of high-frequency transverse acoustic modes in multi-nozzle can combustors.” *Proceedings of the ASME Turbo Expo* (2021) DOI 10.1115/GT2020-16130.
- [76] Güthe, F. and Schuermans, B. “Phase-locking in post-processing for pulsating flames.” *Measurement Science and Technology* (2007) DOI 10.1088/0957-0233/18/9/039.
- [77] Schuermans, B., Moeck, J., Audrey, B., Bayu, D. and Nicolas, N. “The rayleigh integral is always positive in steadily operated combustors.” *Combustion and Flame* (2022) DOI 10.1016/j.proci.2022.08.035.
- [78] Feldman, M. “Hilbert transform in vibration analysis.” *Mechanical Systems and Signal Processing* (2011) DOI 10.1016/j.ymsp.2010.07.018.
- [79] Kim, J., Lieuwen, T., Emerson, B., Acharya, V., Wu, D., Mckinney, R. and Wang, X. Isono, M. “High-frequency acoustic mode identification of unstable combustors.” *Proceedings of the ASME Turbo Expo* (2019) DOI 10.1115/GT2019-91029.
- [80] Keller, Jacob J. “Thermoacoustic oscillations in combustion chambers of gas turbines.” *AIAA Journal* (1995) DOI 10.2514/3.12980.

## BIBLIOGRAPHY

---

- [81] Shanbhogue, S. J., Seelhorst, M. and Lieuwen, T. “Vortex phase-jitter in acoustically excited bluff body flames.” *Journal of spray and combustion dynamics* (2007) DOI 10.1260/175682709789141528.
- [82] Rienstra, S. W. and Hirschberg, A. *An Introduction to Acoustics*. Eindhoven University of Technology (2021).
- [83] Steinbacher, T. and Polifke, W. “Convective velocity perturbations and excess gain in flame response as a result of flame-flow feedback.” *Fluids* (2022) DOI 10.3390/fluids7020061.
- [84] Romero Vega, P. “Numerical Modeling of High-Frequency Transverse.” Ph.D. Thesis, Technical University of Munich. 2022.
- [85] Polifke, W. and Lawn, C. “On the low-frequency limit of flame transfer functions.” *Combustion and Flame* (2007) DOI 10.1016/j.combustflame.2007.07.005.
- [86] Lawn, C. J. “Lifted flames on fuel jets in co-flowing air.” *Progress in Energy and Combustion Science* (2009) DOI 10.1016/j.pecs.2008.06.003.
- [87] Mangold, T. O., Orchini, A., Paschereit, C. O., Moeck, J. P. and Bohon, M. D. “Flame response of a lean premixed swirl flame to high frequency azimuthal forcing.” *Proceedings of the ASME Turbo Expo* (2022) DOI 10.1115/GT2022-84211.
- [88] Pierce, A. D. *Acoustics: An introduction to its physical principles and applications*. ASA Press Springer, Cham (2019).
- [89] Evesque, S., Polifke, W. and Pankiewitz, C. “Spinning and azimuthally standing acoustic modes in annular combustors.” *AIAA Journal* (2003) DOI 10.2514/6.2003-3182.
- [90] Rosenkranz, J. A. and Sattelmayer, T. “An analytical model of the injector response to high frequency modes in a tubular multi-jet combustor.” *Proceedings of the ASME Turbo Expo* (2022) DOI 10.1115/GT2022-81957.
- [91] Rosenkranz, J. A. and Sattelmayer, T. “Experimental investigation of high frequency flame response on injector coupling in a perfectly premixed

- multi-jet combustor.” *Journal of Engineering for Gas Turbines and Power* (2023) DOI 10.1115/1.4063375.
- [92] Rosenkranz, J. A., Neu, J. and Sattelmayer, T. “Network- and CFD/CAA-modelling of the high frequency flame response in multi-jet combustors.” *Proceedings of the SoTiC* (2023).
- [93] Kuhn, P., Soria, J. and Oberleithner, K. “Linear modelling of self-similar jet turbulence.” *Journal of Fluid Mechanics* (2021) DOI 10.1017/jfm.2021.292.
- [94] Hirsch, C. *Technische Verbrennung: Einführung in Theorie und Anwendungen technischer Verbrennungssysteme, Vorlesungsskript*. Technische Universität München, Lehrstuhl für Thermodynamik (2020).
- [95] Hinze, J. O. *Turbulence*. McGraw-Hill series in mechanical engineering, McGraw-Hill, New York, NY (1987).
- [96] Turns, S. R. *An introduction to combustion: Concepts and applications*. McGraw-Hill, Boston (2011).
- [97] Sigloch, H. *Technische Fluidmechanik*. Springer-Verlag, Berlin/Heidelberg (2005).
- [98] “Erdgasbeschaffenheit: Jahresmittel für 2021: Erdgasnetz der SWM Infrastruktur GmbH und Co. KG.” (2021). Accessed 30.01.2024, URL <https://www.swm-infrastruktur.de/erdgas/netzstrukturdaten/gasbeschaffenheitsmerkmale>.
- [99] VDI. *VDI-Wärmeatlas*. Springer Berlin Heidelberg, Berlin, Heidelberg (2013). DOI 10.1007/978-3-642-19981-3.